Modeling of photonic band gap crystals and applications

by

Ihab Fathy El-Kady

A thesis submitted to the graduate faculty

in partial fulfillment of the requirements for the degree of

DOCTOR OF PHILOSOPHY

Major: Condensed Matter Physics

Program of Study Committee:
Kai-Ming Ho, Major Professor
Rana Biswas
Bruce Harmon
Constantine Stassis
Laurent Hodges
Gary Tuttle

Iowa State University

Ames, Iowa

2002

Graduate College
Iowa State University

This is to certify that the doctoral dissertation of

Ihab Fathy El-Kady

has met the dissertation requirements of Iowa State University

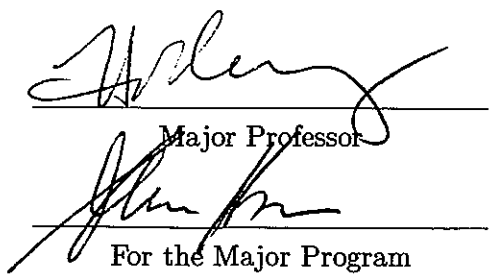

Major Professor

For the Major Program

TABLE OF CONTENTS

LIST OF FIGURES

Acknowledgments

I would like to take the opportunity to thank those people without whose help this thesis would not have been possible. My heartfelt gratitude goes out to my academic advisor, Professor Kai-Ming Ho, whose guidance, encouragement and insight have always been invaluable. My appreciation and gratitude must also go out to Professor Shawn Lin for all of his encouragement, exciting discussions and enthusiastic approach to the topic. My appreciation must also go to Dr. Rana Biswas for all the useful advice and suggestions during the course of this work. I would like also to extend my thanks to Dr. Michael Sigalas for acquainting me with the numerical techniques at hand and putting me up to speed with the codes. My thanks must also be extended to Dr. Zhi-Yuan Li for his invaluable help and support. I would like to also thank my committee members, Professors Bruce Harmon, Constantine Stassis, Laurent Hodges, and Garry Tuttle for their valuable comments and discussions.

My upmost gratitude, thanks, and appreciation must go to my parents, Professors Nabila El-Sayed and Fathy El-Kady, for their never ending support, kindness, believing in me and for simply being the kind hearted people they are, to whom I will always be in debted to.

I would like also to acknowledge the love and support of my wife, Inas El-Shazly, her continuous encouragement and never ending sacrifices. To her I extend my gratitude and appreciation for putting up with my unusual work schedule and being patient throughout the difficult periods of my research.

I am also grateful to my younger sister, Amira, and my younger brothers, Ayman and Osama, for cheering me up whenever I needed, and for claiming to take me as a mentor and an example they are proud of. To them I extend my deepest wishes of success and happiness and a life full of accomplishments that will surpass and overwhelm my own.

To my officemates, my sincerest thanks for putting up with me for the past few months while I've been rather stressed while writing my thesis. If it had not been for their support, suggestions, ideas and assistance, this thesis would have been finished months ago! I would like to especially thank Mohammed Al-Saqer for being more than a brother to me and such a great friend whom I would trust with my life. I would also like to thank Mehmet Fatih Su for many useful, though sometimes fairly incomprehensible, conversations concerning the compilers and computer machines, and most importantly with getting all the bugs out of my codes. My appreciation must also go out to Dr. Bassam Shehadeh for his invaluable friendship and his technical support with the TEX when writing this thesis.

I wish to thank Professors Mohammed Al-Semary, Khalil Abdu, and Abd-Alhady Saleh from the Department of Physics, Cairo University, for showing me the way and setting an example in whose footsteps I follow, and for teaching me that there are no limits to our accomplishments except those we set for ourselves.

My deep appreciation must also go to our group adminestrator Rebecca Shivvers, who always works extremely hard to guide the rest of us through the maze of administrative obstacles and is always on hand to sort things out when we get it wrong!

To all of these people and to the endless others who have made my life here at Ames over the past few years enjoyable, I extend a word of thanks and gratitude. Thank you!

The United States Government has assigned the DOE Report number IS-T2043 to this thesis. Notice: This document has been authored by the Iowa State University of Science and Technology under Contract No. W-7405-ENG-82 with the U.S. Department of Energy. The U.S. Government retains a none-exclusive, paid-up, irrevocable, world-wide license to publish or reproduce the published form of this document, or allow others to do so, for U.S. Government purposes.

Abstract

In this work, we have undertaken a theoretical approach to the complex problem of modeling the flow of electromagnetic waves in photonic crystals. Our focus is to address the feasibility of using the exciting phenomena of photonic gaps (PBG) in actual applications.

We start by providing analytical derivations of the computational electromagnetic methods used in our work. We also present a detailed explanation of the physics underlying each approach, as well as a comparative study of the strengths and weaknesses of each method. The Plane Wave expansion, Transfer Matrix, and Finite Difference Time Domain Methods are addressed. We also introduce a new theoretical approach, the Modal Expansion Method.

We then shift our attention to actual applications. We begin with a discussion of 2D photonic crystal wave guides. The structure addressed consists of a 2D hexagonal structure of air cylinders in a layered dielectric background. Comparison with the performance of a conventional guide is made, as well as suggestions for enhancing it. Our studies provide an upper theoretical limit on the performance of such guides, as we assumed no crystal imperfections and non-absorbing media.

Next, we study 3D metallic PBG materials at near infrared and optical wavelengths. Our main objective is to study the importance of absorption in the metal and the suitability of observing photonic band gaps in such structures. We study simple cubic structures where the metallic scatterers are either cubes or interconnected metallic rods. Several metals are studied (aluminum, gold, copper, and silver). The effect of topology is addressed and isolated metallic cubes are found to be less lossy than the connected rod structures. Our results reveal that the best performance is obtained by choosing metals with a large negative real part of the dielectric function, together with a relatively small imaginary part.

Finally, we point out a new direction in photonic crystal research that involves the interplay of metallic-PBG rejection and photonic band edge absorption. We propose that an absolute metallic-PBG may be used to suppress the infrared part of the blackbody emission and, emit its energy only through a sharp absorption band. Potential applications of this new PBG mechanism include highly efficient incandescent lamps and enhanced thermophotovoltaic energy conversion. The suggested lamp would be able to recycle the energy that would otherwise go into the unwanted heat associated with usual lamps, into light emitted in the visible spectrum. It is estimated this would increase the efficiency over conventional lamps by about 40%.

1 Introduction to Photonic Crystals

Dissertation Organization

In this dissertation, we follow an alternative thesis format, which allows for the inclusion of published papers in scholarly journals. Each paper is presented as an independent chapter in exactly the same format it was published. In what follows, we present a brief description of the highlights of each chapter and how it fits in the theme of this work. In addition, a brief abstract of the contents of each chapter is provided at the beginning of the chapter.

In chapter 1, we present a general introduction to the subject of photonic band gaps and crystals. A rather detailed thorough review of the most relevant theoretical and experimental literature in the area is provided to get the reader acquainted with the most recent developments in the field and to set the stage for the discussions provided in the subsequent chapters. In this chapter we also address the need for adequate theoretical techniques for studying the complex problem of electromagnetic wave propagation in such complicated structures. The needs as well as the expectations from these theoretical approaches are also highlighted.

In chapter 2-4 we provide a review of the theoretical techniques employed in the current work. While most of these techniques are existing developed methods, the aim here is to provide a comprehensive picture of these methods. In chapter 5, on the other hand, we present a detailed discussion of a new approach to the problem of modeling the flow of electromagnetic waves in a photonic crystal. This method, the Modal Expansion method, was initially developed and put to extensive use for modeling one- and two-dimensional lamellar gratings. In chapter 5 we explain how this method can be extended successfully to model three-dimensional photonic crystals. The approach we present here is due largely to Zhi-Yuan Li, and has proven to yield converged results where the previous methods have failed.

Chapter 2 provides a detailed development of the first of the theoretical methods addressed in the current work. Here, we investigate the so-called Plane Wave (PW) expansion technique. As we have pointed out in earlier sections, this method is operates in k-space and is used primarily for mapping the band structure of photonic crystals. Our goal is to provide the reader with the theoretical foundation of this method, and to present a brief explanation of its underlying physics. A highlight of the major strengths as well as the limitations and drawbacks of this technique will also be summarized.

Next, we address the Transfer Matrix Method (TMM) in chapter 3. We shall begin by representing Maxwell's equations on a discrete lattice of real space points. We then show how such discrete equations can be recast into the form of a transfer matrix which connects the electric and magnetic fields on one face of a layer of lattice points to another. Once the transfer matrix of the individual layers is obtained, the overall matrix is simply evaluated by taking products of the individual layer transfer matrices. This enables us to find the fields at every point in our system and from this extract the band structure or transmission and reflection information. This method is used primarily for calculating the transmission and reflection coefficients of photonic crystals, both periodic and with considerable disorder. Our goal is to provide the reader with the theoretical foundation of this method, and to present a brief explanation of its underlying physics. A highlight of the major strengths as well as the limitations and drawbacks of this technique will also be summarized.

Our focus in chapter 4 is on the so-called Finite-Difference Time-Domain (FDTD) method. As its name suggests, this method offers a way of probing the temporal as well as the spatial development of waves propagating inside a photonic crystal. However, this is not the only attractive feature about this method; rather, it has another very appealing aspect to it. It turns out, as we will show in later sections that this method scales as an order N , where N is the number of spatial discretization points. This is an order N improvement over the TMM, and N^2 over the PW method. Again, our goal is to provide the reader with the theoretical foundation of this method, and to present a brief explanation of its underlying physics. Finally, a highlight of the major strengths as well as the limitations and drawbacks of this technique

will also be summarized.

Having addressed three of the most widely used techniques in photonic crystal modeling in the first three chapters, we next shift our attention to a new theoretical approach to the problem of modeling the flow of electromagnetic radiation in photonic crystals. The method at hand, known as the Modal Expansion Method (MEM), offers a much more comprehensive study of photonic crystals as compared to the previous approaches, as well as limited weaknesses. This method was initially developed and put to extensive use for modeling one- and two-dimensional lamellar gratings. In chapter 5 we explain how this method can be extended successfully to model three-dimensional photonic crystals. Preliminary results obtained using this new approach will be presented. A highlight of the capabilities of this new approach will be pointed out, as well as the limited number of draw backs it suffers from.

After providing the reader with a sufficient theoretical foundation, we shift our attention to actual applications of the previous theoretical techniques. Chapters 6, 7, and 8 are a collection of selected papers where the previous methods have been put to use. These chapters comprise the core of the research conducted by the author for fulfilment of the Ph.D. thesis requirements. We begin with a discussion of 2D photonic crystal wave guides in chapter 6. The structure addressed consists of a 2D hexagonal structure of air cylinders in a layered dielectric background. Comparison with the performance of a conventional guide is made, as well as discussions related to means and suggestions for enhancing its performance. Our studies also provide an upper theoretical limit on the performance of such guides, as we assumed no crystal imperfections and non-absorbing media. In the first part of our studies, the three-layer structure is studied in vacuum, in the second part, the three-layer structure is put on a high-dielectric-constant substrate to investigate the effects of substrate losses in the system.

Having pointed out the severe limitations of 2D photonic crystals, we shift out attention to 3D photonic crystals. However, to avoid the experimental difficulties of manufacturing several unit cells primarily arising for the small index contrast of semiconducting materials, we focus our attention on the use of metals as our building blocks. This eliminates the need for multiple unit cells to realize the PBG effect. We begin in chapter 7 by theoretically studying

three-dimensional metallic photonic band gap (PBG) materials at near infrared and optical wavelengths. Our main objective is to find the importance of absorption in the metal and the suitability of observing photonic band gaps in this structure. For this reason, we study simple cubic structures and the metallic scatterers of choice are either cubes or interconnected metallic rods. Several different metals are studied (aluminum, gold, copper, and silver). Our calculations favor copper which gives the smaller absorption compared to the rest of the metals studied. The effect of topology is also addressed, and isolated metallic cubes are found to be less lossy than the connected rod structures. The calculations suggest that isolated copper scatterers are very attractive candidates for the fabrication of photonic crystals at the optical wavelengths. We conclude by pointing out the key requirement for reducing the notorious metallic absorption.

The next step is to use our findings so far and utilize them in fabricating an actual metallic photonic crystal. In chapter 8 we point out a new direction in photonic crystal research that involves the interplay of photonic band gap (PBG) rejection and photonic band edge absorption. It is proposed that an absolute PBG may be used to frustrate the infrared part of black-body emission and, at the same time, its energy is preferentially emitted through a sharp absorption band. Potential application of this new PBG mechanism includes highly efficient incandescent lamps and enhanced thermophotovoltaic energy conversion. Here, a new method is proposed and implemented to create an all-metallic 3D crystal at infrared wavelengths, λ, for this purpose. Superior optical properties are demonstrated. The use of metal is shown to produce a large and absolute photonic band gap (from $\lambda \sim 8\mu m$ to $> 208\mu m$). The measured attenuation strength of $\sim$ 30 dB/ per unit cell at $\lambda = 12\mu m$ is the strongest ever reported for any 3D crystals at infrared λ. At the photonic band edge, the speed-of-light is shown to slow down considerably and an order-of-magnitude absorption enhancement is observed. In the photonic allowed band, $\lambda \sim 5\mu m$, the periodic metallic-air boundaries mold the flow of light, leading to an extraordinarily large transmission enhancement. The realization of a 3D absolute band-gap metallic photonic crystal will pave the way for highly efficiency energy applications and for combining and integrating different photonic transport phenomena in a

photonic crystals. One such potential application is the use of such a crystal to manufacture a new type of incandescent lamp. The suggested lamp would be able to recycle the energy, that would otherwise go into the unwanted heat associated with usual lamps, into light emitted in the visible spectrum. It is estimated this would increase the efficiency over the conventional lamps from about 5% to over 60%.

We end the work at hand by providing a summary of our all of our findings in chapter 9. Recommendations for future work as well as ways of enhancing the current theoretical techniques are also pointed out.

Chapters 6, 7, and 8 have all been published in scholarly journals. Chapter 6 was published in the *Journal of Lightwave Technology*, Vol. 17., No. 11, November 1999. Chapter 7 was published in *Physical Review B*, Vol. 62, No.23, December 2001. Chapter 8 is published in *Nature*, Vol. 417, May 2002.

Introduction

In this chapter we present a brief literature review of the major achievements in the field of photonic crystals. This is by no means a complete or exhaustive review of all the work that has been undertaken in this vast and ever expanding field of research; rather, we focus our attention on relevant advances in topics with direct impact on the work at hand. Our goal is to get the reader up-to-date with the subject matter, and acquainted with the underlying motivation for this work. For a more thorough review, the specialized reader is advised to refer to the NATO ASI conference proceedings[1, 2, 3]. A collective theoretical approach to the physics of photonics is also outlined beautifully in K. Sakoda's recent book [4]. Finally, for a general overview of the subject, the book by Joannopoulos [5] also provides an excellent introduction to the field.

A New Wave of Information Carriers

The past few decades have witnessed a technological revolution in industrial electronics. New generations of lightweight, extremely compact, and more efficient devices have dominated

the market. At the top of the list for industrial success criteria are minimal device size and high speeds. As a result, an ever-growing demand for the development of faster more efficient circuits has become the dominant drive in the integrated-circuit industry. However, two problems brought the integrated-circuit industry almost to a halt, inhibited its continuous success, and obstructed its flourishment. First, miniaturization of electronic circuits leads to increased circuit resistance, and hence high levels of power dissipation. Second, high-speeds require greater sensitivity to signal synchronization and a faster means of communication between the various circuit components. Given the order of magnitude drift velocity of electrons in a typical semiconductor crystal, the latter seems a goal with a dead end. As both problems arise essentially from the physical characteristics of the information carrier in such circuits, namely the electron, scientists have recently turned to light as a possible alternative. Fueled by the greater communication speeds that light can offer, the larger band width for information carriage, and the fact that unlike the fermionic electrons, light is not as strongly interacting with itself and its background as electrons are, the candidacy of light seemed quite powerful. Yet, one must pause and ask the important question: If light is to play the role of electrons in the new "optical-circuit" industry, what will play the role of the hosting semiconductor crystals? In essence, what will mold the propagation of light and control these super fast information photons? To answer these and similar questions, we turn back to the fundamental physics underlying the operation of semiconductor devices.

Careful examination of the physics of semiconductors reveals that the underlying physical principle is the existence of an energy band gap, and that all of the subsequent semiconductor applications are a direct result of the ability to control and manipulate this gap. The questions that we must answer then become: how can we open a photonic band gap? What would constitute our valence and conduction bands? What would be our optical impurities, and how can we dope such optical crystals? Finally, and perhaps most the most important question of all is its existence in nature. Do such crystals exist in nature or do they have to be artificially fabricated?

To accomplish our task and aid in our quest, we start by comparing the quantum mechanics

of electrons in a crystal, to the electrodynamics of photons in the proposed photonic crystals. The Schrodinger equation of an electron in a crystal lattice reads:

$$\left[\frac{\hbar^2}{2m}\nabla^2 + V(\mathbf{r})\right]\psi(\mathbf{r}) = E\psi(\mathbf{r}). \tag{1.1}$$

Here, $V(\mathbf{r})$ is the periodic crystal Coulomb potential at the position $\mathbf{r}$ in the lattice, $\psi(\mathbf{r})$ is the electron's quantum mechanical wave function at $\mathbf{r}$, and E is the total energy eigenvalue. The corresponding equation for a photon in a photonic crystal lattice can be obtained by eliminating either the electric or magnetic field vector in favor of the other. Using the macroscopic Maxwell's equations, assuming a source-free medium, and eliminating $\mathbf{E}$ in favor of $\mathbf{H}$ the resulting equation is:

$$\left[\nabla \times \left(\frac{1}{\varepsilon(\mathbf{r})}\nabla \times\right)\right]\mathbf{H}(\mathbf{r}) = \left(\frac{\omega}{c}\right)^2 \mathbf{H}(\mathbf{r}), \tag{1.2}$$

where $\varepsilon(\mathbf{r})$ is the dielectric function at the position $\mathbf{r}$ in the lattice, $\mathbf{H}(\mathbf{r})$ is the magnetic field vector at $\mathbf{r}$, and ω is the angular frequency. Careful examination of Equations (1.1) and (1.2) yields the following analogies and similarities. First, they are both simple eigenvalue problems, which means that, in principle, both can be approached using standard eigenvalue solution techniques. Both operators, enclosed in square brackets, on the left-hand side of the equations are Hermitian, as can easily be verified. This, in turn, implies their solutions will be real measurable quantities. Finally, but most importantly, we see that $\varepsilon(\mathbf{r})$ is the photonic counterpart of $V(\mathbf{r})$. This suggests that a crystal structure in which the dielectric function varies periodically would somehow open up a photonic band gap. Moreover, by extending the analogy even further, we see this so-called photonic band gap would manifest itself in the form of band(s) of forbidden frequencies, ω, for light propagation through the crystal, in as much as its counterpart, the electronic energy band gap, E, forbids the propagation of electronic waves in a crystal lattice.

In spite all of these similarities, however, there are some grave differences. First, the Schrodinger equation is a scalar wave equation, while the Maxwell equations are vector equa-

tions. This imposes an additional constraint on the solutions of Equation (1.2), namely $\nabla \cdot \mathbf{H} = 0$, or that the solutions must be transverse. In addition, Maxwell equations can "in principle" be solved exactly; whereas, due to the electron-electron interaction, the electronic Schrodinger equation cannot. Of course, as we shall see shortly, particularly in chapter 2 and throughout the rest of this thesis, this is far easier said than done. Yet, the most striking difference is that, unlike the semiconductor crystals, which are not only naturally occurring, but also extremely abundant, our much-desired photonic crystals would have to be artificially fabricated.

What is a photonic crystal?

In light of our previous discussions, one can define a photonic crystal as a novel class of artificially fabricated structures which possess the ability to control and manipulate the propagation of light. Such crystals can be constructed by periodically repeating an array of dielectric or metallic units in one, two, or three dimensions, thereby constituting what have come to be known as one-, two-, or three-dimensional photonic crystals.

The underlying physical principle of operation of such crystals is rather simple: an electromagnetic wave passing through an array of periodic scatterers will undergo destructive interference for certain combinations of wave vectors at certain frequencies, thus forbidding their propagation. Though such an idea is not completely new and has been around for quite sometime, the Fabry-Perot resonators, or as they are sometimes called Bragg stacks, are one example [6], what we intended to do with it is quite different. Rather than simply reflecting the incident electromagnetic radiation at all but one frequency without any control over the subsequent propagation, as is the case with the above examples, the idea is to fully control and direct light through its full course of propagation. Properly designed, such photonic crystals would not only have the ability to allow the propagation of light in certain frequency regions and inhibit it in others, but also localize light and restrict it to a certain region of space [7].

Potential applications of such structures include loss free mirrors on which a microwave dipole antenna can be mounted; in this case greater efficiencies and high directionality are

expected as compared with mounting in conventional dielectric substrates [8, 9, 10]. Others have suggested the use of such crystals as lossless wave guides [11], where a line defect would be created and operated at frequencies within the gap of the underlying periodic photonic structure. Such a guide would not only have the ability to guide light from one point to the other without any loss whatsoever, but also would have the ability to do so around sharp corners where conventional dielectric slab guides and optical fibers are known to be very lossy. Moreover, and perhaps the most intriguing of all applications, would be the possibility of creating optical switches and logic gates by implementing non-linear materials, in which case the position and size of the gap would be mandated by the light intensity [12]. This would make the hopes of replacing all the current electronic devices with optical counter parts a possible reality!

The search for Photonic Band Gaps: A Brief Literature Review

Three-dimensional photonic band gap structures

Photonic band gaps were first suggested by Yablonovitch in 1986 [13]. Yablonovitch's goal was to try to inhibit or suppress electron-hole pair radiative recombinations, a major loss mechanism in semiconductor devices. Arguing the analogy with the one-dimensional (1D) interference coatings, Yablonovitch proposed that a three-dimensional (3D) layered dielectric structure would open up an electromagnetic band gap where electromagnetic waves would be forbidden to propagate. Using a simple straight forward calculation, the size of the gap would be dictated by the contrast between the two refractive indices $n1$ and $n2$ of the alternating layers. He estimated the required contrast to be at least $\Delta n \approx 0.21n$, where $\Delta n = n1 - n2$ and $n = (n1 + n2)/2$. Yablonovitch went even further, explaining how such a 3D layered dielectric structure could be fabricated or grown. He proposed a checkerboard type of arrangement that would eventually lead to a face centered cubic (FCC) lattice structure. Yet, Yablonovitch acknowledged in his paper that it would be difficult to find a common lattice matched pair of materials with a sufficiently large index difference. However, because of the simplistic arguments and the modest approach to the problem that Yablonovitch followed, his work did

not spark strong interest at the time.

Only a few months later, S. John proposed a new mechanism of strong Anderson localization [14]. The idea was that a carefully prepared 3D periodic dielectric structure containing random disorders would lead to strong localization of light in the neighborhood of the disorders. His theoretical studies were based on the solutions of the scalar wave equation of the electric field. He attributed the resulting localization to the periodic nature of the surrounding dielectric, and deduced that a threshold index contrast of $n1/n2 \gtrsim 2.13$ was necessary to open up an electromagnetic frequency gap to inhibit the propagation of light, and hence promote its localization. He also suggested that this so-called gap would extend in all three directions if the Brillouin zone (BZ) of the underlying dielectric lattice was as close to sphericity as possible. Although completely theoretical and based on a scalar wave approximation, later proven to be an inaccurate oversimplification, John's study is regarded as one of the fundamental theoretical foundations in the field.

In light of the arguments presented by John, Yablonovitch made the first experimental attempt at fabricating a photonic band gap crystal [15]. To ensure his success, Yablonovitch modeled his structures based on analogies drawn and concepts extended from the electron waves in a crystal. By analogy with the electronic case, it was expected that band gaps would appear at places where the constant energy surface in the momentum space, (k-space), comes close to touching the Brillouin zone boundary. To maximize the chance of producing a complete omnidirectional gap, it would be necessary to produce Brillouin zone with almost equal extends in all crystal directions. In other words, an almost spherical Brillouin zone! Out of all the common lattice types, the face centered cubic (FCC) structure has the most spherical first Brillouin zone. Based on these arguments, and using a "cut and try" method [15], Yablonovitch fabricated two classes of test structures. The first class consisted of FCC arrays of Al_2O_3 ($n \approx 3.0$) spheres in an air background with a range of filling fractions. The second consisted of FCC arrays of spherical air voids in a dielectric host ($n \approx 3.5$), Fig.1.1, again in a range of filling fractions. In spite of Yablonovitch's elaborate experimental efforts, out of a total of 21 fabricated structures, only one produced what was perceived back then as

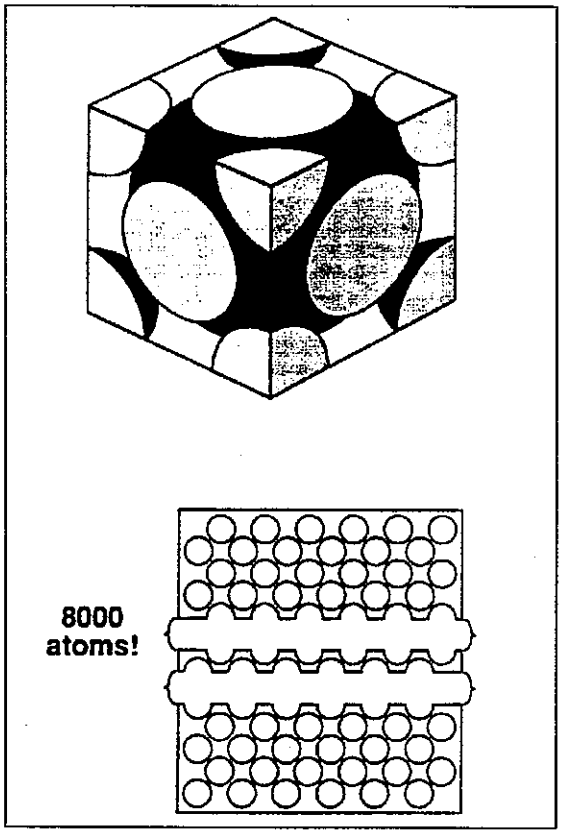

Figure 1.1 Construction of FCC crystals consisting of spherical voids. Hemispherical holes are drilled on both faces of a dielectric sheet, which are then stacked up to make an FCC crystal [15].

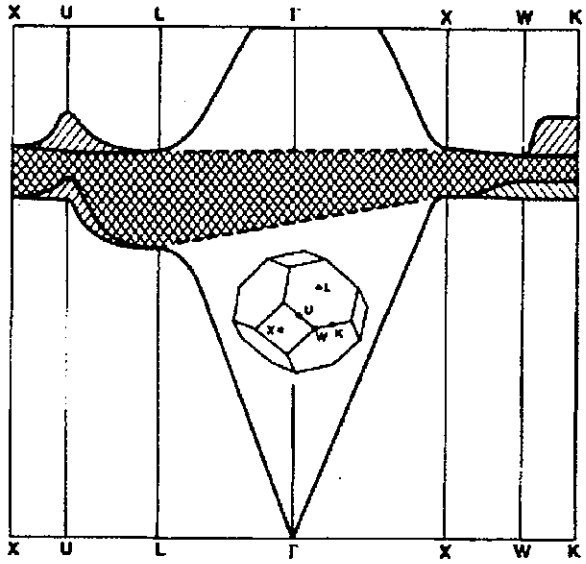

Figure 1.2 The experimentally reported photonic band structure in reciprocal space for and FCC spherical-air-atom crystal with 86% filling fraction [15].

a full 3D photonic band gap, Fig.1.2. Because of the lack of experimental resolution, however, a degeneracy of the bands at the W and U points was overlooked, and the structure only displayed a pseudo gap in the frequency range investigated by the experiment. This fact was only highlighted and proven to be the case when adequate vector wave calculations were later implemented, as will be discussed briefly. It is only fair, however, to mention that the FCC structure fabricated by Yablonovitch, does in fact possess a band gap, but it resides at a higher frequency range than he had predicted experimentally. Nevertheless, Yablonovitch's attempt was regarded as a breakthrough.

The first elaborate theoretical investigation of Yablonovitch's experiment was carried out independently by two different groups: S. Satpathy, Z. Zhang, and M. Salehpour [16], and K. Leung and Y. Liu [17]. In these studies, however, the scalar wave approximation was invoked. Here the two polarizations of the electromagnetic waves were treated separately, thereby decoupling the problem and reducing it to the solution of two scalar equations. The results showed the existence of a gap, but the position and size of the gap were not in quantitative agreement

with Yablonovitch's experiment. Furthermore, they also predicted the existence of full 3D gaps at a smaller threshold index contrast, contradicting what was observed experimentally! The only reasonable conclusion was that the errors made by neglecting the vector nature of light were more serious than initially anticipated.

A full vector calculation for Yablonovitch's FCC experiment was performed by K. M. Leung and Y. F. Lin [18]. In their approach, the plane wave expansion technique was used to solve Maxwell's equations. The process proved to be somewhat complicated and lengthy, in principle, because they eliminated the magnetic field in favor of the electric in Maxwell's equations, thus yielding an eigenvalue equation in which the operator was not Hermitian. Nevertheless, their results provided a more detailed mapping of the energy gap than prior calculations, and distinguished between *S-polarized* and *P-polarized* waves. Although their results generally agreed with the experiment performed by Yablonovitch [15], there was a grave disagreement in the size of the gaps at the W and U Brillouin Zone points! Their calculations revealed no gap at these two points, rather the bands were found to be degenerate. They assessed that the observed degeneracy at the U Zone point was purely accidental and could be lifted by varying the value of the air-to-dielectric filling fraction. The degeneracy at the W Zone point is, on the other hand, real and can be attributed to the inherent structure symmetry. These observations were also found by Z. Zhang and S. Satpathy [19], who assessed that the FCC structure fabricated by Yablonovitch [15], at the most, possessed a pseudo gap resulting from *Mie resonances.* In spite of the agreement between the results of K. M. Leung and Y. F. Lin [18] and those of Z. Zhang and S. Satpathy [19], there were serious doubts about their validity. Their technique suffered from convergence problems as well as inconsistent solutions for the electric and magnetic components of the fields. (See chapter 2 for details.)

Soon after, K. M. Ho, C. T. Chan, and C. M. Soukoulis [20] proposed a different approach for the dielectric function representation within the same context of the plane wave expansion technique. Their approach provided a simple solution to the inconsistency problem observed previously in the plane wave method, and also achieved faster convergence. However, more significant was the observation that the degeneracy at the W and U Brillouin zone points was

actually real, and resulted from the crossing of the second and third bands at these symmetry plane points. Contrary to earlier reports [18], such a degeneracy was independent of refractive-index contrasts and filling ratios. In essence, the degeneracy cannot be lifted rendering the FCC structure gapless, and confirming the error in the experimental observations of Yablonovitch [15]. More important, however, was the suggestion provided by Ho et al. for creating a photonic crystal structure with an actual full 3D gap. In their classic 1990 paper, Ho et al. proposed the use of a diamond structure consisting of either dielectric spheres in an air background, or the inverse structure of air spheres in a dielectric background. The result was an astonishing full 3D gap with a gap-to-midgap ratio ($\frac{\Delta\omega}{\omega}$) of up to 21% for the first case and a record high value of 46% for the latter (these bounds were later corrected to 14 and 29%, respectively [21]). In spite of this great discovery, however, the proposition made by Ho et al., although theoretically sound, was extremely impractical! Due to the complexity and the intricate detail of the diamond structure its fabrication is, up till today, impossible in the relevant length scales! This meant that the hunt for a realistic structure which can be realized practically and that possessed a full 3D gap was still on, and a realistic photonic band gap structure was in serious doubt [22].

The first practical structure followed shortly after. In an attempt to fabricate the diamond structure proposed by Ho et al. [20], Yablonovitch noted that the diamond structure is a very open structure characterized by open channels along the $\langle 100 \rangle$ directions. Thus, by drilling cylindrical channels through a dielectric block along these directions, a structure with the inherent diamond symmetry can, in principle, be created. Now, since there are 6 sets of $\langle 100 \rangle$ directions in the lattice, there will be 6 sets of channels that would need to be drilled. To ease the problem of the necessary delicate alignment, the structure can be tilted so that the (111) plane is exposed, in which case 3 of the necessary six sets of holes will be slanted at 35.26^0 with respect to the normal to the (111) plane. However, the remaining 3 sets of holes would have their axes parallel to the $\langle 111 \rangle$ direction, and, hence, will be extremely hard to accomplish on a thin film oriented along the $\langle 111 \rangle$ direction. In the end, and because of the difficulty, Yablonovitch [23] abandoned the last 3 sets, and maintained only the first 3. However, he

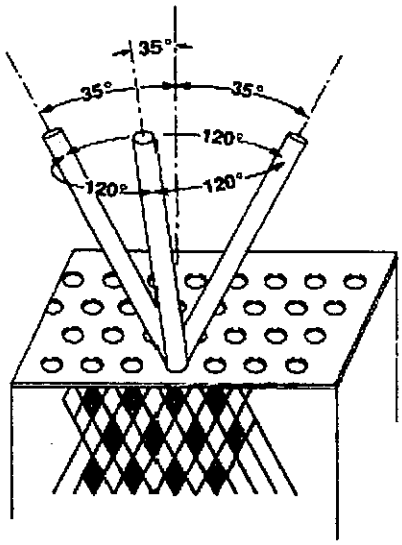

Figure 1.3 Three-axis drilling technique for constructing the Yablonivite structure [23].

ingeniously pointed out that only these 3 were necessary for lifting the degeneracy suffered by his previous FCC structure. He noted that what the diamond structure had essentially accomplished was to introduce 2 atoms per Wigner-Seitz unit cell in its FCC twin structure.

Viewed from a different angle, it is equivalent to deforming the atoms located at the cubic lattice points into a cluster of 2 touching atoms for a large enough filling fraction, one of the major requirements of the Ho et al. group [20]. This is precisely what the 3-axis drilling technique had produced, with the exception that the atoms are now odd-shaped, roughly cylindrical voids centered in the Wigner-Seitz unit cell, with a preferred axis pointing in the $\langle 111 \rangle$ direction, Fig.1.3. The structure was, in fact, found to possess a moderate full 3D gap. The gap-to-midgap ratio was only $\frac{\Delta\omega}{\omega} = 19\%$ for the high bound dielectric contrast of 3.6. Nevertheless, a practical structure was now in hand, and applications seemed a close reality. Although the structure introduced by Yablonovitch [23] displayed a full 3D gap, it proved to be extremely difficult to realize at optical frequencies where the core of the anticipated applications lay.

A more amenable type of photonic crystal lattice was later introduced by Ho et al. [24].

Later to be known as the Iowa State University (ISU) layer-by-layer structure, this structure Fig.1.4 consists of layers of 1D rods with a stacking sequence that repeats every fourth layer with a repeat distance c. Within each layer the rods are arranged in a simple 1D pattern and are separated by a distance a. The rods constituting the next layer are rotated through an angle $\theta = 90^0$. The rods in every alternate layer are parallel, but shifted laterally relative to each other by half a rod spacing. Though strikingly simple in form, this structure actually possesses the symmetry of a face centered tetragonal lattice (FCT), and for the special case of $\frac{c}{a} = \sqrt{2}$, the lattice can be derived from an FCC unit cell with a biases of two rods! Even more striking is the fact that this layered structure can be derived from the famous diamond structure by replacing the $\langle 110 \rangle$ chain of atoms with rods!

This structure has several appealing features. First, it has been observed to produce a large gap-to-midgap ratio of up to 18%, and was predicted to produce large gap-to-midgap of up to 28%, when modified by drilling cylindrical holes through it yielding a diamond-like network [24]. Not only that, but this large gap is actually quite robust and is immune to the specific shape of the rods, and persists even with dielectric contrasts as low as 1.9. Furthermore, the gap is seen to persist even with inter-layer rotation angles as small as 60^0. Most important of all, however, is the relative ease of its fabrication using conventional microfabrication techniques even at optical wavelengths. Recently, this structure has actually been fabricated at optical wavelengths by S. Y. Lin et al. [25]. A further appealing feature is the inherent symmetry of the structure that allows for the ease of accommodation of point and line defects for use in creating high-quality resonance cavities and wave guides [27]. For example, the removal of one complete rod would create a line defect suitable for straight wave guides. On the other hand, the removal of two touching half rods in two successive layers would create a 90^0 bend wave guide [26]. Furthermore, the removal of two complete touching rods would create a "T-splitter" [26], and so on.

One major concern with the ISU structure, however, is the alignment of the alternate parallel layers. As studies conducted by the ISU group have suggested, the observed gap is rather very sensitive to the relative alternate layers shift. A deviation from the selected half a

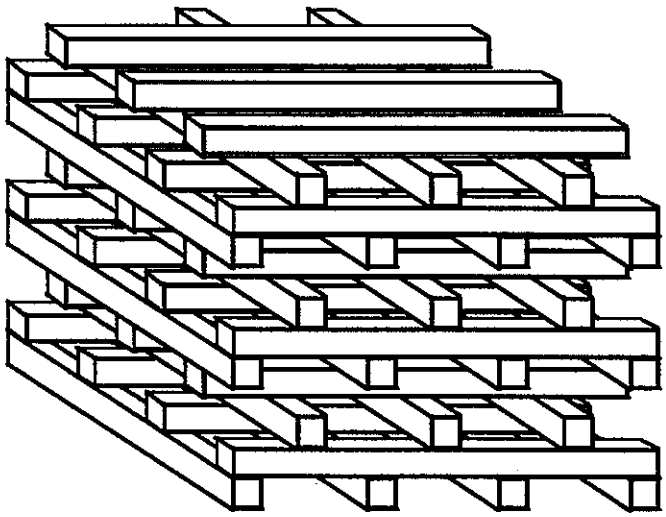

Figure 1.4 Schematic diagram of the ISU layer-by-layer structure.

rod spacing shift results in a drastic reduction in the size of the gap. In fact in the special case of a zero alternate layer shift, the structure acquires the so-called wood-pile arrangement, which has been shown to be gapless [28]. While the alignment problem is trivial in the millimeter wavelength scale, it is a major problem in the optical wavelengths, where state-of-the-art optical aligners must be employed [26]. This is a major drawback, and as a result has limited the popularity of optical research related to the ISU structure to a handful of groups. Several recent efforts have been directed towards finding alternate methods for overcoming the alignment problem, the most recent was accomplished by the Japanese group [29]. Here, a unit cell of the structure is formed by wafer binding two successive bilayers. The redistribution of the diffraction pattern intensity as each set of bilayers is shifted relative to the other is used as an indicator for determining the exact half a rod spacing shift.

A third structure displaying a full band gap was later suggested by the MIT group [31]. Like the ISU layer-by-layer structure, this structure was supposedly introduced around a possible fabrication scheme. First, a layer of high index semiconductor, typically Si, is grown to a thickness d. Next, a series of parallel groves of width w, depth d, and spacing a are etched and backfilled with a second material of a lower refractive index, e.g., SiO_2. Another layer of Si is then grown on top to a thickness of $h < d$. A second series of groves translated laterally

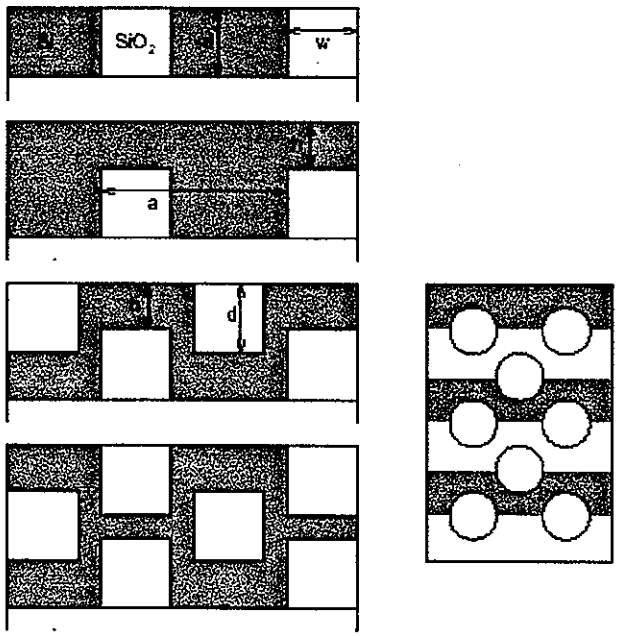

Figure 1.5 A schematic for the growth process for the MIT group's layered structure [30].

by $\frac{a}{2}$ with respect to the first set are then etched to a depth of d, so they actually cut into the first layer. The entire process is then repeated to yield an intricate 3D structure of strides and holes. The fabrication process is shown in Fig.1.5. To maximize the resulting gap, the regions of the lower index material are then etched away completely. It is claimed that the construction of such a structure has "an inherent simplicity"!

Several difficulties, however, combat this claim. First, the successive parts of the above growth technique must be aligned. This is notoriously difficult. To some extent this has been addressed by the MIT group who have gone on to make a series of calculations in which they consider certain amounts of disorder either in the layer thicknesses or in their alignment. Their results [32] show that the band gaps do survive these fabrication imperfections up to an irregularity of $\approx$ 16%. A more serious problem, however, is the drilling of holes in the final fabrication step specifically on the micron scale? In two-dimensional systems, regularly spaced holes have indeed been achieved on that scale, but only by exploiting the special etching

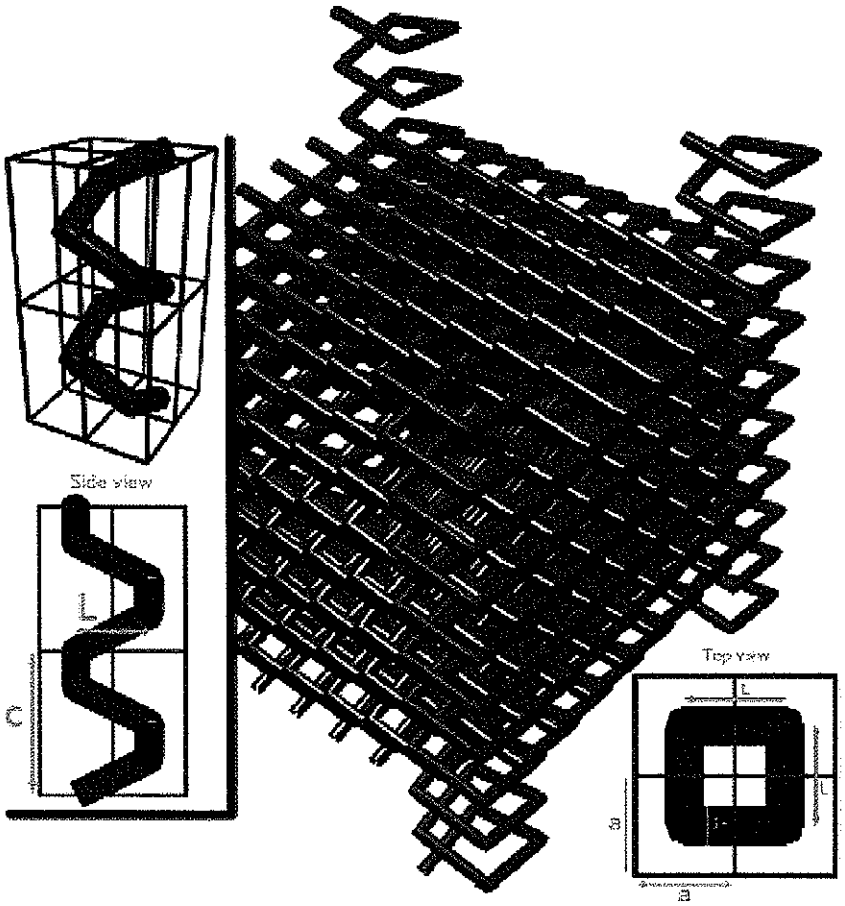

Figure 1.6 Tetragonal square spiral photonic crystal. The crystal shown here has a solid filling fraction of 30%. For clarity, spirals at the corners of the crystal are highlighted with a different color and height. The tetragonal lattice is characterized by lattice constants a and c. The geometry of the square spiral is illustrated in the insets and is characterized by its width, L, cylinder radius, r, and pitch, c. The top left inset shows a single spiral coiling around four unit cells [33].

properties of silicon. In the structure at hand, however, this would have to be done in two different materials at the same time. Whether this can be achieved in the same way is not yet clear.

On top of all of this lies another surprise! although in the end the MIT structure looks quite complicated, it can be shown that it is nothing other than the ISU structure viewed from the (111) face, but with wave-shape-like rods instead of straight ones! As a consequence, most of the experimental work performed on 3D structures has been performed on the relatively "easier" ISU layer-by-layer structure.

Very recently, a new structure based on an underlying tetragonal lattice geometry has been introduced by O. Toader and S. John [33, 34]. The structure, illustrated in Fig.1.6, consists basically of square spiral posts grown initially on a two-dimensional square lattice of growth centers. The result is a tetragonal lattice of intertwined spirals with a gap-to-midgap ratio of 15%. Though considerable smaller in gap size and relatively more complicated, it has been claimed that such a structure is amenable to micro-fabrication using a technique called Glancing Angle Deposition [35, 36]. Although such a structure reportedly has minimal alignment issues compared to the previous layered structures, it remains to see how intentional defects and wave guides can be incorporated in the structure. An interesting observation, however, is that this structure is founded on a tetragonal symmetry, and hence belongs to the same symmetry group as the previous layered structures, and the hunt is still on for simpler 3D structures.

Two-dimensional photonic band gap structures

Ideally, it would be desirable to fabricate 3D photonic structures at optical length scales. After all, this is where their greatest impact in today's technology is anticipated. The key number here is $1.5\mu m$. However, as is clear from the previous discussion, fabricating a structure which is periodic in all three dimensions at such length scales is far from a trivial problem. As a result, the attention of quite a few groups in the community has shifted to the relatively easy to fabricate two-dimensional (2D) photonic crystals.

Vast theoretical and experimental studies were carried out on structures consisting of air rods drilled in a dielectric slab and arranged in either a square or a triangular lattice, as well as on the inverse structure of dielectric rods in an air background [37, 38, 39, 40, 41, 42]. The argument was that in spite of the missing periodicity in the third dimension, there are still major potential applications for such crystals, if proven to exist. Among such applications were planar wave guides, super prisms [43], and prefect planar mirrors [44]. In addition, because of the relative ease in fabrication, and the order of magnitude reduction in the theoretical calculations, such 2D structures would constitute a domain in which new physics can be explored, and grounds for proof of physical principles [45].

The first key measurements were performed by scientists at IBM working in the microwave regime [46]. Their test structure consisted of a square lattice of alumina rods with 0.74mm diameter and a lattice constant of 1.87mm. Their measurements revealed a large gap for the TM modes (**E** field parallel to the rods) and a significantly smaller gap was observed for the TE modes (**H** field parallel to the rods). Their observations were later confirmed by calculations performed by the MIT group [47]. Further calculations by the same group also suggested that a triangular lattice was a more favorable structure for opening sizable gaps for both polarizations. An unfavorable observation, however, was that such gaps are not overlapping!

More recent work included the calculation of the band structures of a whole class of 2D hexagonal structures, commonly known as the boron nitride structures [42]. Here, two interlocking triangular lattices of different diameter rods were used. At the one extreme when the radius of the rods belonging to one of the lattices is set equal to zero, we obtain the usual triangular lattice. On other, when the two radii are equal, we obtain the honey-comb or hexagonal lattice. The largest gaps were observed for the cases of a triangular lattice of air cylinders in a dielectric background, and for a hexagonal lattice of dielectric (in their case graphite) cylinders in an air background.

Effects of introducing disorders in 2D photonic crystals has since been investigated. Cavities resulting from point defects were studied using the transfer matrix method (TMM) [48]. Other studies focused on the disorder introduced by perturbing the position or radii of the

cylinders [49]. In all of these studies, however, the 2D structures were assumed to be infinite in the third dimension. In spite of this, the reported theoretical predictions for the effects of removing a single or multiple rows of cylinders agreed well with the experimental results [50]. However, major concerns were raised as to the viability of such defects as wave guides, since losses in the third dimension were neglected.

Several different approaches were undertaken while fabricating submicron 2D structures. One approach was to use reactive ion etching of semiconducting glass arrays [51] or to use high resolution electron beam lithography [52]. Another was based on exploiting the anisotropic etching properties of silicon to produce macroporous silicon structures [53, 54]. More recently, however, a technique based on photo-electrochemical etching was introduced by the Max-Planck-Institute group in Germany. A detailed description of the resulting macroporous silicon structures can be found in [55]. The group reported the fabrication of long range ordered 2D structures with pore center-to-center distance as low as $1.5\mu m$, and a pore diameter as large as $1.36\mu m$ at a depth of up to $100\mu m$.

Regardless of the process with which such crystals are produced, a tempting question that one must answer is: does the loss of periodicity in the third dimension destroy the usefulness of a 2D crystal and limit its application to being a test ground for physical principles? Apparently not! The point to remember is that despite the lack of periodicity in the third dimension, light can still be contained by total internal reflection when such crystals are sandwiched between two slabs of a relatively large dielectric cladding. Light will, of course, be able to escape at some angles, but this is no worse, at least in principle, than the dielectric wave guides used currently in integrated optics. However, the viability of such wave guides is still a subject of debate in the community. Some studies [56] have suggested drastic improvement in the guiding efficiency over planar dielectric wave guides. It is assumed that when combined with 2D photonic crystal structures, in which line defects have been created, more confinement in the plane of periodicity can be achieved. Such structures will be even more useful for use around sharp corners and bends. Other studies [57] have refuted the argument, and argued that the introduction of such 2D structures in a slab guide merely increases the impedance of the guide

and while the in-plane losses are minimal, large out-of-plane losses cannot be diminished. More recent studies by the MIT group have focused on mapping the 2D band gaps and the resulting defect modes when such crystals are fabricated in finite slabs [58]. Although their calculations show some promising advances, they remain to date purely theoretical predictions.

Photonic crystal fibers

An alterative approach to 2D photonic wave guides was first introduced by a group at Southampton [59]. They proposed the use of a so-called photonic band gap 2D fiber. This was essentially an array of a 2D array of air holes in silica arranged in a hexagonal honeycomb arrangement and mechanically drawn to form a fiber. The idea is then to introduce a defect by either removing one or a bundle of rods such that the general cylindrical symmetry about the axis of the structure is preserved. This opens up an air channel along the axis of the fiber which is then used to guide light.

The advantage is, while conventional optical fibers restrict light to propagating along their axis via total internal reflection, the photonic crystal fibers would essentially accomplish this via the 2D photonic band gap effect, and because the guiding is essentially done in air, this would avoid the major problems associated with the coupling of the radiation in the high index core of the conventional fibers. The greater advantage would be the ability to bend these fibers beyond the threshold bending radius of the conventional optical fibers, where the critical angle conditions are no longer satisfied and the fiber is very lossy. More recent studies were conducted by a group at Corning Inc. [60]. Their studies provide both optimized theoretical and experimental results for both air core and dielectric core band-gap fibers, and have reported very promising outcomes.

A more intriguing approach to wave guiding using 2D photonic crystals was introduced recently by the MIT [61]. In their more recent publication [62], a cylindrical air wave guide was constructed by etching away the core of concentric multi-layer dielectric mirrors which possessed the property of omnidirectional reflection. In their studies, they showed that the lowest order TE mode can propagate in a single mode fashion through even large-core fibers, in

which case other modes are eliminated asymptotically by their large losses and pore coupling. To quite elaborate extents, the group also addressed the issues of dispersion, radiation leakage, material absorption, nonlinearity, bending, acircularity, and interference roughness using leaky modes perturbation and methods. Their results showed that cladding properties such as absorption and nonlinearity could be neglected due to the strong confinement of light in the hollow core. Their observations proved to be extremely promising and fabrication efforts in the optical length scales have been undertaken.

Whether 2D structures will prove to be useful for wave guiding or not is still an open question. Nevertheless, 2D structures have certainly provided a medium for exploring new physics and grounds for testing principles and new ideas.

Symmetry, Topology, and Photonic Gaps

Very early in the development of the field of photonic crystals, it became evident that the refractive index contrast played a vital role in opening up photonic gaps. A minimum value around ~ 3 was found to be the necessary threshold. However, it also became evident that not any periodic arrangement of dielectric scatterers would yield a photonic gap. In fact, only a handful of crystal structures succeeded in doing so. Thus far, all the crystal structures that have yielded a full 3D gap, regardless of size, were found to belong to the so-called A7 family of structures [9]. The *A7* crystals structure consists of a *rhombohedral* lattice with a basis of two atoms situated at the crystal positions $\mathbf{d} = \pm u(\mathbf{a}_1 + \mathbf{a}_2 + \mathbf{a}_3)$, where $\mathbf{a}_1$, $\mathbf{a}_2$, and $\mathbf{a}_3$ are the primitive lattice vectors defined by:

$$\begin{aligned} \mathbf{a}_1 &= a_0\{\varepsilon, 1, 1\},\ \mathbf{a}_2 = a_0\{1, \varepsilon, 1\},\ \text{and}\ \mathbf{a}_3 = a_0\{1, 1, \varepsilon\} \\ \text{with}\ \varepsilon &= 1 - \frac{\sqrt{1 + \cos\alpha - \cos^2\alpha}}{\cos\alpha}. \end{aligned} \tag{1.3}$$

Here, α is the angle between any two primitive lattice vectors. Although all the 3D structures mentioned above seem quite alien to each other, they can all be produced from this group by proper choices of the parameters, α and u. For instance, by choosing $\alpha = 60^0$ and $u = \frac{1}{8}$, we

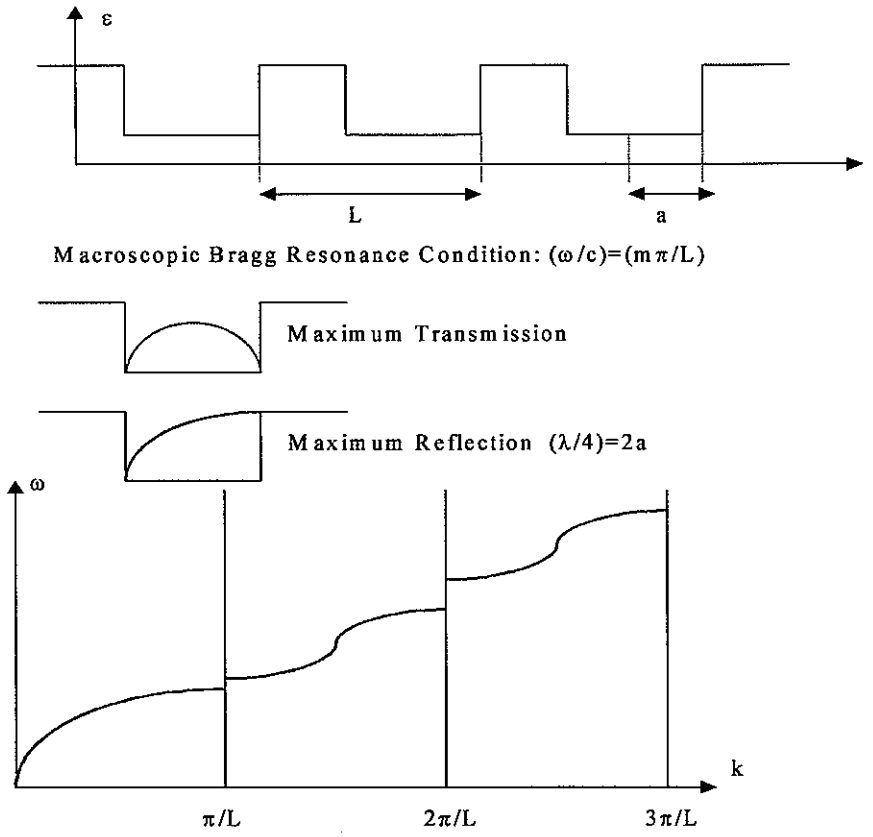

Figure 1.7 Schematic diagram depicting the two different types of scattering mechanisms responsible for photonic gap formation [63].

produce the diamond structure. Setting $\alpha = 60^0$, $u = 0$, and joining up the lattice points by cylinders, we arrive at the Yablonovite structure. Similarly, but with a little more effort, we can generate the ISU layer-by-layer structure, the spiral rod structure, and even the simple cubic structures, by the appropriate choice of parameters. This leads us to the obvious question: what are the necessary crystal symmetry requirements for yielding a photonic gap? In fact, what are the general rules of thumb, if any, that yield a photonic gap? To answer these questions, it is imperative to understand how the photonic gap essentially arises. In the next section we shall follow the argument presented by S. John et al. [63].

Photonic band gap formation can be understood as a "*synergic interplay*" between two distinct resonance scattering mechanisms. One the one hand, there is the *microscopic scattering*

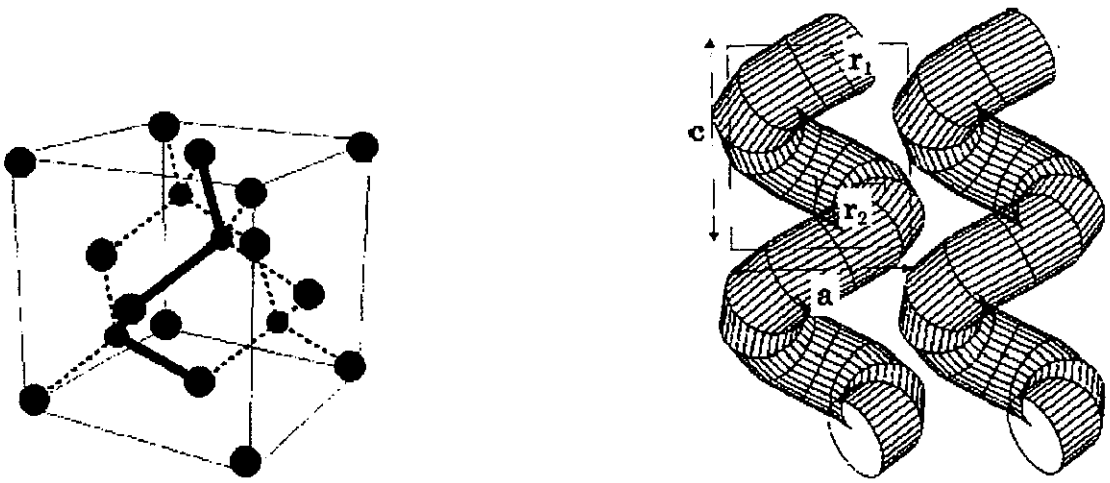

Figure 1.8 Spriral rods defined in a diamond structure by connecting the lattice points along the (001) crystal direction [64].

resonance from the dielectric material contained in a single unit cell of the photonic crystal. On the other hand, there is the *macroscopic resonance* dictated by the geometrical arrangement of the repeating unit cells of the dielectric microstructure.

The first resonance is governed by the local symmetry of the scattering elements. A simple illustration of this is depicted in Fig.1.7. Here, an incoming light wave is scattered from a 1D square potential well. It is clear that transmission is maximized when the wave length of the incoming radiation is equal to the width of the well. On the other hand, if only one-fourth of the wavelength fits in the well, then reflection is maximized. This one-quarter condition is a simple example of the microscopic scattering resonance condition and, as illustrated, depends solely on the local configuration of the scattering center. Conversely, when there is a periodic arrangement of repeating unit cells of the dielectric microstructure, the result is a Bragg type of resonance scattering. This occurs whenever the spacing between adjacent unit cells is an integer multiple of half of the optical wavelength. A photonic band gap is facilitated only if the geometrical parameters of the crystal are such that both the microscopic and macroscopic resonances occur at precisely the same wave length. In addition, both of these scattering mechanisms must be independently quite strong.

Most of the effort set forth has focused on increasing the strength of the macroscopic scattering and, while this has led in one way or another, to the birth of the A7 family of structures, increasing the strength of the microscopic scattering strength, on the other hand, means that one would have to investigate the effect of the local topology of the individual scattering centers. Among the first to investigate the effects of the local structure were the Japanese group, Noda et al. [64]. In fact, they have proposed recently that by carefully choosing the local symmetry of the scattering centers, a photonic band gap can be opened regardless of the periodic macroscopic arrangement they are arranged into. Their idea actually emerged through careful examination of the structures which have thus far yielded photonic gaps. By connecting the lattice points of a structure known to display a photonic band gap along actual material interconnects, they observed that all the previous 3D structures can be viewed as periodic arrangements of twisted rods [64]. Fig.1.8 shows the twisted rod arrangement resulting from connecting the diamond structure lattice points along the $\langle 001 \rangle$ direction. Interestingly, however, They discovered that any periodic arrangements of such twisted rods resulted in a sizable photonic band gap regardless of the underlying symmetry of the lattice constituting the periodic arrangement. Fixing the dielectric contrast to 12.25 : 1, they reported a gap-to-midgap ration ($\frac{\Delta\omega}{\omega}$) up to 16.8% for a SC arrangement of air rods in a dielectric back ground, while a maximum of only 3% was found for dielectric rods in an air background. For an FCC arrangement they obtained maximum gaps of 19.5 and 17.2% for non-touching rods in dielectric and air backgrounds respectively, while a large gap up to 27.5% was observed when the dielectric rods were allowed to overlap. Furthermore, by using a BCC arrangement, they observed respective maximum gaps of 20 and 16.7% for the non-touching rod case in dielectric and air backgrounds, respectively. It is these results that actually motivated the introduction of the tetragonal lattice of square spiral posts suggested by O. Toader and S. John [33, 34] mentioned earlier.

Though these results are quite exciting, one must point out that even after arranging such twisted rods into SC, FCC, or even BCC lattices, and because of the shape of the rods, the overall symmetry remains that of the A7 family! However, what is important is the indirect

implication of this work, namely the realization that "*topology*" does play a vital role in the creation of the gap. Yet, it is not the topology of the individual entities that is of prime importance, rather, that of the high dielectric material, specifically whether it is connected, *network topology,* or disconnected, *cermet topology.* This was first pointed out by Ho et al. [65]. It turns out, as suggested by the above results, as a general rule of thumb, network topology is more favorable for producing large gaps than the cermet topology [66].

The effect of topology on the photonic gaps can be understood by analyzing the fields at the top and bottom of the band gap, specifically by mapping the displacement field intensity [67]. For simplicity, we shall first consider the case of a two-dimensional square lattice of dielectric cylinders in an air background. In this case, one can identify two different polarization states: TE modes, where **E** is in the plane of the crystal and **H** is perpendicular to it, and TM modes, where the opposite is true. Inspection of the band gap diagram of this structure reveals a relatively large photonic gap for the TM modes, while the TE modes are observed to have no gap at all. Examining the displacement field at the top of the lower band (bottom of the photonic gap) for the TM mode, we find it is predominantly concentrated in the dielectric rods and very little leaks into the air regions. Conversely, and because of the mutual orthogonality requirement on successive modes, we find the TM mode residing at the bottom of the upper band (top of the photonic gap) has all of its displacement field predominantly concentrated in to the air regions. However, from the electromagnetic energy density point of view, the concentration of **D** in the high dielectric yields a lower energy configuration than the case where it is mostly in the air. This, in turn, implies that the mode at the bottom of the gap will possess a much lower energy than the upper mode, thereby resulting in a large band gap.

For the TE modes, on the other hand, the situation is completely different. In this case, **E** must remain perpendicular to the rods at all times. Consequently, when the mode at the bottom of the gap tries to concentrate the **D** field in the rods to produce a lower energy configuration, it is frustrated by the boundary conditions which it must obey and instead the field penetrates into the air between the cylinders. The mode at the top of the gap, while maintaining its orthogonality to the former mode, is more or less the same and has all of its

D field in the air regions. The end results is a very small or no energy gap.

Consider now an alternate scenario, instead of isolated high dielectric entities in an air background, we now have a lattice of air holes in a dielectric host. In this case we find that it is the TE modes that possess the large gap, while the TM modes have a sizably smaller gap. The TM modes above and below the gap are observed to both concentrate **D** in the dielectric; in the intersections for the lower mode and in the veins in between for the upper mode. Thus, no large gap is produced. The TE modes, on the other hand, confine the lines of **D** to run along the dielectric channels and avoid the air regions. The upper mode, orthogonal to this, forces the **D** field into the air regions, thus opens up a large gap.

In light of the above discussion, and by extending our analysis to the three-dimensional case, one would understand why a 3D network topology is more favored for large gap production over a 3D cermet one. In a network there will always be some continuous dielectric path into which the **D** field can concentrate in regardless of polarization. The successive mode, which must be orthogonal to this one, will thus be pushed out of the dielectric and into the air regions, thereby producing a configuration in which two successive modes are quite different in their energy values, thus opening up a gap. On the contrary, in a cermet topology this will not be the case, rather, if we have a "*low dielectric host*" with "*high dielectric inclusions*", then the boundary conditions on the fields will always force the penetration of the "*low dielectric*" regions resulting in a reduced gap size or none at all.

Our analysis above certainly agrees with the finding of the Japanese group mentioned previously [64]. In fact, when starting with a parent cermet topology of an FCC lattice of twisted dielectric rods, the observed gap was rather small, compared to the case of the network topology of twisted air rods in a dielectric background. However, when the dielectric rods were allowed to touch and overlap, the topology deviated from the parent cermet to a newborn network and the gap size increased dramatically.

Metallic Photonic Crystals or Structures

Practically increasing the strength of the micro- and macro-scattering resonances implies that the underlying solid material must have a very high refractive index (typically ~ 3), while at the same time exhibits negligible absorption or extinction of the light ($1db/cm$). These conditions, along with the requirement that the individual scattering processes be independently strong along with what topological implications this entails, have severely restricted the set of engineered dielectrics that exhibit a photonic band gap. One suggestion is to use metallic scatterers rather than dielectric ones. Certainly the huge metallic dielectric function would mean that a fewer number of periods are necessary to achieve a photonic band gap effect [68, 69]. However, one must worry about the inherent metallic absorption especially at the optical frequency length scales. Indeed, most of the proposed metallic or metallodielectric photonic crystals have focused on the microwave frequency regions where the absorption is considerably less [70, 71, 72, 73, 74, 75, 76]. However, there are some favorable situations where the redistribution of the photon wave field, due to the periodicity, prevents the metal from absorbing the light [77]. Under such circumstances, "the light sees the metal sufficiently to be scattered by it, but not enough to be absorbed" [77].

Once a photonic crystal contains highly conducting elements such as metals, the possibility of generating local surface currents comes into play, and, as a result, the intertwined roles of topology and polarization change dramatically. As usual, we first start by considering the somewhat simple two-dimensional photonic crystal. Kuzmiak et al. [78] studied the case of an array of infinitely long metallic cylinders arranged in square and triangular lattices embedded in vacuum. Their results showed a striking qualitative difference in the band structures of the two different polarizations.

For the TE modes, they obtained a band structure that was very similar to the free space dispersion except with a number of super-imposed very flat bands. For TM modes, however, the situation was very different. No flat bands were observed, rather a finite cut-off frequency below which no propagating modes existed. To physically understand these observations, we note that while the TM modes can couple to longitudinal oscillations of charge along the length of the

cylinders, because of the orientation of the **E** field, the TE modes, however, cannot. This means there exists a cut-off frequency below which vigorous longitudinal oscillations are generated by an incoming TM polarized radiation, resulting in no propagation. It is worth pointing out that such oscillations do not occur at the bulk plasma frequency, however, because the metal has been diluted by cutting it up into cylinders, rather at an effective plasma frequency which scales with the square root of the filling fraction (essentially the square root of the average electron density). Unable to couple to such longitudinal modes, a TE polarized wave instead excites discrete excitations associated with the isolated cylinders. However, these modes are shifted in frequency and perturbed, due to the interactions between the neighboring cylinders. As a result, they appear in the band structure as a number of very flat, almost dispersionless, bands.

Once again we extend our analysis to 3D structures. In this case, a cermet topology, such as an array of metal spheres, bulk plasma-type of oscillations are not possible because the metal is not continuous; rather, by analogy with the TE modes in two dimensions, both polarizations show the flat bands caused by the interaction of the modes of the individual spheres [2]. In the network topology, on the other hand, collective oscillations throughout the structure are possible for both polarizations. Consequently, the band structure becomes similar to that of the TM modes in two dimensions, producing an effective plasma frequency below which propagation is impossible [68].

The first 3D metallic structure was introduced by Sievenpiper, Sickmiller, and Yablonovitch [71]. They introduced a metal wire structure based on a diamond lattice in the centimeter length scale. Here the structure was created by joining the adjacent lattice points by thick copper wires. In agreement with the above analysis, this network-like structure displayed a forbidden band below a cut-off frequency in the GHz frequency range, as well as a more conventional photonic band gap at a higher frequency resulting from the periodicity of the structure. Defects in the lattice were also introduced, and were observed to allowed modes inside the gap. Almost simultaneously, the ISU group proposed a rather more simple metallic structure [72] constructed from layers of a metallic square mesh separated by layers of a dielectric spacer.

Their results were in qualitative agreement with the wire diamond lattice, once again identifying a finite cut-off frequency below which no modes could propagate. Defects were also introduced by simply cutting the wires; the result was the appearance of allowed modes below the cut-off frequency.

A more theoretically sound investigation of the behavior of such metallic structures was carried out by Pendry [80]. In his calculations, Pendry used the wire diamond structure; however, the diameter of the wires was of the order microns rather than the millimeters of the Yablonovitch structure. His results showed that the effective plasma frequency of the structure is not only controlled by the average electron density, but also by the inductance of the wires. The net effect was a several orders of magnitude increase in the effective mass of the electrons, consequently reducing the plasma frequency. Unlike the Yablonovitch structure which had a plasma frequency of the same order of magnitude as the lattice spacing, in the Pendry structure the square of the plasma frequency was suppressed by a factor of $ln(a/r)$ where a is the lattice spacing and r is the wire radius. The result is that the plasma frequency is shifted far below the frequency at which the primary diffraction effects occur. This prevents diffraction from interfering with the plasma frequency and results in a much cleaner effect supporting the validity of the above arguments.

More recent studies were conducted by McIntosh et al. [81, 82]. In their studies, they proposed the use of an FCC lattice of metallic units embedded in a dielectric background to open up infrared stop bands. Their results showed promising applications for possible IR filters. Because their goal was to design reflection filters, their studies completely overlooked the effect of metallic absorption and focused solely on transmission measurements. The theoretical simulations they provided also assumed lossless metallic conductors. It was unclear from their work whether such metallic structures would ever play a role in any other form of application.

A more welcome study was conducted by Zhang et al. [83]. In their efforts, Zhang et al. showed both theoretically and experimentally that it was possible to realize photonic band gaps using dielectric-coated metallic spheres as building blocks in the GHz frequency regime. Robust photonic band gaps were found to exist, provided that the filling ratio of the spheres

exceeded a certain threshold. However, what was more intriguing about their work was the demonstration of how robust were such metallic generated photonic band gaps and that they were quite immune to random disorders in the global structure symmetry. The group also provided arguments about the possibility of extending their results to the infrared and optical regimes. They assessed that, by proper choice of the coating dielectric spacer and the metal cores, such gaps could be realized in spite of metallic absorption.

Almost immediately after this, the ISU group ([84], see also chapter 7) investigated theoretically the effects of metallic absorption on the photonic band gap in an all metallic photonic crystal. They argued that metals possessed an IR-to-optical window of frequencies in which metallic absorbance is minimal and can, in fact, be negligibly small with a proper choice of the material. They also showed that by proper choice of the metallic crystal parameters, it is possible to avoid the catastrophic metallic absorption region and overlay the photonic band gap with this preferred window. By satisfying both conditions together, it was demonstrated that an incoming electromagnetic radiation would be rejected by the crystal and negligible absorbance would take place. The effect of intentionally introducing defects was also studied. The group demonstrated that the defect induced transmission bands suffered from nearly zero absorbance. This opened the door for a much welcomed progress in the possibility of using defects in metallic photonic crystals as IR and possibly optical waveguides [85].

Soon after, the ISU group, in collaboration with the Sandia National Lab group, designed the first all metallic 3D photonic crystal at IR wavelength scale (see chapter 8). An ISU layer-by-layer crystal was fabricated using tungsten metal; transmission, reflection, and absorbance measurements were performed[86]. Not only did the crystal display a huge photonic band gap attenuation effect, a record high 30db per unit cell, but also provided grounds for a very promising incandescent lamp and thermal photovoltaic applications. They showed a considerable slow down in the speed of light at the photonic band edge, and, as a result, an order of magnitude enhanced absorption was produced. This, however, was not a typical material induced absorbance, as both theoretical calculations and experimental measurements have shown that a slab of tungsten metal produces negligible absorbance at those wavelength

scales. Rather, it appeared that sufficient reduction in the group velocity of light had taken place, allowing for more interaction time with the crystal, and hence increased absorbance. Not only was this the first demonstration of the possibility of slowing down light, they also noted that this extraordinary absorbance narrow peak can be tuned by varying the crystal parameters. Such an absorbance peak would function as an emission band when the structure was properly heated. They argued that the extraordinary large metallic gap would be ideally suited for suppressing broad band blackbody radiation in the infrared [87] and recycling its energy into a selective emission band in the visible spectrum, thus producing an efficient incandescent lamp with minimal or no thermal losses at all!

In an attempt to explain the origin of the prescribed sharp absorbance peak, the ISU group used a modal expansion technique to solve for the field distributions in the various crystal modes [88]. They showed, the wide lowest stop band gap extending to zero frequency is induced not only by the wave guide cut-off attenuation, but also by the coupling of waveguide modes between unit cells in different layers, a global photonic band gap effect. Due to the cavity resonance formed inside the photonic crystal, nearly 100% transmission can be achieved. In contrast, surface plasmons were shown to play a negative role in this resonance, and, hence, were ruled out as possible sources for the experimental observations.

Self Assembled Photonic Crystals or Colliodal Crystals and Photonic Band Gaps

It became apparent very early on, and as we have highlighted throughout the previous sections, that fabricating 3D photonic crystals at optical length scales is both tedious and extremely difficult. In an attempt to overcome this problem, the experimental community turned its attention to what are widely known as self assembled structures [89]. Though hard-sphere like interactions, a colloidal suspensions containing mono-disperse sub-micron spheres minimizes its free energy assembling in short ranged, closed packed FCC clusters [90]. The result is the production of random stacks of hexagonal planes, a structure with intrinsic disorder along the c-axis. Charged colloids, on the other hand, yield well-ordered crystals with the FCC

arrangement [91]. Such structures have been used to demonstrate the inhibition of spontaneous emission of dye molecules dissolved in the solvent between the spheres [92]. The net negative charge of spheres is counterbalanced by the free ions in the solution. Once these ions are removed, the spheres interact both via long range Van der Waals forces, as well as short range electrostatic repulsion. Under favorable conditions the colloid undergoes a phase change from a disordered phase to a crystalline FCC structure.

Provided that the mono-disperse condition ($< 5\%$ radial variation) is satisfied within the suspension, a wide range of sphere radii (from $1nm$ to $10m\mu$) can be used to manufacture such crystals. The resulting lattice constants, on the other hand, appear to be governed by the concentration of spheres. Several groups [93, 94, 95] have produced such crystals with the goal of experimentally studying photonic effects.

A key experimental measurement is that of the Kossel line pattern for a given crystal. This is simply the diffraction pattern produced using a diffuse source at a given frequency. The transmitted light signal produces a series of dark rings, or stop bands, corresponding to angles where the Bragg condition is satisfied for some set of crystal planes. By analogy with the standard crystallography techniques, these patterns are used to identify the lattice type and orientation of the single crystal domains.

A major drawback, however, is the dielectric contrasts in these colloids, typically about 1:4. Unfortunately, this is much too small to produce complete band gaps. One idea is to utilize spheres with a high dielectric core. The question, of course, is whether this can be done while maintaining the mono-dispersion criterion.

Another possibility is to increase the dielectric constant of the solvent. In other words, use the colloidal crystal as a template. One such early attempt resulted in an interconnected network of uniform pores in a titania background [96]. Though no long range crystalline order was achieved, the technique proved ground breaking for the production of uniform pores in a dielectric background. Following this, a number of groups modified the approach to first synthesizing ordered silica or polystyrene spheres, then infiltrating with an appropriate material with a relatively large refractive index, and finally removing the spheres either by chemical

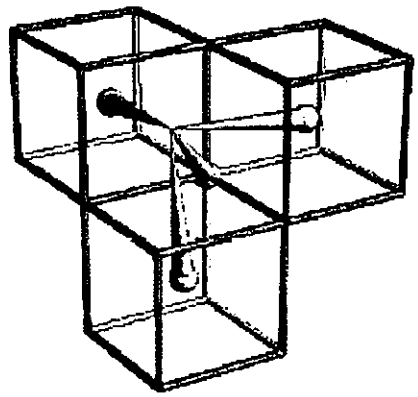

Figure 1.9 Beam geometry for an f.c.c. interference pattern [108].

etching or firing. Several different materials have been attempted including solgels and ceramic precursors [97, 98, 99, 100], metals and polymers [101, 102, 103, 104], as well as semiconducting nano-particles [105]. A further technique is to introduce a high index background material during the process of colloidal crystallization. This latest approach was undertaken by the ISU group and succeeded in producing long range ordered FCC thin films on the order of centimeters [106, 107].

In spite of all the development and successes in the field of inverse opals, their direct application in the design of photonic crystals is still unclear. Aside from being used as possible reflection coatings, to date it is very difficult to intentionally introduce and control defects during or after the crystallization process. As a result, it remains unclear whether such crystals will make it into the realm of possible photonic devices or will remain merely grounds for fundamental physical research.

Photonic Crystals Through Lithographic Holography

The experimental techniques described thus far have focused on the use of various etching and other lithographic techniques to create a periodic structure by removing material, more or less, from a solid block. These techniques have the potential to combine the size of the colloidal crystal with the controlled order of layer-by-layer assembly, yet they are both

tedious and extremely time consuming. A more elegant approach was introduced by Berger, Gauthier-Lafaye, and Costard [108]. They argued that photonic crystals can be viewed as holograms with extremely high refractive index contrasts. Since the refractive index function was successfully approximated by a finite number of plane waves [20], it is therefore possible to construct such a crystal via holographic recording using a finite number of plane waves. The group theoretically investigated the feasibility of their approach to a number of photonic structures, but succeeded only in experimentally fabricating a 2D triangular lattice.

Very recently, however, a group at Oxford University described how such a process can be extended to fabricate 3D structures using only four intersecting laser beams [109]. The resulting interference pattern is then used to illuminate a photoresist. The high intensity regions in the interference pattern render the photoresist soluble, allowing the 3D periodic template to be formed Figs.1.9 and 1.10. Inverse structures can then be formed by infiltrating the template. This simple, yet elegant, holographic technique may hold the key to fabricating the much desired and superior diamond lattice. It also possesses the viability, at least in principle, to create a variety of crystal structures by simply varying the relative orientation and polarization of the four laser beams. It also has the advantage of speed, since the entire pattern in the photoresist is created in nanoseconds. However, it remains to test to what extent ideal defect-free structures can be experimentally realized, how absorption of the laser beams affects uniformity in thickness, and how intentional defects can be incorporated in the resulting template.

Tunable Photonic Crystals

A question that has for long baffled the community was the possibility of optical switching. The essential difficulty arises from the fact that to design a viable optical switch, one must find a way of varying the optical properties of the resulting structure. In other words, be able to tune and move the band gap from one frequency range to another. This, in turn, implies the ability to vary the lattice constant of a realized structure and or its refractive index. Thus far, however, all of the fabrication methods proposed produced photonic band gap structures

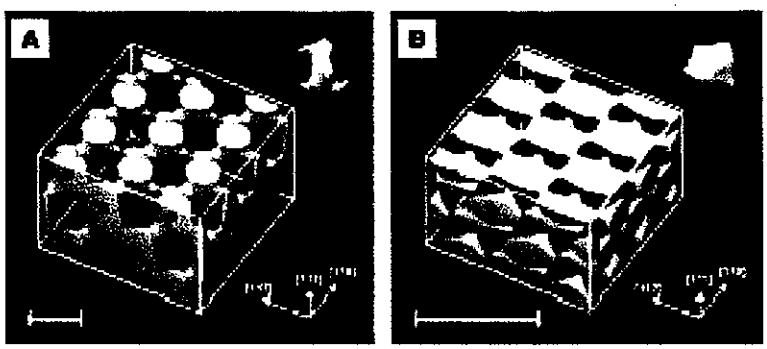

Figure 1.10 Calculated constant-intensity surfaces in four-beam laser interference patterns designed to produce photonic crystals for the visible spectrum from photoresist. The primitive basis (contents of a Wigner-Seitz unit cell) is shown inset in each case [108].

with fixed crystal dimensions and refractive indices.

Recently, the MIT group proposed the use of block copolymers as self assembling building blocks for 1D, 2D, and 3D photonic crystals [110]. By controlling the composition, molecular weight, and architecture of the macromolecules, the resulting equilibrium phase can be molded into a rich repertoire of equilibrium phase periodic structures. Possible assembled structures include alternating molecular layers, complex topologically connected cubics, cylinders on a hexagonal lattice, and spheres on a body-centered lattice. In addition to providing the topologically preferred network topology, such molecules provide also strikingly flexible structures in as much as plastics. This means that by applying an appropriate mechanical stress within the elastic limits, one can change the lattice constant of the assembled structure, thereby changing both the location and the size of the photonic gap. Thus far, the group has only been successful in fabricating 1D crystals using this technique. However, efforts continue for producing such structures in 2D and 3D configurations.

A more recent attempt at tunable photonic crystals was undertaken by John and Busch [111, 112, 113]. Their idea was based on infiltrating an inverse opal structure with an optically birefringent nematic liquid crystal. The resulting composite material was shown to exhibit a completely tunable photonic gap. In particular, it was shown that such a 3D gap can be

completely opened or closed by applying an electric field of appropriate strength. Such an electric field would act to rotate the axis of the nematic molecules relative to the inverse opal backbone, thereby changing the refractive index contrast, and, hence, the gap size.

Modeling and Numerical Methods

Early on, it became apparent that a sound fundamental foundation was needed to aid and guide the experimental efforts. Certain requirements or expectations, however, were imposed by the preliminary experimental efforts. Among these "adequate theory requirements" where to:

- produce a detailed map of the energy band diagram to aid the search and discover the viability of new photonic crystals.
- estimate experimentally measurable quantities, e.g., the transmission, reflection, and absorption spectra, for the sake of touching base with the realistic limitations of imperfect samples.
- simulate the real time evolution of the electromagnetic fields in the proposed structures for the sake of testing possible devise applications and feasibility.
- provide deep physical insight in to the physical origins of photonic features to better aid the development of potential applications.

In the next few chapters we will highlight some of the most widely used full 3D techniques used in the investigation of photonic crystal research and applications and describe briefly the major theoretical techniques used in the investigation of photonic crystal research and applications. The Plane Wave Expansion Method, the Transfer Matrix Method, and the Finite Difference Time Domain Method will be addressed. In an attempt to paint a detailed picture of a potential PBG-crystal application, each method has both an advantage that it offers as well as a drawback that limits its use. We will present a brief explanation of the physics underlying each approach, as well as a comparative study of the strengths and weaknesses of each

method. Simulations and results obtained by these methods will be presented and discussed. A new theoretical approach, the so-called Modal Expansion Method, will be presented. This method offers a much more comprehensive study of PBG-crystals as compared to the previous approaches, as well as limited weaknesses. The beauty of this technique is that it is tailored to the silicon processing and machining techniques. Preliminary results obtained using this new approach are presented and compared to its peers.

Bibliography

[1] *Photonic Band Gaps and Localization*, NATO ASI Series B, Vol. **308**. Ed. C. M. Soukoulis.

[2] *Photonic Band Gap Materials*, NATO ASI Series E, Vol. **315**. Ed. C. M. Soukoulis.

[3] *Photonic Crystals and Light Localization in the 21st Century*, NATO ASI Series C, Vol. **563**. Ed. C. M. Soukoulis

[4] K. Sakoda, *Optical Properties of Photonic Crystals*, 2001, Springer, Verlag New York Inc.

[5] J. D. Joannopoulos, R. D. Meade, J. N. Winn, *Photonic Crystals: Molding the Flow of Light*, 1995, Princeton University Press.

[6] Born and Wolf, *Principles of Optics*, Pergamon Press, p66-70.

[7] S. John, in *Photonic Band Gap Materials*, NATO ASI Series E, Volume **315**. Ed. C. M. Soukoulis.

[8] E. R. Brown, C. D. Paker, O. B. McMahon, 1994, *Appl. Phys. Lett.* **64** 3345.

[9] S. D. Cheng, R. Biswas, E, Ozbay, S. McCalmont, G. Tuttle, K. M. Ho, 1995, *Appl. Phys. Lett.* **67** 3399.

[10] R. Biswas, E. Ozbay, B. Temelkuran, M. Bayindir, M. M. Sigalas, K. H. Ho, *Photonic Crystals and Light Localization in the 21st Century*, NATO ASI Series C, Vol. **563**. Ed. C. M. Souklous.

[11] I. El-Kady, M.M. Sigalas, R. Biswas, K. M. Ho, 1999, *J. Lightwave Technol.* **17** 2042.

[12] M. Scalora, J. P. Dowling, C. M. Bowden, M. J. Bloemer, 1994, *Phys. Rev. Lett.* **73** 1368.

[13] E. Yablanovitch, 1987, *Phys. Rev. Lett.* **58** 2059.

[14] S. John, 1987, *Phys. Rev. Lett.* **58** 2486.

[15] E. Yablonovitch, T. J. Gmitter, 1989, *Phys. Rev. Lett.* **63** 1950.

[16] S. Satpathy, Z. Zhang, M. R. Salehpour, 1990, *Phys. Rev. Lett.* **64** 1239.

[17] K. M. Leung, Y. F. Liu, 1990, *Phys. Rev. B 41* 10 188.

[18] K. M. Leung, Y. F. Liu, 1990, *Phys. Rev. Lett.* **65** 2646.

[19] Z. Zhang, S. Satpathy, 1990, *Phys. Rev. Lett.* **65** 2650.

[20] K. M. Ho, C. T. Chang, C. M. Soukoulis, 1990, *Phys. Rev. Lett.* **65** 3152.

[21] H. S. Sozuer, J. W. Haus, 1993, *J. Opt. Soc. Am. B* **10** 296.

[22] J. Maddox, 1990, *Nature* **348** 481.

[23] E. Yablonovitch, T. M. Gmitter, K. M. Leung, 1991, *Phys. Rev. Lett.* **67** 2295.

[24] K. M. Ho, C. T. Chan, C. M. Soukoulis, R. Biswas, M. Sigalas, 1994, *Solid State Commun.* Vol. **89**, 413.

[25] S. Y. Lin, J. G. Fleming, D. L. Hetherington, B. K. Smith, R. Biswas, K. M. Ho. M. M. Sigalas, W. Zubrzycki, S. R. Kurtz, J. Bur, 1998. *Nature*, Vol. **394**, 251.

[26] M. M. Sigalas, R. Biswas, K. M. Ho, C. M. Soukoulis, D. D.Crouch, *Proc. 14th Ann. Rev. Progr. Appl. Compuational Electrodynamics,* 1998, Vol. **1**, 144.

[27] S. Noda, M. Imada, A. Chutinan, N. Yamamoto, in *Photonic Crystals and Light Localization in the 21st Century*, NATO ASI Series C, Vol. **563**, Ed. C. M. Soukoulis.

[28] H. S. Sozuer, J. P. Dowling, 1994, *J. Mod. Opt.* **41** 231.

[29] S. Noda, N. Yamamoto, M. Imada, H. Kobayashi, M. Okano, 1999, *J. Lightwave Technol.* **17** 1948.

[30] Transfer Matricies, Photonic BAnds, and related quantities, Ph.D. Thesis, Imperial Collage, London, 1996, Ed. A. J. Ward.

[31] S. Fan, P. R. Villeneuve, R. D. Meade, J. D. Joannopoulos, 1994, *Apl. Phys. Lett.* **65** 1466.

[32] S. Fan, P. R. Villeneuve, J. D. Joannopoulos, 1995, *J. Appl. Phys.* **78** 1415.

[33] A. Blanco, E. Chomski, S. Grabtchak, M. Ibisate, S. John, S. W. Leonard, F. L. Meseguer, H. Miguez, J. P. Mondia, G. A. Ozin, O. Toader, H. M. Van Driel, 2000, *Nature* Vol. **405** 437.

[34] S. R. Kennedy, M. J. Brett, O. Toader et al., 2002 *Nano Lett.* **2 (1)** 59.

[35] K. Robbie, M. J. Brett, 1996, *Nature* **384** 616.

[36] K. Robbie, J. C. Sit, M. J. Brett, J. Vac, 1998, *Sci. Technol. B* **16** 1115.

[37] M. Plihal, A. Shambrook, A. A. Maradudin, P. Sheng, 1991, *Opt. Comm.* **89** 199.

[38] M. Plihal, A. A. Maradudin, 1991, *Phys. Rev. B* **44** 8565.

[39] P. R. Villeneuve, M. Piche, 1991, *J. Opt. Soc. Am.* **A8** 1296.

[40] S. L. McCall, P. M. Platzman, R. Dichaouch, D. Smith, S. Schultz, 1991, *Phys. Rev. Lett.* **67** 2017.

[41] R. D. Meade, K. D. Brommer, A. M. Rappe, J. D. Joannopoulos, 1992, *Appl. Phys. Lett.* **61** 495.

[42] D. Cassange, C. Jouanin, D. Bertho, 1996, *Phys. Rev. B* **53** 7134.

[43] H. Kosaka, T. Kawashima, A. Tomita, M. Notomi, T. Tamamura, T. Sato, S. Kawakami, 1999, *J. Lightwave Technol.* **17** 2032.

[44] D. Labiloy, H. Benisty, C. Weisbuch, T. F. Krauss, R. M. De La Rue, V. Bardinal, R. Houdre, U. Oesterle, D. Cassagne, C. Jouanin, 1997, *Phys. Rev. Lett.* **79** 4147.

[45] J. D. Joannopoulos, S. Fan, A. Mekis, S. G. Johnson, in *Photonic Crystals and Light Localization in the 21st Century*, NATO ASI Series C, Vol. **563**. Ed. C. M. Soukoulis.

[46] W. M. Robertson, G. Arjavalingam, R. D. Meade, K. D. Brommer, A. M. Rappe, J. D. Joannopoulos, 1992, *Phys. Rev. Lett.* **68** 2023.

[47] R. D. Meade, K. D. Brommer, A. M. Rappe, J. D. Joannopoulos, 1992, *Appl. Phys. Lett.* **61** 495.

[48] M. Sigalas, C. M. Soukoulis, C. T. Chan, K. M. Ho, 1993, *Phys. Rev. B* **48** 14121.

[49] M. Sigalas, C. M. Soukoulis, C. T. Chan, D. Turner, 1996, *Phys. Rev. B* **53** 8340.

[50] S. L. McCall, P. M. Platzman, R. Dalichaouch, D. Smith, S. Schultz, 1991, *Phys. Rev. Lett.* **67** 2017.

[51] J. R. Wendt, G. A. Vawter, P. L. Gourley, T. M. Brennan, B. E. Hammons, 1993, *J. Vac. Sci. Technol. B* **11** 2637.

[52] P. L. Gourley, J. R. Wendt, G. A. Vawter, T. M. Brennan, B. E. Hammons, 1994, *Japan, J. Appl. Phys.Pt 2* **33** L1463.

[53] H. W. Lau, J. G. Parker, R. Greef, M. Holling, 1995, *Appl. Phys. Lett.* **67** 1877.

[54] U. Gruning, V. Lehmann, S. Ottow, K. Busch, 1996, *Appl. Phys. Lett.* **68** 747.

[55] A. Birne, R. B. Wehrspohn, U. M. Gosele, K. Busch, 2001, *Adv. Mater.* **13** 377.

[56] R. D. Meade, A. M. Rappe, K. D. Brommer, J. D. Joannopoulos, 1993, *J. Opt. Soc. Am. B* **10** 328.

[57] I. El-Kady, M. M. Sigalas, R. Biswas, K. M. Ho, 1999, *J. Lightwave Technol.* **17** 2042.

[58] S. G. Johnson, S. Fan, P. R. Villeneuve, J. D. Joannopoulos, 1999, *Phys. Rev. B* **60** 5751.

[59] T. A. Birks, D. M. Atkin, G. Wylangowski, P. St. J. Russel, in *Photonic Band Gap Materials*, NATO ASI Series E, Vol. **315**. Ed. C. M. Soukoulis.

[60] D. C. Allan, J. A. West, J. C. Fajardo, T. J. Michael, K. W. Koch, N. F. Borrelli, in *Photonic Crystals and Light Localization in the 21st Century*, NATO ASI Series C, Vol. **563**. Ed. C. M. Souklous.

[61] Y. Fink, D. J. Ripin, S. Fan, C. Chen, J. D. Joannopoulos, E. L. Tomas, 1999, *J. Lightwave Technol.* **17** 2039.

[62] S. G. Johnson, M. Ibanescu, M. Skorobogatiy, O. Weisberg, T. D. Engeness, M. Soljacic, S. A. Jacobs, J. D. Joannopoulos, Y. Fink, 2001, *Opt. Express* **9** 748.

[63] S. John, O. Toader, K. Busch

[64] A. Chutinan, S. Noda, 1997, *Phys. Rev. B* **57** 2006.

[65] K. M. Ho, C. T. Chan, C. M. Soukoulis, in *Photonic Band Gaps and Localization*, NATO ASI Series B, Vol. **308**. Ed. C. M. Souklous.

[66] Economou E N, Sigalas M M, 1993, Phys. Rev. B 48 13434.

[67] Meade R D, Rappe A M, Brommer K D, Joannopoulos J D, 1993, J. Opt. Soc. Am. B 10 328.

[68] M. M. Sigalas, C. T. Chan, K. M. Ho, C. M. Soukoulis, 1995, *Phys. Rev. B* **52** 11744.

[69] S. Fan, P. R. Villeneuve, J. D. Joannopoulos, 1994, *Phys. Rev. B* **54** 11245.

[70] E. R. Brown, O. B. McMahon, 1995, *Appl. Phys. Lett.* **67** 2138.

[71] D. F. Sievenpiper, M. E. Sickmiller, E. Yablonovitch, 1996, *Phys. Rev. Lett.* **76** 2480.

[72] J. S. McCalmont, M. Sigalas, G. Tuttle, K. M. Ho, C. M. Soukoulis, 1996, *Appl. Phys. Lett.* **68** 2759.

[73] M. M. Sigalas, G. Tuttle, K. M. Ho, C. M. Soukoulis, 1996, *Appl. Phys. Lett.* **69** 3797.

[74] A. Kao, K. A. McIntosh, O. B. McMahon, R. Atkins, S. Verghese, 1998, *Appl. Phys. Lett.* **73** 145.

[75] C. Jin, B. Cheng, B. Man, D. Zhang, S. Ban, B. Sun, L. Li, X. Zhang, Z. Zhang, 1999, *Appl. Phys. Lett.* **75** 1201.

[76] M. M. Sigalas, R. Biswas, K. M. Ho, C. M. Soukoulis, 1999, *Phys. Rev. B* **60** 4426.

[77] A. J. Ward, J. B. Pendry, W. Stewart, 1995, *J. Phys.: Condens. Matter* **7** 2217.

[78] V. Kuzmiak, A. A. Maradudin, F. Pincemin, 1994, *Phys. Rev. B* **50** 16835.

[79] J. B. Pendry, 1994, *J. Mod. Optics* **41** 209.

[80] J. B. Pendry, A. J. Holden, W. J. Stewart, I. Youngs, 1996, *Phys. Rev. Lett.* **76** 4773.

[81] K. A. McIntosh, L. J. Mahoney, K. M. Molvar, O. B. McMahon, S. Verghese, M. Rothschild, E. R. Brown, 1997, *Appl. Phys. Lett.* **70** 2937.

[82] J. A. Oswald, B.-I. Wu, K. A. McIntosh, L. J. Mahoney, S. Verghese, 2000, *Appl. Phys. Lett.* **77** 2098.

[83] W. Y. Zhang, X. Y. Lei, Z. L. Wang, D. G. Zheng, W. Y. Tam, C. T. Chan, P. Sheng, 2000, *Phys. Rev. Lett.* **84** 2853.

[84] I. El-Kady, M. M. Sigalas, R. Biswas, K. M. Ho, C. M. Soukoulis, 2000, *Phys. Rev. B* **62** 15299.

[85] Z.-Y. Li, I. El-Kady, K. M. Ho. To be Published.

[86] S. Y. Lin, J. Bur, Z.-Y. Li, I. El-Kady, K. M. Ho,To be Published.

[87] S. Y. Lin, J. G. Fleming, E. Chow, J. Bur, 2000, *Phys. Rev. B* **62** R2243.

[88] Z.-Y. Li, I. El-Kady, K. M. Ho, 2002, *Phys. Rev.B* In Review.

[89] W. Luck, M. Klier, H. Wesslau, 1963, *Naturwissenschaften* **50** 485.

[90] K. Busch, S. John, 1998, *Phys. Rev. E* **58** 3896.

[91] J. E. G. Wijnhoven, L. Bechger, W. L. Vos, 2001, *Chem. Mater.* **13** 4486.

[92] J. Martorell, N. M. Lawandy, 1990, *Phys. Rev. Lett.* **65** 1877.

[93] I. I. Tarhan, M. P. Zinkin, G. H. Watson, 1995, Optics Lett. **20** 1571.

[94] I. I. Tarhan, G. H. Watson, 1996, *Phys. Rev. Lett.* **76** 315.

[95] W. L. Vos, R. Sprik, A. Lagendijk, G. H. Wegdam, A. V. Blaaderen, A. Imhof , in *Photonic Band Gap Materials*, NATO ASI Series E, Vol. **315**. Ed. C. M. Soukoulis

[96] A. Imhof, D. J. Pine, 1997, *Nature* **389** 948.

[97] J. E. G. Wijnhoven, W. L. Vos, 1998, *Science* **281** 802.

[98] A. Zakhidov, R. H. Baughman, et al., 1998, *Science* **282** 897.

[99] B. T. Holland, C. F. Blanford, A. Stein, 1998, *Science* **281** 538.

[100] A. Velev, T. A. Jede, R. F. Lobo, A. M. Lenhoff,1997, *Nature* **389** 448.

[101] P. Jiang, J. Cizeron, J. F. Bertone, V. L. Colvin, 1999, *J. Chem Soc. Am.* ***121*** 7957.

[102] P. Jiang, K. S. Hwang, D. M. Mittleman, J. F. Bertone, V. L. Colvin, 1999, *J. Chem Soc. Am.* ***121(50)*** 11630.

[103] S. H. PArk, Y. Xia,1998, *Adv. Mater.* **10(13)** 1045.

[104] O. D. Velev, P. M. Tessier, A. M. Lenhoff, E. W. Kaler, 1997, *Nature* **401** 548.

[105] Y. A. Vlasov, N. Yao, D. J. Norris, 1999, *Adv. Mater.* **11(2)** 165.

[106] G. Subramania, K. Constant, R. Biswas, M. Sigalas, K. M. Ho, 1999, *Appl. Phys. Lett* **74** 3933.

[107] G. Subramania, K. Constant, R. Biswas, M. Sigalas, K. M. Ho,1999, *J. Lightwave Technol.* **17** 1970.

[108] V. Berger, O. Guathier-Lafaye, E. Costard, 1997, *J. Appl. Phys.* **82(1)** 60.

[109] M. Campbell, D. N. Sharp, M. T. Harrison, R. G, Denning, A. J. Turberfiel, 2000, *Nature* **404** 53.

[110] Y. Fink, A. M. Urbas, M. G. Bawindi, J. D. Joannopoulos, E. L. Thomas, 1999, *J. Lightwave Technol.* **17** 1963.

[111] S. John, K. Busch, 1999, *J. Lightwave Technol.* **17** 1931.

[112] S. John, T. Quang, 1997, *Phys. Rev. Lett.* **78** 1888.

[113] K. Busch, S. John, 1999, *Phys. Rev. Lett.* **83** 967.

2 Finding Photonic Band Structures: The Plane Wave Expansion Method

In this chapter we present a detailed derivation of the Plane Wave (PW) expansion method, and the physics underlying it. This method was first introduced by Ohtaka et al. [1], and later implemented by Leung and Liu [2], and Zhang and Satpathy [3]. The version we present here, however, is due primarily to Ho et al [4] which, as we shall see, automatically incorporates the transverse requirements that must be imposed on the solutions of Maxwell's equations, while at the same time dealing with pure Hermitian operators. As we have pointed out in earlier sections, this method is used primarily for mapping the band structure of photonic crystals. Our goal is to provide the reader with the theoretical foundation of this method, and to present a brief explanation of its underlying physics. A highlight of the major strengths as well as the limitations and drawbacks of this technique will also be summarized.

Plane Wave Expansion Concept

To formulate our eigenvalue problem, we start from the fundamental Maxwell's equations for source free medium:

$$\nabla \cdot \mathbf{D}(\mathbf{r},t) = 0, \tag{2.1}$$

$$\nabla \cdot \mathbf{B}(\mathbf{r},t) = 0, \tag{2.2}$$

$$\nabla \times \mathbf{E}(\mathbf{r},t) = -\frac{\partial}{\partial t}\mathbf{B}(\mathbf{r},t), \tag{2.3}$$

$$\nabla \times \mathbf{H}(\mathbf{r},t) = \frac{\partial}{\partial t}\mathbf{D}(\mathbf{r},t). \tag{2.4}$$

where $\mathbf{E}$ is the electric field, $\mathbf{H}$ is the magnetic field, $\mathbf{B}$ is the magnetic induction, and $\mathbf{D}$ is the electric displacement. Assuming a non-magnetic isotropic dielectric medium, one can write:

$$\mathbf{B}(\mathbf{r},t) = \mu_0 \mathbf{H}(\mathbf{r},t), \tag{2.5}$$

$$\mathbf{D}(\mathbf{r},t) = \varepsilon_0 \varepsilon(\mathbf{r}) \mathbf{E}(\mathbf{r},t). \tag{2.6}$$

Where μ_0 and ε_0 are the permeability and permittivity of free space, respectively, and $\varepsilon(\mathbf{r})$ is the relative dielectric constant of the medium, chosen here to be a real position dependent function. Furthermore, by assuming a harmonic time dependent form $e^{-i\omega t}$ for the fields, the two curl Equations (2.3) and (2.4) reduce to:

$$\nabla \times \mathbf{E}(\mathbf{r},t) = i\omega\mu_0 \mathbf{H}(\mathbf{r},t), \tag{2.7}$$

$$\nabla \times \mathbf{H}(\mathbf{r},t) = -i\omega\varepsilon_0 \varepsilon(\mathbf{r}) \mathbf{E}(\mathbf{r},t). \tag{2.8}$$

Eliminating $\mathbf{E}(\mathbf{r},t)$ in favor of $\mathbf{H}(\mathbf{r},t)$ in Equations (2.7) and (2.8) and rearranging we obtain;

$$\left[\nabla \times \left(\frac{1}{\varepsilon(\mathbf{r})}\nabla\times\right)\right] \mathbf{H}(\mathbf{r}) = \left(\frac{\omega}{c}\right)^2 \mathbf{H}(\mathbf{r}), \tag{2.9}$$

where $c = \frac{1}{\sqrt{\mu_0 \varepsilon_0}}$ is the speed if light in vacuum. Equation (2.9) is the desired eigenvalue equation of the magnetic field vector. It is worth noting that one could have eliminated the magnetic field in favor of the electric field to obtain the analogous eigenvalue equation for the electric field, in which case, the resulting operator enclosed in square brackets, on the left-hand side would have not been Hermitian as in the above equation. To further simplify this equation, we exploit the periodicity of the structure, specifically that of the dielectric function, namely;

$$\varepsilon(\mathbf{r}+\mathbf{a}_i)=\varepsilon(\mathbf{r}), \tag{2.10}$$

where $\mathbf{a}_i$ are the primitive lattice vectors. This allows us to expand the inverse of the dielectric function appearing in Equation (2.9) in a Fourier series of plane waves of the form;

$$\frac{1}{\varepsilon(\mathbf{r})}=\sum_{\mathbf{G}}\varepsilon^{-1}(\mathbf{G})e^{i\mathbf{G}.\mathbf{r}}, \tag{2.11}$$

where $\mathbf{G}$ is a reciprocal lattice vector constructed by any linear vector combination of the primitive reciprocal lattice vectors $\{\mathbf{b}_i; i=1,2,3\}$, the latter defined by;

$$\mathbf{b}_i\cdot\mathbf{a}_i=2\pi\delta_{ij}. \tag{2.12}$$

Taking the Fourier transform of Equation (2.9) and using (2.10), we obtain:

$$(\mathbf{k}+\mathbf{G})\times\left[\sum_{G,G^{\backslash}}\varepsilon^{-1}_{G,G^{\backslash}}\,(\mathbf{k}+\mathbf{G})\times\mathbf{H}_{G^{\backslash}}\right]=\left(\frac{\omega}{c}\right)^2\mathbf{H}_G. \tag{2.13}$$

To impose the transverse condition on the fields mandated by Equations (2.1) and (2.2), we express the magnetic field vector as a vector sum over vectors orthogonal to the relevant$(\mathbf{k}+\mathbf{G})$;

$$\mathbf{H}_G=\sum_{\lambda}h_{G,\lambda}\widehat{\mathbf{e}}_{\lambda}, \tag{2.14}$$

where the $\widehat{\mathbf{e}}_{\lambda}$'s are the pair of unit vectors perpendicular to $(\mathbf{k}+\mathbf{G})$. Together, these three form a right-handed set satisfying

$$\begin{aligned}(\mathbf{k}+\mathbf{G})\times\widehat{\mathbf{e}}_1 &= |\mathbf{k}+\mathbf{G}|\times\widehat{\mathbf{e}}_2, \qquad (2.15)\\ &\textit{and}\\ (\mathbf{k}+\mathbf{G})\times\widehat{\mathbf{e}}_2 &= -|\mathbf{k}+\mathbf{G}|\times\widehat{\mathbf{e}}_1.\end{aligned}$$

Substituting (2.15) into (2.14) we get

$$-(\mathbf{k}+\mathbf{G})\times\left[\sum_{G\backslash,\lambda\backslash}\varepsilon^{-1}_{G,G\backslash}\,(\mathbf{k}+\mathbf{G})\times h_{G\backslash,\lambda\backslash}\widehat{\mathbf{e}}_{\lambda\backslash}\right]=\left(\frac{\omega}{c}\right)^2\sum_{\lambda}\mathbf{h}_{G,\lambda}\widehat{\mathbf{e}}_{\lambda}. \tag{2.16}$$

Taking the dot product of each side with $\widehat{\mathbf{e}}_{\mu}$ gives

$$\left(-(\mathbf{k}+\mathbf{G})\times\left[\sum_{G\backslash,\lambda\backslash}\varepsilon^{-1}_{G,G\backslash}\,(\mathbf{k}+\mathbf{G})\times h_{G\backslash,\lambda\backslash}\widehat{\mathbf{e}}_{\lambda\backslash}\right]\right)\cdot\widehat{\mathbf{e}}_{\mu}=\left(\frac{\omega}{c}\right)^2 h_{G,\mu}. \tag{2.17}$$

Rewriting μ as λ and rearranging we get

$$\sum_{G\backslash,\lambda\backslash}\mathbf{H}^{\lambda\lambda\backslash}_{G,G\backslash}h_{G\backslash,\lambda\backslash}=\left(\frac{\omega}{c}\right)^2 h_{G,\boldsymbol{\lambda}}, \tag{2.18}$$

where

$$H^{\lambda\lambda\backslash}_{G,G\backslash}=-\varepsilon^{-1}_{G,G\backslash}\left[(\mathbf{k}+\mathbf{G})\times(\mathbf{k}+\mathbf{G})\times\widehat{\mathbf{e}}_{\boldsymbol{\lambda}\backslash}\right]\cdot\widehat{\mathbf{e}}_{\boldsymbol{\lambda}}. \tag{2.19}$$

Though the expression in (2.18) and (2.19) looks quite more complicated than the one we initially started with, Equation (2.19) actually simplifies with the aid of (2.15) to a rather simple form

$$\begin{aligned}
\mathbf{H}^{\lambda\lambda\backslash}_{G,G\backslash} &= -\varepsilon^{-1}_{G,G\backslash}\begin{pmatrix}\left[(\mathbf{k}+\mathbf{G})\times(\mathbf{k}+\mathbf{G}^{\backslash})\times\widehat{\mathbf{e}}_{1\backslash}\right]\cdot\widehat{\mathbf{e}}_{1} & \left[(\mathbf{k}+\mathbf{G})\times(\mathbf{k}+\mathbf{G}^{\backslash})\times\widehat{\mathbf{e}}_{2\backslash}\right]\cdot\widehat{\mathbf{e}}_{1}\\ \left[(\mathbf{k}+\mathbf{G})\times(\mathbf{k}+\mathbf{G}^{\backslash})\times\widehat{\mathbf{e}}_{1\backslash}\right]\cdot\widehat{\mathbf{e}}_{2} & \left[(\mathbf{k}+\mathbf{G})\times(\mathbf{k}+\mathbf{G}^{\backslash})\times\widehat{\mathbf{e}}_{2\backslash}\right]\cdot\widehat{\mathbf{e}}_{2}\end{pmatrix}\\
&= -\varepsilon^{-1}_{G,G\backslash}\left|\mathbf{k}+\mathbf{G}^{\backslash}\right|\begin{pmatrix}-(\mathbf{k}+\mathbf{G})\times\widehat{\mathbf{e}}_{2\backslash}\cdot\widehat{\mathbf{e}}_{1} & (\mathbf{k}+\mathbf{G})\times\widehat{\mathbf{e}}_{1\backslash}\cdot\widehat{\mathbf{e}}_{1}\\ -(\mathbf{k}+\mathbf{G})\times\widehat{\mathbf{e}}_{2\backslash}\cdot\widehat{\mathbf{e}}_{2} & (\mathbf{k}+\mathbf{G})\times\widehat{\mathbf{e}}_{1\backslash}\cdot\widehat{\mathbf{e}}_{2}\end{pmatrix}\\
&= -\varepsilon^{-1}_{G,G\backslash}\left|\mathbf{k}+\mathbf{G}^{\backslash}\right|\left|\mathbf{k}+\mathbf{G}\right|\begin{pmatrix}\widehat{\mathbf{e}}_{2}\cdot\widehat{\mathbf{e}}_{2\backslash} & -\widehat{\mathbf{e}}_{2}\cdot\widehat{\mathbf{e}}_{1\backslash}\\ -\widehat{\mathbf{e}}_{1}\cdot\widehat{\mathbf{e}}_{2\backslash} & \widehat{\mathbf{e}}_{1}\cdot\widehat{\mathbf{e}}_{1\backslash}\end{pmatrix}.
\end{aligned} \tag{2.20}$$

Equation (2.20) can now be solved using standard numerical techniques yielding all the allowed frequencies, ω, corresponding to a given wave vector, $\mathbf{k}$, where the sum in (2.18) is to

be truncated, retaining enough plane waves for the desired degree of accuracy.

Problems with the Plane Wave Expansion Method

Self consistency

To ensure a physical result, we must check to see if the finite number of plane waves used in solving the truncated sum of the magnetic field eigenvalue Equation (2.13) yields a consistent result if the same number of plane waves is used in the electric filed counter part, namely,

$$(\mathbf{k}+\mathbf{G})\times[(\mathbf{k}+\mathbf{G})\times\mathbf{E}_G] = \left(\frac{\omega}{c}\right)^2 \sum_{G\backslash} \varepsilon_{G,G\backslash}\mathbf{E}_{G\backslash}. \tag{2.21}$$

However, it was observed very early that, because of the truncated sum, such a requirement is nearly never met!

An additional source of discrepancy arises from the $\varepsilon^{-1}_{G,G\backslash}$ term in (2.13). Two distinct ways of evaluating this term have been used. First, there is the so-called *Inverse Expansion Method* in which the Fourier transform of $\varepsilon(\mathbf{r})$ is first evaluated. The result is then inverted to yield the inverted Fourier transform of the dielectric function $\varepsilon^{-1}_{G,G\backslash}$. The other is the so-called *Direct Expansion Method,* where $\varepsilon(\mathbf{r})$ is first inverted and then the Fourier transform of the inverse is performed, giving $\varepsilon^{-1}_{G,G\backslash}$ [5]. While the two choices produce the same results in the limit of an infinite plane wave basis set, for a finite plane wave expansion, they give different answers when truncated to a finite basis. For many cases, it was found that the two methods have different convergence behavior as the size of the plane wave basis is increased. For example, for the case of the Yablonovitch FCC 86% air spheres structure, the first method was found to produce eigenvalues that increase as the number of plane waves in the sum is increased, while the second method resulted in an opposite behavior [5]. In addition, it was also found that convergence speed of the second method is much slower than the first, so that for moderate basis sets, there is a big difference in the numeric results one obtains from the two methods. This, in fact, is the source of the discrepancy between the two early vector wave photonic band structure calculations, performed by Leung and Liu [2], and Zhang and Satpathy [3].

As a general rule of thumb, for a network-type of topology, the *inverse expansion* method converges much better than the *direct expansion* method. On the other hand, near the point of transition between the two classes of structures, that is, when the isolated scatterers get close to touching each other, the second method seems to perform better than the first method. For a cermet-type of topology, however, both methods suffer from serious convergence problems. Moreover, in this latter type of topology, the convergence of different bands are also quite uneven for the same structure; some bands converge more rapidly for one method, while other bands behave in just the opposite manner [5].

Convergence speed

Two factors are observed to obstruct the convergence of the PW method and hence limit its use. First, there is the scaling properties of the matrices involved in describing the system. In a *d-dimensional* structure, the size of the matrix system scales as $2N^d$, where N is the number of plane waves used in the expansion along each coordinate axis, and the factor 2 arises because of the two different possible polarization states. Combined with the finite extends and complex shapes of the building blocks of a typical crystal structure, this inevitably leads to exceedingly large matrices. To understand exactly how this affects the matrix size, we point out that from simple wave mechanics, to describe a particle localized in a finite region of space, one would need a wave packet that incorporates a large number of plane waves. Now suppose that our finite space is further complicated by having complex geometrical features incorporating different media, as is the case when constructing a photonic crystal, the number of necessary plane waves consequently grows exponentially, thereby leading to large matrix sizes.

The second limiting factor is the so-called *Gibbs Phenomenon* [6]. The discontinuous nature of $\varepsilon(\mathbf{r})$ implies that its Fourier transform will have a very long tail. Not only this, but, in general, the electric and magnetic field vectors will also be discontinuous across the discontinuities in ε, and, as a result, will have nonvanishing components for large $\mathbf{G}$ vectors. Because of this, any method that truncates a plane wave sum in either ε or $\mathbf{H}$ is guaranteed slow, if not, no convergence at all! Coupling this with the numerical problem size outlined above, the

plane wave expansion method will be very costly both in terms of computer time and memory requirements.

Developments and Improvements in the Plane Wave Expansion Method

To overcome the convergence speed problem, the MIT group [7] proposed a rather ingenious method. While working within the frame work of the Ho et al. version of the plane wave method, they suggested using the same number of plane waves per polarization (N_{PW}) in the expansion as the number of grid points on which the dielectric function is sampled (N_{FFT}). Typically, this number is very large (10^6), and, hence, more than sufficient to achieve convergence with well-defined Fourier transforms. To further tailor down the size of the problem, they pointed out that by carefully examining the operator in the eigenvalue Equation (2.9), namely

$$\boldsymbol{\theta}\mathbf{H}(\mathbf{r}) = \left(\frac{\omega}{c}\right)^2 \mathbf{H}(\mathbf{r}), \tag{2.22}$$

where $\boldsymbol{\theta} := \left[\boldsymbol{\nabla} \times \left(\frac{1}{\varepsilon(\mathbf{r})}\boldsymbol{\nabla}\times\right)\right]$, one notices that the curl operation is diagonal in k-space, while $\varepsilon(\mathbf{r})$ is diagonal in real space. This means that the vector product $\boldsymbol{\theta}\mathbf{H}(\mathbf{r})$ can be evaluated in steps using purely diagonal matrices. First, a trial wave function $\mathbf{H}$ is chosen in in k-space and its curl is computed. Then a Fast Fourier transform is performed on the result, taking it into real space where the diagonal dielectric function $\varepsilon(\mathbf{r})$ is divided. Fast Fourier transform is then performed once again, taking the result back to k-space to evaluate the final curl. Since all the matrix operations are diagonal in this scheme, the storage is only of the order N_{PW}, which is an order reduction over the usual direct expansion method. This reduces considerably the required memory size and computational time which is dominated by the Fourier transform step an order $N_{PW}log(N_{PW})$.

The rather demanding question of evaluating the eigenvalues now springs to the scene. The answer is rather simple, a variational method type of approach is used [8]. Since Equation (2.22) is to be solved using the variational method by taking a trial wave function $\mathbf{H}$, then by the same token, minimizing $\langle \mathbf{H} | \boldsymbol{\theta} | \mathbf{H} \rangle$ gives us one eigen-frequency ω. To find all the eigen-

frequencies, the procedure is repeated with the constraint that a new mode must be orthogonal to any modes that have been already found. This eventually yields all the eigen-frequencies and the field distributions for the modes.

Now that the problems relating to "*plane wave cut-off* " have been "circumvented," the main remaining source of inaccuracy is the coarseness of the mesh used to sample the dielectric function. Because of the discreteness of the real space grid used in this approach, boundaries tend to be poorly represented. This is an unavoidable problem. However, one can limit the severeness of its effects by performing some kind of smoothing or averaging along the boundaries. There are several obvious choices; one choice is to average $\varepsilon(\mathbf{r})$ over the grid cell containing the boundary and then invert the result to give $1/\overline{\varepsilon}(\mathbf{r})$. Another possibility is to reverse the order of the averaging and the inverting. However, the best results were obtained by using a tensor average which uses both previous alternatives in different directions, depending on the location of the boundary in question [7],

$$\varepsilon_{m,ij} = \overline{\varepsilon}_m n_i n_j + \left(\frac{1}{\overline{\varepsilon}}\right)_m e_{nli} e_{kjl} n_k m_k, \tag{2.23}$$

where n is the unit vector normal to the dielectric boundary and e_{ijk} is the *Levi-Civita* pseudotensor.

Advantages Versus Disadvantages of the Plane Wave Expansion Method

It is only fair to say that had it not been for this semi-analytical approach to the photonic crystal problem, no photonic crystals would have been delivered to date. The plane wave expansion technique incorporates both simplicity and viability in a rather difficult and complex problem. The result is a clear detailed mapping of the energy band diagram of almost any type of periodic dielectric arrangement. In addition, by combining this method with simple group theory analyses, it is possible to investigate large classes of crystal structures for possible photonic gap production. In fact, the A7 family of structures first studied by Ho et al. [9] is a product of this type of approach.

In spite of this, however, the PW method suffers from grave disadvantages. Among these

is the inability to efficiently study crystals containing materials with frequency dependent dielectric functions such as metals, for example. The main problem stems from the fact that the plane wave method fixes k and searches for all the possible values of ω, a process that becomes exceedingly difficult and time consuming if ϵ is frequency dependent. Furthermore, the PW method is best suited for handling perfectly periodic systems. When a crystal structure contains a defect or some kind of disorder, a supercell type of approach may be applied to model the effect on the energy band diagram. This again is very costly in terms of the number of plane waves that must be incorporated in the sum in (2.13), and, hence, the computational time. Finally, while this type of approach provides a deep physical insight into the origins of the photonic gap and the parameters affecting it, the PW method loses complete sight of possible potential applications, as it cannot provide any information about the viability of potential applications such as a cavity produced via a point defect, or the guidance capability of a wave guide produced by a line defect. Nevertheless, it certainly paints a clear picture of an invaluable portion of the overall photonic crystal portrait.

Bibliography

[1] Ohtaka, Kazuo, Tanabe, Yukito, 1996, *Journal of the Physical Society of Japan.* **65** 2265.

[2] K.M. Leung, Y. F. Liu, 1990, *Phys. Rev. Lett.* **65** 2646.

[3] Z. Zhang, S. Satpathy, 1990, *Phys. Rev. Lett.* **65** 2650.

[4] K. M. Ho, C. T. Chan, C. M. Soukoulis, 1990, *Phys. Rev. Lett.* **65** 3152.

[5] K. M. Ho, C. T. Chan, C. M. Soukoulis, in *Photonic Band Gaps and Localization*, NATO ASI Series B, Vol. **308**. Ed. C. M. Soukoulis.

[6] H. S. Sozuer, J. W. Haus, R. Inguva, 1992, *Phys. Rev. B* **45** 13962.

[7] R. D. Meade, A. M. Rappe, K. D. Brommer, J. D. Joannopoulos, O. L. Alerhand, 1993, *Phys. Rev. B* **48** 8434.

[8] P. R. Villeneuve et al. in *Photonic Band Gap Materials*, NATO ASI Series E, Vol. **315**, Ed. C. M. Soukoulis.

[9] S. Fan, P. R. Villeneuve, R. D. Meade, J. D. Joanopoulos, 1994, *Appl. Phys. Lett.* **65** 1466.

3 The Transfer Matrix Method

In this chapter, we present a detailed derivation of the Transfer Matrix Method (TMM) and the physics underlying it. We shall follow closely the development of the method as introduced first by Pendry and MacKinnon [1, 2]. We shall begin by representing Maxwell's equations on a discrete lattice of real space points. We shall then show how such discrete equations can be recast into the form of a transfer matrix which connects the electric and magnetic fields on one face of a layer of lattice points to another. Once the transfer matrix of individual layers is obtained, the overall matrix is simply evaluated by taking products of the individual layer transfer matrices. This enables us to find the fields at every point in our system and from this extract band structure or transmission and reflection information. As we pointed out earlier, this method is used primarily for calculating the transmission and reflection coefficients of photonic crystals, both periodic and with considerable disorder. Our goal is to provide the reader with the theoretical foundation of this method and to present a brief explanation of its underlaying physics. A highlight of the major strengths as well as the limitations and drawbacks of this technique will also be summarized.

The Transfer Matrix Concept

To best present the physical concept underlying the transfer matrix approach, we begin by considering the simple example of a three-layered dielectric system in which an electromagnetic radiation is incident from the left, Fig.3.1.

The equivalent transfer matrix (TM) of the medium is defined as the matrix representation of the transmission and reflection coefficients that relate the outgoing field $\left[\mathbf{E}_{out}^{+}, \mathbf{0}\right]$ to the incoming field $\left[\mathbf{E}_{in}^{+}, \mathbf{E}_{in}^{-}\right]$. Although this may sound a bit complicated, one can actually establish

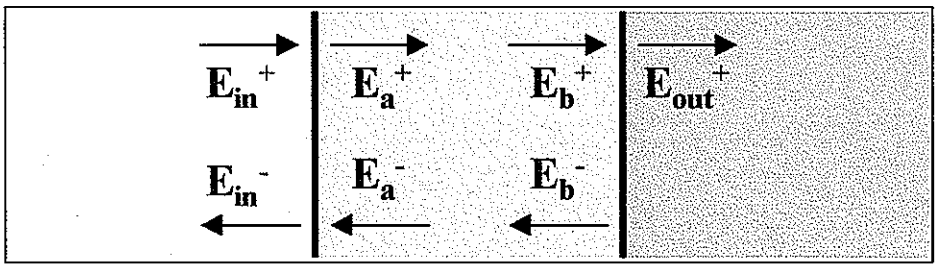

Figure 3.1 Electromagnetic radiation incident from the left on a three-layered dielectric system.

a rather simple recipe for obtaining the equivalent transfer matrix of the whole system simply by iteratively relating the fields at the various boundaries to their preceding ones. To see how this is done, we turn to Fig.3.1. Instead of writing a set of coupled vector equations at ecah boundary, rather, we cast them in the form of a matrix equation. For example, the matrix equation relating the incident and reflected fields $[\mathbf{E}_{in}^{+}, \mathbf{E}_{in}^{-}]$ at the first boundary to the fields $[\mathbf{E}_{a}^{+}, \mathbf{E}_{a}^{-}]$ immediately after the boundary is given by

$$\begin{bmatrix} \mathbf{E}_a^+ \\ \mathbf{E}_a^- \end{bmatrix} = \begin{bmatrix} a_{11} & a_{12} \\ a_{21} & a_{22} \end{bmatrix} \begin{bmatrix} \mathbf{E}_{in}^+ \\ \mathbf{E}_{in}^- \end{bmatrix}. \tag{3.1}$$

Similarly, the fields $[\mathbf{E}_{b}^{+}, \mathbf{E}_{b}^{-}]$ at the end of the first slab are related to the fields at its beginning $[\mathbf{E}_{a}^{+}, \mathbf{E}_{a}^{-}]$ by

$$\begin{bmatrix} \mathbf{E}_b^+ \\ \mathbf{E}_b^- \end{bmatrix} = \begin{bmatrix} b_{11} & b_{12} \\ b_{21} & b_{22} \end{bmatrix} \begin{bmatrix} \mathbf{E}_a^+ \\ \mathbf{E}_a^- \end{bmatrix}. \tag{3.2}$$

Finally, the transmitted field $[\mathbf{E}_{out}^{+}, \mathbf{0}]$ is also related to the field impinging on the second boundary $[\mathbf{E}_{b}^{+}, \mathbf{E}_{b}^{-}]$ according to

$$\begin{bmatrix} \mathbf{E}_{out}^+ \\ \mathbf{0} \end{bmatrix} = \begin{bmatrix} c_{11} & c_{12} \\ c_{21} & c_{22} \end{bmatrix} \begin{bmatrix} \mathbf{E}_b^+ \\ \mathbf{E}_b^- \end{bmatrix}. \tag{3.3}$$

Using this iterative approach, one can combine the previous three equations to obtain

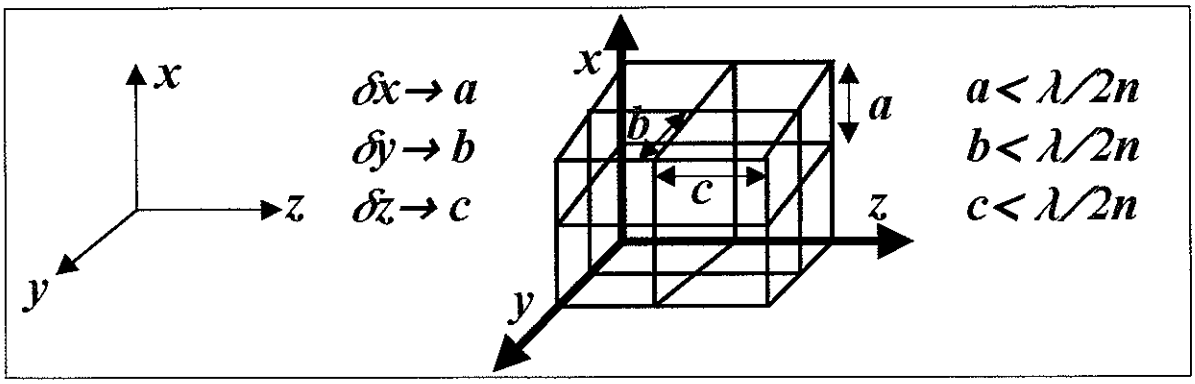

Figure 3.2 A schematic of the spatial discretization process. Here **a**, **b**, and **c** are the discretization lattice vectors, λ is the wave length of the electromagnetic radiation, and n is the effective refractive index of the medium.

$$\begin{bmatrix} \mathbf{E}^{+}_{out} \\ \mathbf{0} \end{bmatrix} = \begin{bmatrix} c_{11} & c_{12} \\ c_{21} & c_{22} \end{bmatrix} \begin{bmatrix} b_{11} & b_{12} \\ b_{21} & b_{22} \end{bmatrix} \begin{bmatrix} a_{11} & a_{12} \\ a_{21} & a_{22} \end{bmatrix} \begin{bmatrix} \mathbf{E}^{+}_{in} \\ \mathbf{E}^{-}_{in} \end{bmatrix}$$

or

$$\begin{bmatrix} \mathbf{E}^{+}_{out} \\ \mathbf{0} \end{bmatrix} = \begin{bmatrix} T \end{bmatrix} \begin{bmatrix} \mathbf{E}^{+}_{in} \\ \mathbf{E}^{-}_{in} \end{bmatrix}. \tag{3.4}$$

The combined matrix $[T]$ is the desired transfer matrix of the system and the task of finding $[T]$ reduces to evaluating the coefficients of the various constituent matrices. This may be done by implementing straight forward techniques for solving boundary value problems.

When modeling a photonic crystal, however, the approach of solving the actual boundary value problem is rather difficult, and, in most cases, quite impossible. To overcome this difficulty, first real space is converted into a grid lattice as shown by the diagram in Fig.3.2 in such a way that the unit cell of the grid lattice extends a distance less than half of the wavelength inside the medium $\frac{\lambda}{n}$, n being the effective refractive index of the medium. This restriction ensures that a standing wave fundamental mode can be captured within one unit cell of the grid lattice, a restriction that ensures the convergence of our subsequent approximations.

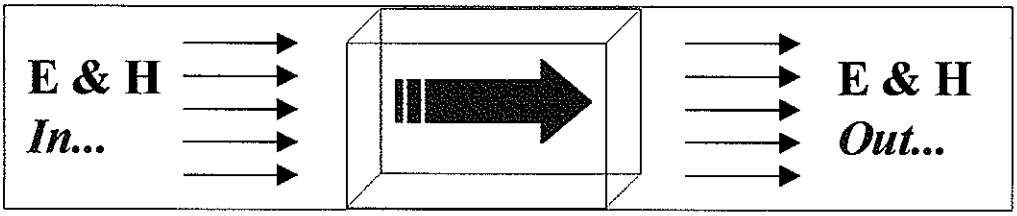

Figure 3.3 The discretized Maxwell's equations are used to propagate the fields from one face of the descretized lattice to the next.

Next, Maxwell's equations are cast into the form of a set of finite difference equations on the discrete lattice using the approximation

$$\frac{\partial \mathbf{E}}{\partial x} \longrightarrow \frac{\partial \mathbf{E}(x+\delta x) - \partial \mathbf{E}(x)}{\delta x} \approx \frac{\partial \mathbf{E}(x+a) - \partial \mathbf{E}(x)}{a}, \; etc.$$

Assuming an initial incident field, usually in the form of a plane wave, the descretized Maxwell's equations are then used to propagate the fields from one face of the descretized lattice to the next, until the fields eventually reach the end of the structure. Once the terminal fields are known, standard matrix solution techniques may be applied to relate the incident to the terminal fields, thus yielding the transfer matrix of the system. A detailed derivation of this systematic approach is given in the following section.

Obtaining the Real Space Transfer Matrix

To show how the real space transfer matrix can be derived for an actual system, we start from Maxwell's equations for a source free isotropic medium

$$\nabla \cdot \mathbf{D}(\mathbf{r},t) = 0, \tag{3.5}$$

$$\nabla \cdot \mathbf{B}(\mathbf{r},t) = 0, \tag{3.6}$$

$$\nabla \times \mathbf{E}(\mathbf{r},t) = -\frac{\partial}{\partial t}\mathbf{B}(\mathbf{r},t), \tag{3.7}$$

$$\nabla \times \mathbf{H}(\mathbf{r},t) = \frac{\partial}{\partial t}\mathbf{D}(\mathbf{r},t), \tag{3.8}$$

where $\mathbf{E}$ is the electric field, $\mathbf{H}$ is the magnetic field, $\mathbf{B}$ is the magnetic induction, and $\mathbf{D}$ is the electric displacement. Here, we will only focus our attention on the two curl equations, (3.7) and (3.8). The restrictions of orthogonality mandated by the other two divergence equations will be incorporated automatically in our treatment. Fourier transforming to k-space we obtain

$$i\mathbf{k} \times \mathbf{E} = i\omega\mathbf{B} \tag{3.9}$$

and

$$\mathbf{k} \times \mathbf{H} = -i\omega\mathbf{D}. \tag{3.10}$$

We now make the following approximations

$$\begin{aligned} \pm k_x &\approx \frac{\left[e^{(\pm ik_x a)} - 1\right]}{ia} \\ \pm k_y &\approx \frac{\left[e^{(\pm ik_y b)} - 1\right]}{ib} \\ \pm k_z &\approx \frac{\left[e^{(\pm ik_z c)} - 1\right]}{ic}. \end{aligned} \tag{3.11}$$

It is important to note that the approximations we have made in (3.11) preserve the form of the cross product in (3.7) and (3.8), which automatically insures that any *longitudinal modes* will have zero frequency, and hence guarantees transversality. Now we apply (3.11) to (3.9) and (3.10) to obtain the descretized from of Maxwell's curl equations in Fourier space, namely

$$\begin{aligned}
\frac{\left[e^{(\pm ik_y b)}-1\right]E_z}{ib}-\frac{\left[e^{(\pm ik_z c)}-1\right]E_y}{ic} &= \omega B_x \\
\frac{\left[e^{(\pm ik_z c)}-1\right]E_x}{ic}-\frac{\left[e^{(\pm ik_x a)}-1\right]E_z}{ia} &= \omega B_y \\
\frac{\left[e^{(\pm ik_x a)}-1\right]E_y}{ia}-\frac{\left[e^{(\pm ik_y b)}-1\right]E_x}{ib} &= \omega B_z
\end{aligned} \tag{3.12}$$

and

$$\begin{aligned}
-\frac{\left[e^{(\pm ik_y b)}-1\right]H_z}{ib}+\frac{\left[e^{(\pm ik_z c)}-1\right]H_y}{ic} &= -\omega D_x \\
-\frac{\left[e^{(\pm ik_z c)}-1\right]H_x}{ic}+\frac{\left[e^{(\pm ik_x a)}-1\right]H_z}{ia} &= -\omega D_y. \\
-\frac{\left[e^{(\pm ik_x a)}-1\right]H_y}{ia}+\frac{\left[e^{(\pm ik_y b)}-1\right]H_x}{ib} &= -\omega D_z
\end{aligned} \tag{3.13}$$

We now Fourier transform back to real space to obtain the corresponding descretized equations on a the real space descretized mesh

$$\begin{aligned}
\frac{E_z(\mathbf{r}+\mathbf{b})-E_z(\mathbf{r})}{ib}-\frac{E_y(\mathbf{r}+\mathbf{c})-E_y(\mathbf{r})}{ic} &= \omega B_x(\mathbf{r}) \\
\frac{E_x(\mathbf{r}+\mathbf{c})-E_x(\mathbf{r})}{ic}-\frac{E_z(\mathbf{r}+\mathbf{a})-E_z(\mathbf{r})}{ia} &= \omega B_y(\mathbf{r}) \\
\frac{E_y(\mathbf{r}+\mathbf{a})-E_y(\mathbf{r})}{ia}-\frac{E_x(\mathbf{r}+\mathbf{b})-E_x(\mathbf{r})}{ib} &= \omega B_z(\mathbf{r})
\end{aligned} \tag{3.14}$$

and

$$\begin{aligned}
-\frac{H_z(\mathbf{r}-\mathbf{b})-H_z(\mathbf{r})}{ib}+\frac{H_y(\mathbf{r}-\mathbf{c})-H_y(\mathbf{r})}{ic} &= -\omega D_x(\mathbf{r}) \\
-\frac{H_x(\mathbf{r}-\mathbf{c})-H_x(\mathbf{r})}{ic}+\frac{H_z(\mathbf{r}-\mathbf{a})-H_z(\mathbf{r})}{ia} &= -\omega D_y(\mathbf{r}). \\
-\frac{H_y(\mathbf{r}-\mathbf{a})-H_y(\mathbf{r})}{ia}+\frac{H_x(\mathbf{r}-\mathbf{b})-H_x(\mathbf{r})}{ib} &= -\omega D_z(\mathbf{r})
\end{aligned} \tag{3.15}$$

Finally, choosing the propagation direction to be along the z-direction, we proceed to eliminate the z-components of the fields and use

$$\begin{aligned} \mathbf{B}(\mathbf{r}) &= \mu_0\mu(\mathbf{r})\mathbf{H}(\mathbf{r}), \\ \mathbf{D}(\mathbf{r}) &= \varepsilon_0\varepsilon(\mathbf{r})\mathbf{E}(\mathbf{r}), \\ c_0 &= \frac{1}{\sqrt{\mu_0\varepsilon_0}}. \end{aligned} \tag{3.16}$$

This yields the real space transfer equations along the z-direction

$$\begin{aligned} E_x(\mathbf{r}+\mathbf{c}) &= E_x(\mathbf{r}) + \left(\frac{c^2\omega^2}{c_0^2}\right)\mu(\mathbf{r})\mathbf{H}_x(\mathbf{r}) \\ &+ \left(\frac{c^2}{a\varepsilon(\mathbf{r})}\right)\left[\frac{H_y(\mathbf{r}-\mathbf{a})-H_y(\mathbf{r})}{a} - \frac{H_x(\mathbf{r}-\mathbf{b})-H_x(\mathbf{r})}{b}\right] \\ &- \left(\frac{c^2}{a\varepsilon(\mathbf{r}+\mathbf{a})}\right)\left[\frac{H_y(\mathbf{r})-H_y(\mathbf{r}+\mathbf{a})}{a} - \frac{H_x(\mathbf{r}+\mathbf{a}-\mathbf{b})-H_x(\mathbf{r}+\mathbf{a})}{b}\right] \end{aligned} \tag{3.17}$$

and

$$\begin{aligned} E_y(\mathbf{r}+\mathbf{c}) &= E_y(\mathbf{r}) - \left(\frac{c^2\omega^2}{c_0^2}\right)\mu(\mathbf{r})\mathbf{H}_x(\mathbf{r}) \\ &+ \left(\frac{c^2}{b\varepsilon(\mathbf{r})}\right)\left[\frac{H_y(\mathbf{r}-\mathbf{a})-H_y(\mathbf{r})}{a} - \frac{H_x(\mathbf{r}-\mathbf{b})-H_x(\mathbf{r})}{b}\right] \\ &- \left(\frac{c^2}{b\varepsilon(\mathbf{r}+\mathbf{b})}\right)\left[-\frac{H_x(\mathbf{r})-H_x(\mathbf{r}+\mathbf{b})}{b} + \frac{H_y(\mathbf{r}-\mathbf{a}+\mathbf{b})-H_y(\mathbf{r}+\mathbf{b})}{b}\right]. \end{aligned} \tag{3.18}$$

$$
\begin{aligned}
H_x(\mathbf{r}+\mathbf{c}) &= H_x(\mathbf{r}) + \varepsilon(\mathbf{r}+\mathbf{c})\mathbf{E}_y(\mathbf{r}+\mathbf{c}) \\
&\quad + \left(\frac{c_0^2}{a\omega^2\mu(\mathbf{r}-\mathbf{a}+\mathbf{c})}\right) \cdot \\
&\quad \left[\frac{E_y(\mathbf{r}+\mathbf{c}) - E_y(\mathbf{r}-\mathbf{a}+\mathbf{c})}{a} - \frac{E_x(\mathbf{r}-\mathbf{a}+\mathbf{b}+\mathbf{c}) - E_x(\mathbf{r}-\mathbf{a}+\mathbf{c})}{b}\right] \\
&\quad - \left(\frac{c_0^2}{a\omega^2\mu(\mathbf{r}+\mathbf{c})}\right) \cdot \\
&\quad \left[\frac{E_y(\mathbf{r}+\mathbf{a}+\mathbf{c}) - E_y(\mathbf{r}+\mathbf{c})}{a} - \frac{E_x(\mathbf{r}+\mathbf{b}+\mathbf{c}) - E_x(\mathbf{r}+\mathbf{c})}{b}\right] \qquad (3.19)
\end{aligned}
$$

and

$$
\begin{aligned}
H_x(\mathbf{r}+\mathbf{c}) &= H_x(\mathbf{r}) - \varepsilon(\mathbf{r}+\mathbf{c})\mathbf{E}_y(\mathbf{r}+\mathbf{c}) \\
&\quad - \left(\frac{c_0^2}{b\omega^2\mu(\mathbf{r}+\mathbf{c})}\right) \cdot \\
&\quad \left[\frac{E_y(\mathbf{r}+\mathbf{a}-\mathbf{b}+\mathbf{c}) - E_y(\mathbf{r}-\mathbf{b}+\mathbf{c})}{a} - \frac{E_x(\mathbf{r}+\mathbf{c}) - E_x(\mathbf{r}-\mathbf{b}+\mathbf{c})}{b}\right] \\
&\quad + \left(\frac{c_0^2}{b\omega^2\mu(\mathbf{r}+\mathbf{c})}\right) \cdot \\
&\quad \left[\frac{E_y(\mathbf{r}+\mathbf{a}+\mathbf{c}) - E_y(\mathbf{r}+\mathbf{c})}{a} - \frac{E_x(\mathbf{r}+\mathbf{b}+\mathbf{c}) - E_x(\mathbf{r}+\mathbf{c})}{b}\right]. \qquad (3.20)
\end{aligned}
$$

We are now ready to extract the transfer matrix $\widehat{T}$ for propagation along the z-direction. To do so, we simply use the definition:

$$
\widehat{\mathbf{F}}(\mathbf{r}+\mathbf{c}) = \widehat{\mathbf{T}} \cdot \widehat{\mathbf{F}}(\mathbf{r}), \text{ where } \widehat{\mathbf{F}}(\mathbf{r}) = \begin{pmatrix} E_x \\ E_y \\ H_x \\ H_y \end{pmatrix} \qquad (3.21)
$$

Equation (3.21) specifies the real space transfer matrix $\widehat{T}$ and Equations (3.17) to (3.20) define its elements.

The Transfer Matrix and the Extraction of Transmission and Reflection Coefficients

As we mentioned before, the primary use of the transfer matrix is the calculation of the transmission, $\mathcal{T}$, and reflection, $\mathcal{R}$, coefficients. Indeed it is the ability of this method to estimate these experimentally measurable quantities that has made the transfer matrix technique one of the most powerful and widely used techniques in the area of photonic crystal modeling to date.

In order to extract $\mathcal{T}$ and $\mathcal{R}$ from $\widehat{T}$, it is necessary to choose a basis set in terms of which we can expand the wave-field, this will act as our fixed reference "*coordinate*" system or "*bases*". Our choice is the eigenvectors of the transfer matrix $\widehat{T}_0$ for a layer of empty cells ($\mu(\mathbf{r}) = \varepsilon(\mathbf{r}) = 1.0$). However, because $\widehat{T}_0$ is not Hermitian, we must distinguish between *left* and *right* eigenvectors;

$$\begin{aligned} \textit{Right eigenvectors} \quad &\longrightarrow \quad \widehat{T}_0 \left|r_i\right\rangle = e^{ik_i c} \left|r_i\right\rangle \\ \textit{Left eigenvectors} \quad &\longrightarrow \quad \left\langle l_i\right| \widehat{T}_0 = \left\langle l_i\right| e^{ik_i c}. \end{aligned} \tag{3.22}$$

Subject to the orthogonality condition;

$$\left\langle l_i\right| \left|r_j\right\rangle = \delta_{ij}. \tag{3.23}$$

Having defined our bases set, next we propagate the right eigenvectors through a layer of occupied cells using the full real space transfer matrix $\widehat{T}$, and expand the resulting fields in the complete set of right eigenvectors;

$$\widehat{T} \ \left|r_i\right\rangle = \widehat{\mathbf{F}} = \sum_k T_{ik} \left|r_k\right\rangle . \tag{3.24}$$

We then multiply from the left by the left eigenvectors to obtain the elements of T_{ij} of the transfer matrix;

$$\begin{aligned}\langle l_j|\widehat{T}\ |r_i\rangle &= \sum_k \langle l_j|\,T_{ik}\,|r_k\rangle \\ &= \sum_k T_{ik}\,\langle l_j|\,|r_k\rangle \\ &= T_{ik}\delta_{jk} = T_{ij}. \end{aligned} \tag{3.25}$$

Equation (3.25) specifies the elements of $\widehat{T}$ in our plane wave bases, which connect wavelets on the left side of a slab along the z-direction to those on the right side. To avoid difficulties arising from elements being randomly arranged inside $\widehat{T}$, we conveniently choose to order our bases set vectors so that the *right-going* ones come first followed by the *left-going* ones. This allows us to divide the transfer matrix into 4 sub-blocks, namely

$$\widehat{T} = \begin{pmatrix} T^{++} & T^{+-} \\ T^{-+} & T^{--} \end{pmatrix}, \tag{3.26}$$

where the $+$ sign denote right eigenvectors, whereas the $-$ sign denotes left eigenvectors. For example, T^{+-}would be the matix block relating *right-going eigenvectors* on one side of the slab to *left-going eigenvectors* on the other.

We are now at a point where we are ready to extract the desired transmission and reflection coefficients, $\mathcal{T}$ and $\mathcal{R}$, respectively. Consider the diagram in Fig.3.4 depicting the two different cases of wave incidence from the *right-hand side* and the *left-hand side* on a slab of material

If we denote the transmission and reflection matrices for a wave incident from the left by t^{++} and t^{-+} , and the transmission and reflection matrices for a wave incident from the right by t^{--} and t^{-+}, then by definition, the transfer matrix must satisfy

$$\begin{pmatrix} T^{++} & T^{+-} \\ T^{-+} & T^{--} \end{pmatrix} \begin{pmatrix} 1 \\ t^{-+} \end{pmatrix} = \begin{pmatrix} t^{++} \\ 0 \end{pmatrix} \tag{3.27}$$

and

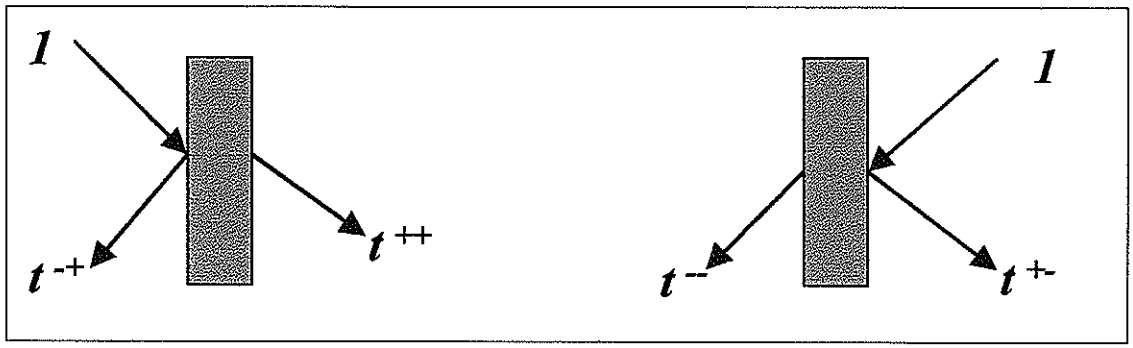

Figure 3.4 The transmission and reflection coefficients for right-propagating and left-propagating waves.

$$\begin{pmatrix} T^{++} & T^{+-} \\ T^{-+} & T^{--} \end{pmatrix} \begin{pmatrix} 0 \\ t^{--} \end{pmatrix} = \begin{pmatrix} t^{+-} \\ 1 \end{pmatrix}. \tag{3.28}$$

Combining (3.27) with (3.28) and solving for the elements of $\widehat{T}$ in terms of $t^{\pm\pm\prime}s$, we get

$$\widehat{T} = \begin{pmatrix} T^{++} & T^{+-} \\ T^{-+} & T^{--} \end{pmatrix} = \begin{pmatrix} t^{++} - t^{+-}[t^{--}]^{-1}t^{-+} & t^{+-}[t^{--}]^{-1} \\ -[t^{-+}]^{-1}t^{-+} & [t^{--}]^{-1} \end{pmatrix}. \tag{3.29}$$

Equation (3.29) allows us to obtain $t^{\pm\pm\prime}s$, once the full transfer matrix of the structure is known. The latter can easily be done by multiplying the individual transfer matrices of the individual layers compromising our structure:

$$\prod_{i=1}^{N_{layers}} \widehat{T}_i = \widehat{T}_{total}. \tag{3.30}$$

It is worth pointing out that, this latter process becomes extremely simple if the structure is periodic along the propagation direction, in which case all of the individual layer matrices become identical replicas.

The Transfer Matrix and the Band Structure

A further interesting application of this approach is to use it in determining the band structure of a periodic system. Let our photonic crystal be periodic on a lattice defined by primitive lattice vectors $\{\mathbf{a}`, \mathbf{b}`, \mathbf{c}`\}$, which are some multiple of the discretization lattice vectors $\{\mathbf{a}, \mathbf{b}`, \mathbf{c}`\}$:

$$\mathbf{a}` = \alpha\mathbf{a},\ \mathbf{b}` = \beta\mathbf{b},\ and\ \mathbf{c}` = \gamma\mathbf{c}. \tag{3.31}$$

Then, by applying Bloch's condition, we have

$$\widehat{\mathbf{F}}(\mathbf{r} + \mathbf{a}`) = e^{ik_x a`}\widehat{\mathbf{F}}(\mathbf{r}) \tag{3.32}$$

$$\widehat{\mathbf{F}}(\mathbf{r} + \mathbf{b}`) = e^{ik_y b`}\widehat{\mathbf{F}}(\mathbf{r}) \tag{3.33}$$

$$\widehat{\mathbf{F}}(\mathbf{r} + \mathbf{c}`) = e^{ik_z c`}\widehat{\mathbf{F}}(\mathbf{r})\ . \tag{3.34}$$

On the other hand, according to the definition of the transfer matrix, we can obtain the fields $\widehat{\mathbf{F}}(z + \mathbf{c}`)$ in a subsequent layer by multiplying the fields in the previous layer $\widehat{\mathbf{F}}(z)$ by the transfer matrix $\widehat{T}$ of that layer. Thus, by taking the product of n such matrices, we can find the fields in the n^{th} layer using the fields in the first. Now, since there are, say γ, layers in each unit cell along the propagation direction, then a product of γ such transfer matrices will relate the fields in one unit cell to the equivalent point in the next. If $\widehat{T}_i$ is the transfer matrix for the i^{th} layer, then

$$\widehat{\mathbf{F}}(z + \mathbf{c}`) = \prod_{i=1}^{\gamma} \widehat{T}_i.\widehat{\mathbf{F}}(z). \tag{3.35}$$

Equations (3.32) and (3.33) allow us to set the boundary conditions on the fields in the x and y directions by specifying k_x and k_y. Equations (3.34) and (3.35), on the other hand, give us

an eigenvalue problem, which allows us to determine all the possible k_z's. Thus for a given frequency ω we first calculate $\widehat{T}$. Next, from the eigenvalues of $\widehat{T}$ we extract all the k_z's which correspond to propagating waves, that is we disregard any k_z with an imaginary part. Finally the process is then repeated for different frequencies to obtain the band structure $k_z(\omega)$.

Problems with the Transfer Matrix Method: Numerical Stability

Although the transfer matrix method we have described above is founded on strong physical bases, unfortunately, it suffers from a serious numerical instability problem. The problem essentially arises from the free space transfer matrix $\widehat{T}_0$ elements that we use to define our plane wave bases set. Recall Equation (3.22),

$$\begin{aligned} \textit{Right eigenvectors} &\longrightarrow \widehat{T}_0 \left|r_i\right\rangle = e^{ik_i c} \left|r_i\right\rangle \\ \textit{Left eigenvectors} &\longrightarrow \left\langle l_i\right| \widehat{T}_0 = \left\langle l_i\right| e^{ik_i c} \end{aligned}$$

Also, recall that we are to construct the full transfer matrix from products of individual layer transfer matrices. Couple this with the fact that for every k_i there is an equivalent $-k_i$, not necessarily real, and the problem becomes quite apparent. The reason is that for each of complex k corresponding to a wave which decays exponentially, there will be a wave which grows exponentially. It is the product of such terms that threatens the numerical stability of our algorithm, and renders it practically useless, even for medium size problems.

To overcome this problem, Pendry and MacKinnon [1, 2] suggested an alternative way of combining layers. Their idea is based on the use of a multiple scattering formula for combining the transmission and reflection coefficients of the individual layers. Rather than multiplying the individual layer transfer matrices as is suggested in (3.22), we proceed by extracting the transmission and reflection matrices for the first two layers, $t_1^{\pm\pm}$ and $t_2^{\pm\pm}$, along the direction of propagation. We then employ a simple multiple scattering formula to combine these two layers together, and find the total transmission and reflection matrices for the combined layer,

involved are of dimension $N \times N$. Multiplying transfer matrices scales much more favorably, as an order N^2 operation, because of the sparseness of the transfer matrix. Usually the best course of action is to make a compromise and add together as many layers as we can by multiplying matrices and then switching to the multiple scattering technique before the numerical errors become too large.

Advantages Versus Disadvantages of the Transfer Matrix Method

This approach has several key advantages over the plane wave method introduced in chapter 2. The main advantage is that while the plane wave method fixes k and searches for all the possible values of ω, the TMM works the other way around. The TM is calculated for a specific value of ω and gives us all the possible values of k. This can be far more convenient, especially if the dielectric function is some complex function of frequency as in the case of metals. It is also vital if we wish to calculate the transmission and reflection matrices where we need to find all the waves excited at a given frequency, rather than the other way around. Moreover, it takes into account, to some extent, mode coupling difficulties, since a plane wave source is assumed to be the origin of the impinging radiation, not to mention the nature of the boundary conditions imposed on the fields. This is completely neglected in the PW method. Add to this the fact that by providing the transmission and reflection coefficients of a given structure, the TMM offers a direct way of comparison with the experimental measurements. Furthermore, by using the TMM, it is possible to estimate vital parameters for defect states at the center of all potential applications, such as the quality factor of a point defect, or the transmission band of a line defect, etc.

The major disadvantage with the TMM is that it becomes impossible to map the band structure along an arbitrary direction in k-space, something which is trivial to do using a PW technique. In addition, the TMM provides us with no information about the temporal development of the fields inside the photonic crystal, vital information when designing splitters, channel drop filters, couplers, and even simple waveguides. Moreover, the scaling properties of this technique, better than the PW method by an order N, are still of order N^2. This

imposes severe restrictions on the size of the problem that can be modeled. This, in fact, is the greatest limitation of this technique when it comes to dealing with defects or disorders, when a supercell is the only way to treat a problem in a method that imposes periodic boundary conditions like the one at hand.

Bibliography

[1] J. B. Pendry, A. MacKinnon, 1992, *Phys. Rev. Lett.* **69** 2772.

[2] J. B. Pendry, 1994, *J. Mod. Optics* **41** 209.

[3] Born and Wolf, *Principles of Optics*, Pergamon Press, pp. 66-70.

4 The Finite-Difference Time-Domain Method

In this chapter we present yet another method which has recently found its way into the photonic crystal community. Our focus in this chapter is on the so-called Finite-Difference Time-Domain (FDTD) method. As its name suggests, this method offers a way of probing the temporal as well as the spatial development of waves propagating inside a photonic crystal. However, this is not the only attractive feature about this method. Rather, it has another very appealing aspect to it. As we will show in later sections, this method scales as an order N, where N is the number of spatial discretization points. This is an order N improvement over the TMM, and N^2 over the PW methods.

Throughout this chapter, we will follow closely the development of this method as outlined in the book by A. Taflove [1]. As usual, our starting point is Maxwell's equations, where we shall begin by showing how one can discretized them fully in both space and time. We will then proceed to explain how the *space-time* descretized equations can be used to yield information about the fields inside the crystal at points throughout the process of propagation. Our goal is to provide the reader with the theoretical foundation of this method, and to present a brief explanation of its underlying physics. Finally, the major strengths as well as the limitations and drawbacks of this technique will be summarized.

Discretizing Maxwell's Equation in Space and Time: The Yee Algorithm

Motivated by the idea of developing a method that can simulate the time-evolution of the electromagnetic fields inside a given crystal, we begin by examining Maxwell's curl equations:

$$\frac{\partial \mathbf{H}}{\partial t} = -\frac{1}{\mu}\nabla \times \mathbf{E} - \frac{\rho\backslash}{\mu}\mathbf{H} \tag{4.1}$$

and

$$\frac{\partial \mathbf{E}}{\partial t} = \frac{1}{\varepsilon}\nabla \times \mathbf{H} - \frac{\sigma}{\varepsilon}\mathbf{E}, \tag{4.2}$$

where $\mathbf{E}$ and $\mathbf{H}$ are the electric and magnetic fields, respectively, ε and μ are the permittivity and permeability of the medium respectively, $\rho\backslash$ is the equivalent magnetic resistivity (included here to account for any possible magnetic losses), and σ is the electric conductivity. The next step is to introduce our discretization by replacing all spatial and temporal derivatives by finite differences according to the following prescription:

$$Space\ Point \Rightarrow (i,j,k) \equiv (i\Delta x, j\Delta y, k\Delta z), \tag{4.3a}$$

$$Function\ of\ space\ and\ time \Rightarrow f(i\Delta x, j\Delta y, k\Delta z, n\Delta t) \equiv f^n_{i,j,k}, \tag{4.3b}$$

$$Spatial\ derivative \Rightarrow \frac{\partial f(i\Delta x, j\Delta y, k\Delta z, n\Delta t)}{\partial x} \equiv \frac{f^n_{i+\frac{1}{2},j,k} - f^n_{i-\frac{1}{2},j,k}}{\Delta x} + O[(\Delta x)^2], \tag{4.3c}$$

$$Temporal\ derivative \Rightarrow \frac{\partial f(i\Delta x, j\Delta y, k\Delta z, n\Delta t)}{\partial t} \equiv \frac{f^{n+\frac{1}{2}}_{i,j,k} - f^{n-\frac{1}{2}}_{i,j,k}}{\Delta t} + O[(\Delta t)^2]. \tag{4.3d}$$

To ensure conversion, we require that the discretization steps, both spatial and temporal, be sufficiently small so that we can neglect terms containing second order in them, specifically $\Delta_{space} \leqslant \frac{\lambda}{2n}$, $\Delta_{time} \leqslant \frac{\Delta_{space}}{c\sqrt{3}}$, λ being the wavelength, n the effective refractive index, and c the speed of light. A more detailed discussion of this requirement will be addressed in a later section. For the sake of simplicity, we will only consider here one component of the two curl equations, the reader is advised to follow exactly the same argument to arrive at the final forms of the other 5 components. We will at the end of our derivation, provide the final forms of these subsequent equations. Our choice is the $x - component$ of the magnetic field curl equation, namely,

$$\frac{\partial H_x}{\partial t} = \frac{1}{\mu}\left(\frac{\partial E_y}{\partial z} - \frac{\partial E_z}{\partial y} - \rho\backslash H_x\right). \tag{4.4}$$

Employing our discretization prescription in (4.3), we get:

$$\frac{(H_x)^{n+\frac{1}{2}}_{i,j,k} - (H_x)^{n-\frac{1}{2}}_{i,j,k}}{\Delta t} = \left(\frac{1}{\mu_{i,j,k}}\right)\left[\begin{array}{c}\frac{(E_y)^n_{i,j,k+\frac{1}{2}} - (E_y)^n_{i,j,k-\frac{1}{2}}}{\Delta z} - \\ \frac{(E_z)^n_{i,j+\frac{1}{2},k} - (E_z)^n_{i,j-\frac{1}{2},k}}{\Delta x} - \rho\backslash_{i,j,k}(H_x)^n_{i,j,k}\end{array}\right] \tag{4.5}$$

Examining (4.5), one immediately realizes that the field quantities are evaluated at three different time steps: $n, n-\frac{1}{2}$, and $n+\frac{1}{2}$. This is a major problem, since our aim is to arrive at an algorithm by which we step forward in time by knowing the fields at a preceding time. In other words, we can only afford to maintain two and only two different time steps.Also, the electric field components and the magnetic field components must independently belong to two different time steps. To overcome this difficulty, we introduce the *"semi-implicit"* approximation,

$$(H_x)^n_{i,j,k} \approx \frac{(H_x)^{n+\frac{1}{2}}_{i,j,k} + (H_x)^{n-\frac{1}{2}}_{i,j,k}}{2}. \tag{4.6}$$

This is nothing other than an arithmetic average and it turns out to be more than sufficient, if Δt is chosen to be sufficiently small as previously described. Substituting (4.6) into (4.5), collecting terms, and rearranging, we obtain

$$\begin{aligned}(H_x)^{n+\frac{1}{2}}_{i,j,k} \quad = \quad & \left(\frac{1 - \frac{\rho\backslash_{i,j,k}}{2\mu_{i,j,k}}\Delta t}{1 + \frac{\rho\backslash_{i,j,k}}{2\mu_{i,j,k}}\Delta t}\right)(H_x)^{n-\frac{1}{2}}_{i,j,k} + \\ & \left(\frac{\frac{\Delta t}{\mu_{i,j,k}}}{1 + \frac{\rho\backslash_{i,j,k}}{2\mu_{i,j,k}}\Delta t}\right)\left[\begin{array}{c}\frac{(E_y)^n_{i,j,k+\frac{1}{2}} - (E_y)^n_{i,j,k-\frac{1}{2}}}{\Delta z} - \\ \frac{(E_z)^n_{i,j+\frac{1}{2},k} - (E_z)^n_{i,j-\frac{1}{2},k}}{\Delta y}\end{array}\right].\end{aligned} \tag{4.7}$$

The remaining $H - field$ components can be obtained in a straight forward manner, simply by *cyclic-permutation* of the indices x, y, and z. Thus, generally we can write

$$(H_{\widehat{i}})^{n+\frac{1}{2}}_{i,j,k} = \left(\frac{1-\frac{\rho_{i,j,k}}{2\mu_{i,j,k}}\Delta t}{1+\frac{\rho_{i,j,k}}{2\mu_{i,j,k}}\Delta t}\right)(H_{\widehat{i}})^{n-\frac{1}{2}}_{i,j,k} + \left(\frac{\frac{\Delta t}{\mu_{i,j,k}}}{1+\frac{\rho_{i,j,k}}{2\mu_{i,j,k}}\Delta t}\right)\left[\begin{array}{c}\frac{(E_{\widehat{j}})^{n}_{i,j,k+\frac{1}{2}}-(E_{\widehat{j}})^{n}_{i,j,k-\frac{1}{2}}}{\Delta_{\widehat{k}}} - \\ \frac{(E_{\widehat{k}})^{n}_{i,j+\frac{1}{2},k}-(E_{\widehat{k}})^{n}_{i,j-\frac{1}{2},k}}{\Delta_{\widehat{j}}}\end{array}\right], \tag{4.8}$$

where $\widehat{i}, \widehat{j}$,and $\widehat{k}$ now refer to x, y, and z, respectively. Following a similar argument, the $E-field$ components can be obtained from

$$(E_{\widehat{i}})^{n+1}_{i,j,k} = \left(\frac{1-\frac{\sigma_{i,j,k}}{2\varepsilon_{i,j,k}}\Delta t}{1+\frac{\sigma_{i,j,k}}{2\varepsilon_{i,j,k}}\Delta t}\right)(E_{\widehat{i}})^{n}_{i,j,k} + \left(\frac{\frac{\Delta t}{\epsilon_{i,j,k}}}{1+\frac{\sigma_{i,j,k}}{2\varepsilon_{i,j,k}}\Delta t}\right)\left[\begin{array}{c}\frac{(E_{\widehat{k}})^{n}_{i,j+\frac{1}{2},k}-(E_{\widehat{k}})^{n}_{i,j-\frac{1}{2},k}}{\Delta_{\widehat{j}}} - \\ \frac{(E_{\widehat{j}})^{n}_{i,j,k+\frac{1}{2}}-(E_{\widehat{j}})^{n}_{i,j,k-\frac{1}{2}}}{\Delta_{\widehat{k}}}\end{array}\right]. \tag{4.9}$$

Figure 4.1 shows the spatial discretization process for the field components. Notice the time offset between the $E-field$ and the $H-field$ components. This is a very important point, and, in fact, is the whole idea behind this method. Because the fields are offset by $\frac{1}{2}$ *a* $time-step$, this allows us to compute the component of one field from those of the other in a leapfrog type of process, according to the following procedure:

- *First we initialize the* $\mathbf{E}(\mathbf{H})$ *field at the time step* $t = 0 \times \Delta t$.
- *Then using these* $\mathbf{E}(\mathbf{H})$ *field values, we compute and store the* $\mathbf{H}(\mathbf{E})$ *field values at the time step* $t = \frac{1}{2} \times \Delta t$.
- *Next, use the values just computed for the* $\mathbf{H}(\mathbf{E})$ *field to calculate and store the* $\mathbf{E}(\mathbf{H})$ *field values at time step* $t = 1 \times \Delta t$.
- *Repeat...*

Figure4.2 shows this leapfrog type of calculation in one-dimension.

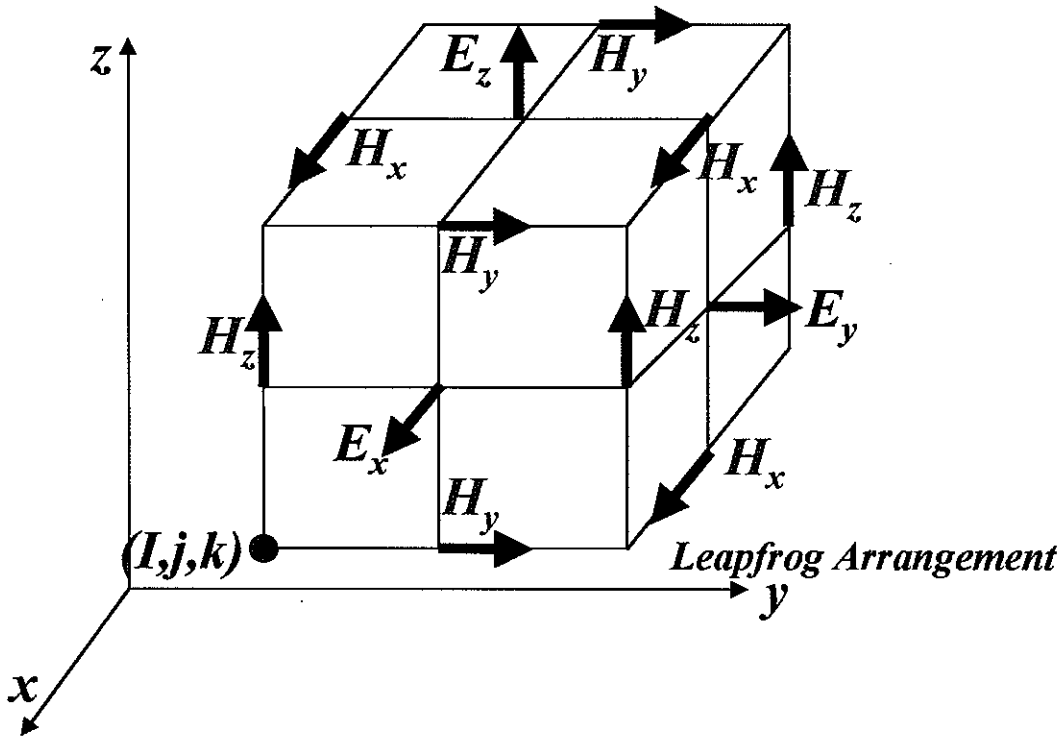

Figure 4.1 Position of the electric and magnetic field vector components about a cubic unit cell of the Yee space lattice.[2]

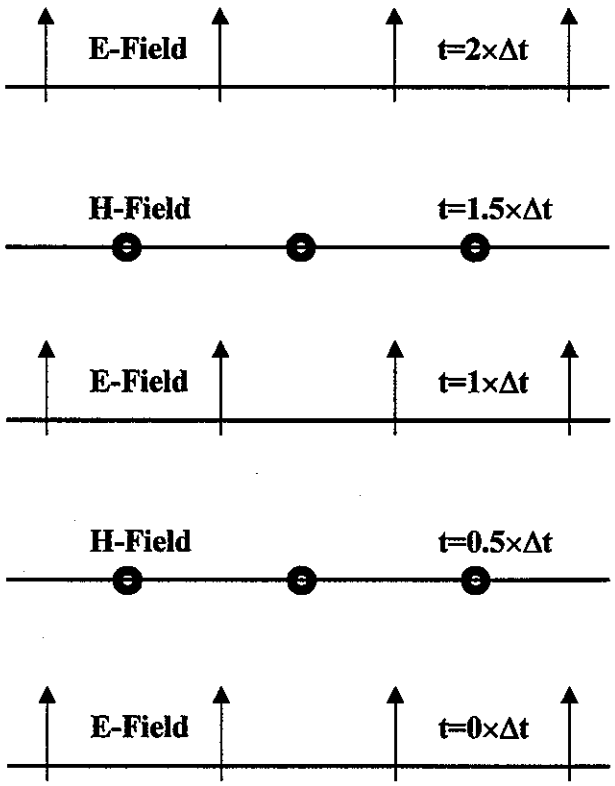

Figure 4.2 Space-time chart of the Yee algorithm for a one-dimensional example showing the use of central differences for the space derivatives and the leapfrog for the time derivatives [1].

Numerical Stability

Throughout the development of the FDTD algorithm above, we have maintained the assumption that Δ_{space} and Δ_{time} are both small enough to suffice the inclusion of only first order terms in the finte-differences (4.3c) and (4.3d). An imposing question now is: exactly how small is small enough? and what, if any, is the relation between the upper bound on Δ_{space} and Δ_{time}? To ensure a stable, accurate representation of the fields on the discretized cell, we must guarantee that the mesh size is small enough to capture the field variations throughout the structure. Typically, this can be ensured by choosing the unit cell of the grid lattice to be less than half of the wavelength inside the medium $\frac{\lambda}{n}$, n being the effective refractive index of the medium. This restriction ensures that a standing wave fundamental mode can be captured within one-unit cell of the grid lattice, a restriction that guarantees the convergence of our subsequent approximations. However, a more cautious approach, long adopted in the field, is to use a grid size that is 20 times smaller than λ, even with normal dielectric materials.

Once an upper bound is set on the spatial grid size, we turn our attention to the temporal one. Though the obvious choice is to set $\Delta_{time} = \frac{\Delta_{space}}{c}$, we shall see this severely over estimates the necessary upper bound on Δ_{time} and may very well lead to convergence problems. To find the necessary constraint on Δt, we proceed by separating the FDTD algorithm into separate time and space eigenvalue problems, and mandate the overlapping of the stability regions of the solutions of both problems according to the following procedure:

- First, the plane-wave eigenmodes are assumed to propagate in the numerical data space.
- We then determine the spectrum of eigenvalues for these modes due to the numerical space differentiation.
- Next, we compare them to the stable spectrum of eigenvalues as determined by the numerical time differentiation process.
- By requiring the complete spectrum of spatial eigenvalues to be contained within the stable range, we are assured that all possible numerical wave modes in the grid are stable, i.e., cannot grow spuriously without limit. This will bound the time step.

To simplify our task, we will assume a sourcefree, lossfree medium, ($\rho = \sigma = 0$). It can be shown, however, that the results obtained here will still hold in the more general case of lossy media and in the presence of sources [3]. We start by casting Maxwell's equations in the compact vector representation,

$$\mathbf{j}\boldsymbol{\nabla} \times (\mathbf{H} + \mathbf{j}\mathbf{E}) = \frac{\partial}{\partial t}(\mathbf{H} + \mathbf{j}\mathbf{E}), \tag{4.10}$$

where $\mathbf{j} = \sqrt{-1}$, and we have chosen to work in using a normalized system of units where $\mu = 1$, $\varepsilon = 1$, and therefore $c = 1$. Letting $\mathbf{V} = \mathbf{H} + \mathbf{j}\mathbf{E}$, then according to the convergence prescription, the stability of our FDTD algorithm can be examined by considering the pair of eigenvalue problems:

$$\frac{\partial}{\partial t}|_{nmerical}\mathbf{V} = \boldsymbol{\Lambda}\mathbf{V} \tag{4.11}$$

and

$$\mathbf{j}\boldsymbol{\nabla}|_{numerical} \times \mathbf{V} = \boldsymbol{\Lambda}\mathbf{V} \tag{4.12}$$

Using the Yee leapfrogging as the numerical time derivative, the left-hand side of (4.11) can be cast into the form

$$\frac{V_{i,j,k}^{n+\frac{1}{2}} - V_{i,j,k}^{n-\frac{1}{2}}}{\Delta t} = \Lambda V_{i,j,k}^{n}, \tag{4.13}$$

where V is a generic field vector component. We now define a solution growth factor $q_{i,j,k}$ according to

$$q_{i,j,k} = \frac{V_{i,j,k}^{n+\frac{1}{2}}}{V_{i,j,k}^{n}} = \frac{V_{i,j,k}^{n}}{V_{i,j,k}^{n-\frac{1}{2}}}. \tag{4.14}$$

According to this definition, a given spatial mode will grow at a rate of $(q_{i,j,k})^n$. To ensure a converged solution, therefore, we require that $|q_{i,j,k}| \leq 1$ for all possible spatial modes and for all possible grid points. This ensures there are no modes that will increase out of bounds as the time marching process proceeds. Substituting (4.14) in to (4.13), we get:

$$\frac{q_{i,j,k}V^n_{i,j,k} - \frac{V^n_{i,j,k}}{q_{i,j,k}}}{\Delta t} = \Lambda V^n_{i,j,k}. \tag{4.15}$$

Factoring out $V^n_{i,j,k}$, solving for $q_{i,j,k}$, and imposing the magnitude restriction on $q_{i,j,k}$, we arrive at the following requirement on the spatial eigenvalues:

$$\frac{-2}{\Delta t} \leq \mathrm{Im}(\Lambda) \leq \frac{2}{\Delta t}. \tag{4.16}$$

We now point out that at any time step n, the instantaneous values of the electric and magnetic fields distributed in space across a grid can be Fourier transformed with respect to the i, j, k grid coordinates to yield a spectrum of sinusoidal modes. The result is usually referred to as the *spatial-frequency spectrum*, or *plane wave eigenmodes* of the grid. Let the following specify an arbitrary spatial-frequency mode having $\widehat{k}_x$, $\widehat{k}_y$, and $\widehat{k}_z$ as the $x-$, $y-$, and $z-$components of its numerical wavevector:

$$\mathbf{V}_{i,j,k} = \mathbf{V}_0 e^{\mathrm{j}(\widehat{k}_x i\Delta x + \widehat{k}_y j\Delta y + \widehat{k}_z k\Delta z)}. \tag{4.17}$$

Using the Yee central space differencing to implement the derivatives of the curl operator, it can be shown that (4.12) yields

$$-2\left[\frac{\widehat{x}}{\Delta x}\sin(\widehat{k}_x\frac{\Delta x}{2}) + \frac{\widehat{y}}{\Delta y}\sin(\widehat{k}_y\frac{\Delta y}{2}) + \frac{\widehat{z}}{\Delta z}\sin(\widehat{k}_z\frac{\Delta z}{2})\right] \times \mathbf{V}_{i,j,k} = \mathbf{\Lambda}\mathbf{V}_{i,j,k}. \tag{4.18}$$

Resolving 4.18 in to components and solving for $\mathbf{\Lambda}$ we get

$$\mathbf{\Lambda}^2 = -4\left[\frac{1}{(\Delta x)^2}\sin(\widehat{k}_x\frac{\Delta x}{2}) + \frac{1}{(\Delta y)^2}\sin(\widehat{k}_y\frac{\Delta y}{2}) + \frac{1}{(\Delta z)^2}\sin(\widehat{k}_z\frac{\Delta z}{2})\right]. \tag{4.19}$$

This implies that $\mathbf{\Lambda}$ is purely imaginary and by using the upper bounds on the trigonometric Sin function, we obtain

$$-2\sqrt{\frac{1}{(\Delta x)^2}+\frac{1}{(\Delta y)^2}+\frac{1}{(\Delta z)^2}} \leq \mathrm{Im}(\mathbf{\Lambda}) \leq 2\sqrt{\frac{1}{(\Delta x)^2}+\frac{1}{(\Delta y)^2}+\frac{1}{(\Delta z)^2}}. \tag{4.20}$$

Combining Equations (4.16) and (4.20), we immediately obtain the desired upper bound on the temporal grid size or time step Δt, as

$$\Delta t \leq \frac{1}{\sqrt{\frac{1}{(\Delta x)^2}+\frac{1}{(\Delta y)^2}+\frac{1}{(\Delta z)^2}}}. \tag{4.21}$$

Or more generally, by demoralizing to a non-unity value of c, equation (4.21) becomes:

$$\Delta t \leq \frac{1}{c\sqrt{\frac{1}{(\Delta x)^2}+\frac{1}{(\Delta y)^2}+\frac{1}{(\Delta z)^2}}}. \tag{4.22}$$

Equation (4.22) defines the desired upper bound on the time step. In the special case of a cubic spatial mesh, $\Delta x = \Delta y = \Delta z = \Delta_{space}$, the requirement mandated by (4.22) reduces to: $\Delta t \leq \frac{\Delta_{space}}{c\sqrt{3}}$, precisely the restriction we imposed on Δt at the beginning of our discussion.

The Finite-Difference Time-Domain Method and the Band Structure

A further interesting application of the FDTD approach is to use it to determine the band structure of a periodic system [4]. This can be accomplished by launching an electromagnetic pulse with a limited time span, $\Delta\tau$. In Fourier space, this translates into a frequency packet with a large number of frequencies included in it, $\Delta\omega \sim 1/\Delta\tau$. If the initial fields are chosen such that they obey the Bloch condition for a particular wavevector $\mathbf{k}$, then the Fourier transform, with respect to time, will pick out the allowed frequencies corresponding to $\mathbf{k}$ as a series of delta functions. By repeating for other $\mathbf{k}$'s we get the whole band structure. If we also ensure that the initial fields obey the transverse condition, $\nabla \cdot \mathbf{B}(\mathbf{r},t) = 0$, then we pick up only the transverse solutions not the longitudinal ones. We must be careful, however, when we choose the initial fields; modes which do not have a finite overlap with the starting fields will not be found.

The total time for each $\mathbf{k}$-point is $N_r N_t$, where N_r is the number of real space points used

and N_t is the number of time steps. So, the method is really of the order N if the number of time steps we need to use is independent of the system size. For most band structure calculations, this is indeed the case.

Advantages versus Drawbacks of the Finite-Difference Time-Domain Method

The FDTD approach has several key advantages over all of the preceding methods, as well as several drawbacks. The leapfrog time stepping mechanism used is *fully explicit*, thereby completely avoids the problems associated with simultaneous equations and matrix inversions as in both of the preceding methods. The order of operations in this method scale as N_r, N_r being the number of real space discretization points. This allows the use of a very fine grid for the representation of the dielectric function. The method further imposes no restriction on the type of source used, this allows an accurate simulation of the experimental efforts, where the sources used are not plane waves, but vary from quantum-dot point sources to Gaussian beams. More importantly is the fact that by using the FDTD method, we are able to account for the finiteness of the structure in all 3−dimensions. Moreover, the method allows for the explicit examination of the time development of EM waves in the structure and therefore is the best suited algorithm for investigating wave guiding mechanisms and cavity coupling.

However, there are some rather serious drawbacks to this method. For example, to calculate the transmission and reflection coefficients, a Gaussian frequency pulse is launched into the structure. The fields values, are then stored on a slicing plane. Fast Fourier transform is then performed on these values and the component of the pointing vector perpendicular to the plane is calculated for every frequency. It is then spatially averaged and compared with the corresponding value of a reference medium to yield the transmission and reflection coefficients. This is more tedious and sensitive to errors than the TMM method.

Furthermore, the band structure calculations performed using this method are haunted by the need of extremely careful choice of the initial fields, as well as the necessity of high time resolution for the ability to distinguish between parasite pulses originating from the numerical space termination at the boundaries and the actual signal.

Moreover, to date this method has effectively never been used to model lossy and gain media; the reason stems from the infinitesimal extent of the spatial parameters describing these materials. For example, when modeling a lossy metal, one must incorporate an extremely fine spatial grid to account for the infinitesimal metallic skin-depth. This immediately magnifies the time and memory requirements of the algorithm, rendering it practically useless for such cases. There are, however, some ongoing efforts at our end to try to incorporate such material properties via virtual loss mechanisms. For example, to model the skin-depth effect, one may choose to add an absorbing component to an otherwise perfect metallic reflector or incorporate a finite conductivity. Nevertheless, this work is still in its early stages and must be subjected to several tests before credit can be claimed.

Bibliography

[1] Allen Taflove, *Computational Electrodynamics: The Finite-Difference Time-Domain Method*, 1995, Artech House Inc.

[2] K. Yee, 1966, *IEEE Trans. "Antennas and Propagation,"* Vol. **14** 302.

[3] A. Taflove, M. E. Brodwin, 1975, *IEEE Trans. Microwave Theory and Techniques*, Vol. **23**, 623.

[4] C. T. Chan, Q. L. Yu, K. M. Ho, 1995, *Phys. Rev. B* **51** 16635.

5 The Modal Expansion Method

In the past few chapters, we presented three of the most widely used techniques in photonic crystal modeling. We addressed the strengths as well as the weaknesses of each of these methods and pointed out the specific applications where each method prevailed over the others. In this chapter, we present a new theoretical approach to the problem of modeling the flow of electromagnetic radiation in photonic crystals. The Modal Expansion Method (MEM) offers a much more comprehensive study of photonic crystals as compared to the previous approaches, as well as limited weaknesses. This method was initially developed and put to extensive use for modeling one- and two-dimensional lamellar gratings [1].

In this chapter, we explain how this method can be extended successfully to model three-dimensional photonic crystals. The approcah we present here is due at large to Zhi-Yuan Li [2], and has proven to yield converged results where the previous methods have failed. Preliminary results obtained using this new approach will be presented. A highlight of the capabilities of this new approach will be pointed out, as well its limited number of drawbacks.

Principal Features of the Modal Expansion Method

To avoid redundancy by the mere introduction of yet another numerical method for modeling photonic crystals, we require that a new proposed method overcome most, if not all, of the drawbacks, as well as provide more comprehensive information over the previous three methods. To accomplish this, we begin by surveying the weaknesses to, as well as the desired strengths of these methods.

Our first requirement is to overcome the poor representation of the dielectric function at the grid boundaries arising from the spatial discretization process. This can be accomplished

by avoiding real space altogether and, like the PW method, working in k-space. Second, we need to avoid the notoriously large matrices associated with any k-space type of representation. This can be done by exploiting the crystal symmetry of the structure and, as we shall see in some cases, can amount to reducing the matrix sizes to those of a 2D problem. Third, we need to map the field distributions throughout the structure. We shall see that the method we are about to present, not only provides this, but in fact it actually provides the more crucial distribution of the eigenmodes inside the structure. Finally, we require the ability of handling complex frequency dependent dielectric functions, while at the same time maintaining high numerical stability.

Numerical Stability and the Choice of the Transfer Matrix

To provide the spatial field distribution, we will need to implement some kind of transfer matrix which contains the field information at various spatial locations throughout the structure. We encountered such a transfer matrix formalism in chapter 3, while addressing the transfer matrix method, and discovered that such matrices are highly unstable for moderately large systems. To show how one may avoid such a problem, we will begin by reiterating the formalism of such matrices, point out the reason for the instability problem, and then explain how it can be surpassed.

Consider the simple case of an electromagnetic wave incident from the right on a slab of uniform material, Fig.5.1. Using simple electromagnetic boundary value arguments, one can easily relate the fields at the two boundaries of the slab. This relation can readily be expressed in the following matrix notation.

$$\begin{pmatrix} E_2^+ \\ E_2^- \end{pmatrix} = \begin{bmatrix} t_{11} & t_{12} \\ t_{21} & t_{22} \end{bmatrix} \begin{pmatrix} E_1^+ \\ E_1^- \end{pmatrix} = \widehat{T} \begin{pmatrix} E_1^+ \\ E_1^- \end{pmatrix}. \tag{5.1}$$

Here we have chosen the simplest way to appropriate and arrange the fields based on their spatial locus relative to the slab. In this case, the resulting transfer matrix is termed the *Transmission-Matrix* or simply the *T-matrix*. This is the same type of matrix that we have

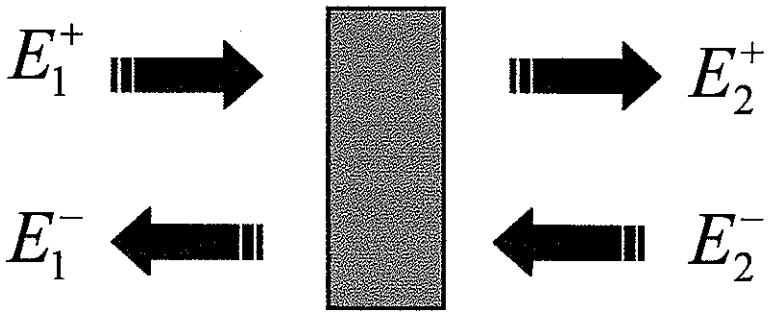

Figure 5.1 Electromagnetic waves incident on a uniform slab of material.

encountered in chapter 3, when discussing the transfer matrix method (TMM). The reason for the instability is consequently the same. For a homogeneous slab of material, the T-matrix can be diagonalized and expressed in the form:

$$\widehat{T} = \begin{bmatrix} e^{i\beta x} & 0 \\ 0 & e^{-i\beta x} \end{bmatrix}, \tag{5.2}$$

where x is the thickness of the slab, and β is the wavevector component. The instability problem becomes quite obvious when we choose to deal with materials for which the dielectric function is not purely real. In this case, β becomes complex. This immediately implies that one of the diagonal elements of the T-matrix will grow exponentially to dominate and overwhelm the other element which is decaying exponentially at the same rate, thus leading to numerical overflows and inaccuracies.

One way of avoiding this problem is by rearranging the choice of the related fields in the matrix equation. Rather than ordering the fields based on their spatial locus relative to the slab, we can choose to order them based on their propagation direction in the form

$$\begin{pmatrix} E_2^+ \\ E_1^+ \end{pmatrix} = \begin{bmatrix} r_{11} & r_{12} \\ r_{21} & r_{22} \end{bmatrix} \begin{pmatrix} E_2^- \\ E_1^- \end{pmatrix} = \widehat{R} \begin{pmatrix} E_2^- \\ E_1^- \end{pmatrix}. \tag{5.3}$$

In this type of arrangement, the resulting transfer matrix is called the *R-Matrix* and is not to be confused with the reflection matrix, since the matrix at hand does not contain immediate

reflection information.

Another way of ordering the fields is by choosing to arrange them in a scattering format, where we assume that two distinct fields aere incident on the slab from both sides at the same time, and then scattered away from it. The resulting matrix notation is given below and, for obvious reasons, the resulting transfer matrix is called the *Scattering-Matrix* or simply the *S-Matrix*:

$$\begin{pmatrix} E_2^+ \\ E_1^- \end{pmatrix} = \begin{bmatrix} s_{11} & s_{12} \\ s_{21} & s_{22} \end{bmatrix} \begin{pmatrix} E_1^+ \\ E_2^- \end{pmatrix} = \widehat{S} \begin{pmatrix} E_1^+ \\ E_2^- \end{pmatrix}. \tag{5.4}$$

To see how the above choices offer a much more stable configuration, we point out that for a homogeneous slab, the resulting diagonal formats will be such that the diagonal elements of R will be the ratio of either two exponentially growing or two exponentially decaying numbers at the same rate. On the other hand, those of S will be both exponentially decaying numbers. This means that after combining several layer-matrices, the results will not produce any numerical overflows, and hence, stability is achieved. The only drawback to the previous two choices is they do not contain any explicit physical information about the desired reflection and transmission coefficients of the slab. Rather, in order to extract such information, one would have to relate the overall structure R- or S-matrix to the T-matrix to extract this information (See chapter 3). However, this process is rather trivial.

Modal Expansion Method Pseudo Algorithm

The algorithm we present here is designed primarily for *layered-structures*, i.e., structures that can be divided into layers related to each other by crystal symmetry operations. *Notice that we can cast almost all periodic structures in a layered-structure configuration!* In other words, the algorithm can easily be extended to include all types of structures by correct use of simple group theory techniques.

We begin by reducing the size of the problem from 3D,order N^3 operations, to 2D and, hence, order N^2 operations. This can easily be done by noting that for a layered structure,

regardless of its symmetry, each distinct layer can be viewed as a 2D grating. Like the TMM, we then assume the existence of a separating fictitious infinitesimally thin (*practically of zero thickness*) layer of vacuum separating the respective structure layers.

We then follow in the foot steps of the PW method. We proceed by casting Maxwell's equations into an eigenproblem format. Next, we Fourier transform to k-space, and map the fields onto an appropriate plane wave basis. We then proceed to solve the resulting eigenvalue problem in these basis, subject to the appropriate boundary conditions *only for the first layer.*

Having solved for the fields in the fictitious vacuum layer immediately above and below the first structure layer, we then extract either the R- or the S-matrix for the first layer. This can be done by employing standard matrix manipulation routines.

The next step is to obtain the transfer R or S matrices for the subsequent layers. Here, we make use of the symmetry operations relating the consecutive layers to simplify this task. If, for example, layer 2 can be generated from layer one by a symmetry operation U_{12} , i.e.

$$Layer\ 2 = U_{12}[Layer\ 1].$$

Then, the transfer matrix of this second layer can be obtained from that of the first layer by applying a unitary transformation of the form

$$R_2 = U_{12}^{-1} R_1 U_{12},\ or\ S_2 = U_{12}^{-1} S_1 U_{12}.$$

Similarly, one can easily derive the transfer matrix of the n^{th} layer by using the appropriate symmetry operation. To avoid wasting computer memory, however we, proceed first by finding the combined transfer matrices of the first two layers, and then save them in place of R_2 or S_2, before proceeding to obtain that of the next layer. This means that at the most we need only preserve three large matrices: the transfer matrix of the first layer R_1or S_1, that of the layers combined so far R_{1n} or S_{1n}, and a work matrix used to temporarily store calculated information, R_{ij} or S_{ij}. It is worth pointing out that it may be possible to even reduce further the number of matrices to only the first two types by overwriting continuously R_{1n} or S_{1n}.

This, however, demands extreme caution, and limits the ability of the algorithm to be restarted after proceeding to calculate for a chosen period of time.

One benefit of obtaining the individual layer transfer matrices is that one can immediately obtain the field distributions at any given layer. This allows us to map the spatial progress of the fields throughout the structure.

The final step is to extract the vital physical information about the structure. The reflection and transmission coefficients can be obtained by relating our overall transfer matrix to the equivalent T-matrix of the structure, while the modal distribution profiles are simply obtained by evaluating the eigenvectors of the transfer-matrix. An even further possibility is obtaining the band structure. This can be done by diagonalizing the equivalent transfer-matrix of the structure.

The Modal Expansion Method and the ISU Metallic Layer-by-Layer Strurure

As we have seen above, the MEM offers a rich domain of information about the structure. It remains to provide the analytical base of this method. In the following few sections we give a rather detailed derivation of the necessary equations for the formalism of this new technique.

In what follows, we shall focus our attention at the special case of an ISU metallic layer-by-layer structure. In particular, we shall focus our attention on the IR-to-optical wavelength regimes. We will occupy ourselves primarily with one single layer of such a structure, keeping in mind that the subsequent layers are mere 90^0 $-$ *rotations* or $1/2$ *a period diagonal* $-$ *translations* of this first layer, see Fig.5.2. This means that once we have found the transfer matrices for this first layer, we are more or less done, as the transfer matrices of the subsequent layers are easily obtained from the one at hand by the appropriate unitary transformations as we have explained above. In the following few sections, we shall closely follow the development provided in reference [2].

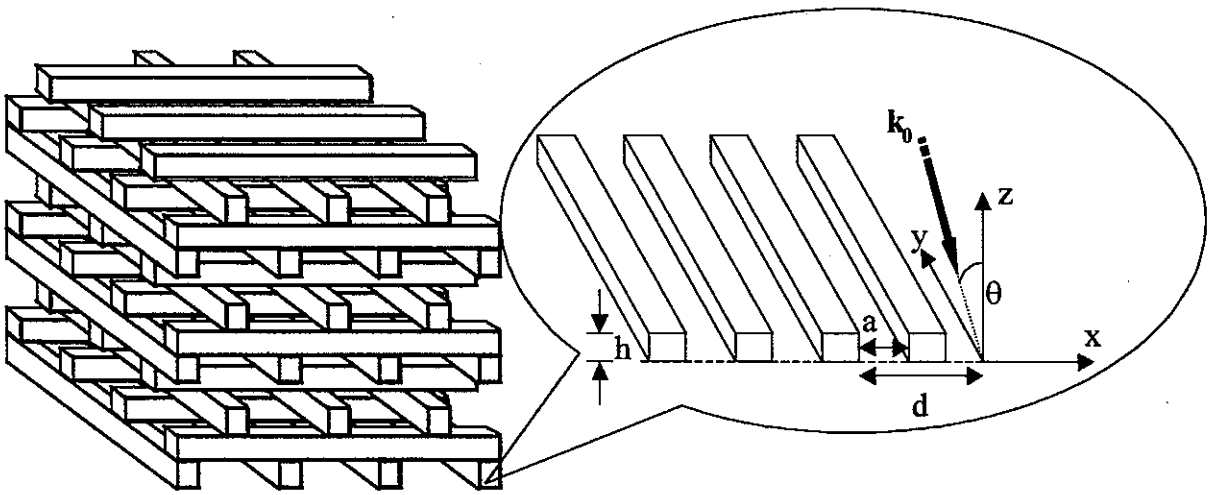

Figure 5.2 ISU layer-by-layer structure. Each layer can be viewed as a 2D grating. Each subsequent layer is a 90^0 rotation with respect to the previous one, and every two bilayers diagonally shifted a distance equal to half the period. The inset of the figure depicts the case of an electromagnetic wave incident on one such layer. θ is the polar angle of incidence, h is the rod height, a is the rod separation, and d is the grating period.

Maxwell's Equations in K-space: Eigenvalue problem approach

A careful examination of the ISU layer-by-layer structure shows that each layer constitutes a 1D-Lamellar grating. Consider the case of an electromagnetic wave incident on one such layer of the structure, where the rods are situated in the *xy-plane* and aligned parallel to the *y-axis* separated by distance a. Assume further that the grating is of high h and period d, Fig5.2. Suppose an electromagnetic wave with a wave vector $\mathbf{k} = (k_{0x}, k_{0y}, k_{0z}) = k_0(\sin\theta\cos\phi, \sin\theta\sin\phi, \cos\theta)$ is incident on the grating shown in Fig.5.2. Here, θ and ϕ are the polar and azimuthal angles, respectively. There are three regions to consider; the *reflection-region* $(z > h)$, the *grating-region* $(h \geq z \geq 0)$, and the *transmission-region* $(z < 0)$, denoted by the letters r, m, and t, respectively. Moreover, since k_x and k_y are the tangential wavevector components along the metal wall, they are conserved across this air-metal interface. To solve for the eigenmodes in each region under arbitrary incident conditions, we will use the following trial function as an eigenmode for the E-field in the air domain $0 \leq x < a$:

$$E_y(\mathbf{r}) = e^{ik_z z + ik_y y}[A_1 \sin(\beta_1 x) + B_1 \cos(\beta_1 x)], \tag{5.5a}$$

$$E_z(\mathbf{r}) = e^{ik_z z + ik_y y}[C_1 \sin(\beta_1 x) + D_1 \cos(\beta_1 x)], \tag{5.5b}$$

$$E_x(\mathbf{r}) = e^{ik_z z + ik_y y}[-(ik_y B_1 + ik_z D_1)\beta 1_1^{-1} \sin(\beta_1 x) + (ik_y A_1 + ik_z B_1)\beta 1_1^{-1} \cos(\beta_1 x)]. \tag{5.5c}$$

Here, $k_z^2 + \beta_1^2 + k_y^2 = \epsilon_1 k_0^2$, with $Im(\beta_1) > 0$ to account for the finite conductivity of the metal. The E-field in the metal domain $a \leq x < d$ is assumed to have the form

$$E_y(\mathbf{r}) = e^{ik_z z + ik_y y}[A_2 e^{i\beta_2(x-a)} + B_2 e^{-i\beta_2(x-d)}], \tag{5.6a}$$

$$E_z(\mathbf{r}) = e^{ik_z z + ik_y y} C_2 e^{i\beta_2(x-a)} + D_2 e^{-i\beta_2(x-d)}], \tag{5.6b}$$

$$E_x(\mathbf{r}) = e^{ik_z z + ik_y y}[-(k_y A_2 + k_z C_2)\beta_2^{-1} e^{i\beta_2(x-a)} + (k_y B_2 + k_z D_2)\beta_2^{-1} e^{-i\beta_2(x-d)}], \tag{5.6c}$$

where $k_z^2 + \beta_2^2 + k_y^2 = \epsilon_2 k_0^2$ and $Im(\beta_2) > 0$.

Next, we determine the amplitudes in the trial solution by using boundary conditions at metal walls located at $x = a$ and $x = d$. Since E_y, E_z, H_y and H_z are all continuous across the metal walls, from the E-field continuity we get:

$$A_1 \sin\beta_1 a + B_1 \cos\beta_1 a = A_2, \tag{5.7a}$$

$$C_1 \sin\beta_1 a + D_1 \cos\beta_1 a = C_2, \tag{5.7b}$$

and

$$p_0 B_1 = B_2, \tag{5.8a}$$

$$p_0 D_1 = D_2, \tag{5.8b}$$

where $p_0 = e^{ik_x d}$ is the Bloch's phase factor. In deriving Equations (5.8a) and (5.8b), we have used Bloch's theorem to relate fields at $x = 0$ and $x = d$. The continuity of the H-field, on the

other hand, yields

$$-[k_y k_z \beta_1^{-1} \cos\beta_1 a]A_1 + [k_y k_z \beta_1^{-1} \sin\beta_1 a]B_1 - [(k_z^2\beta_1^{-1} + \beta_1)\cos\beta_1 a]C_1 + [(k_z^2\beta_1^{-1} + \beta_1)\sin\beta_1 a]D_1$$
$$= -(ik_y k_z \beta_2^{-1})A_2 - (k_z^2\beta_2^{-1} + \beta_2)C_2, \tag{5.9a}$$

$$[k_y k_z \beta_1^{-1} \cos\beta_1 a]C_1 - [k_y k_z \beta_1^{-1} \sin\beta_1 a]D_1 + [(k_y^2\beta_1^{-1} + \beta_1)\cos\beta_1 a]A_1 - [(k_y^2\beta_1^{-1} + \beta_1)\sin\beta_1 a]B_1$$
$$= (ik_y k_z \beta_2^{-1})B_2 + (k_y^2\beta_2^{-1} + \beta_2)D_2. \tag{5.9b}$$

$$p_0[-(k_y k_z \beta_1^{-1})A_1 - (k_z^2\beta_1^{-1} + \beta_1)C_1] = (ik_y k_z \beta_2^{-1})B_2 + (k_z^2\beta_2^{-1} + \beta_2)D_2, \tag{5.10a}$$

$$p_0[(k_y k_z \beta_1^{-1})C_1 - (k_y^2\beta_1^{-1} + \beta_1)A_1] = -(ik_y k_z \beta_2^{-1})D_2 - (k_y^2\beta_2^{-1} + \beta_2)B_2. \tag{5.10b}$$

In deriving Equations (5.10a) and (5.10b), we have neglected terms with a factor $e^{i\beta_2(d-a)}$, which is far smaller than one due to small skin depth of metal in mid-infrared-to-optical wavelength regimes. Define

$$T_1 = \begin{pmatrix} -k_y k_z \beta_1^{-1} & -(k_z^2\beta_1^{-1} + \beta_1) \\ k_y^2\beta_1^{-1} + \beta_1 & k_y k_z \beta_1^{-1} \end{pmatrix}, \tag{5.11a}$$

$$T_2 = \begin{pmatrix} ik_y k_z \beta_2^{-1} & -i(k_z^2\beta_2^{-1} + \beta_2) \\ i(k_y^2\beta_2^{-1} + \beta_2) & ik_y k_z \beta_2^{-1} \end{pmatrix}. \tag{5.11b}$$

Combining (5.9) with (5.11) we obtain

$$\begin{pmatrix} A_2 \\ C_2 \end{pmatrix} = T_2^{-1}T_1 \begin{pmatrix} A_1 \\ C_1 \end{pmatrix} \cos\beta_1 a - T_2^{-1}T_1 \begin{pmatrix} B_1 \\ D_1 \end{pmatrix} \sin\beta_1 a = \begin{pmatrix} A_1 \\ C_1 \end{pmatrix} \sin\beta_1 a + \begin{pmatrix} B_1 \\ D_1 \end{pmatrix} \cos\beta_1 a. \tag{5.12}$$

From (5.8) and (5.11) we get

$$\begin{pmatrix} B_1 \\ D_1 \end{pmatrix} = -T_2^{-1}T_1 \begin{pmatrix} A_1 \\ C_1 \end{pmatrix}. \tag{5.13}$$

Denoting $T = T_2^{-1}T_1$ and deleting B_1 and D_1 from (5.12) and (5.13), we finally have

$$(I - T^2)\begin{pmatrix} A_1 \\ C_1 \end{pmatrix} \tan\beta_1 a = 2T \begin{pmatrix} A_1 \\ C_1 \end{pmatrix}$$

or

$$\tan\beta_1 a \begin{pmatrix} A_1 \\ C_1 \end{pmatrix} = 2(I - T^2)^{-1}T \begin{pmatrix} A_1 \\ C_1 \end{pmatrix}. \tag{5.14}$$

Equation (5.14) is recognized to be a standard eigen-equation for the matrix $Q = 2(I-T^2)^{-1}T$, with $\tan\beta_1 a$ being the eigenvalue. It will be shown that this eigen-equation can be analytically solved. Notice Q and T have the same eigenvector, it therefore suffices to work on T, whose explicit form is

$$T = T_2^{-1}T_1 = \frac{-i}{\epsilon_2 k_0^2}\begin{pmatrix} k_z^2\beta_2^{-1}\beta_1 + k_y^2\beta_2\beta_1^{-1} + \beta_1\beta_2 & k_y k_z\beta_1^{-1}\beta_2 - \beta_2^{-1}\beta_1 \\ k_y k_z\beta_1^{-1}\beta_2 - \beta_2^{-1}\beta_1 & k_y^2\beta_2^{-1}\beta_1 + k_z^2\beta_2\beta_1^{-1} + \beta_1\beta_2 \end{pmatrix}. \tag{5.15}$$

After some algebraic manipulations, we find that the eigen-equation,

$$T\begin{pmatrix} A_1 \\ C_1 \end{pmatrix} = x\begin{pmatrix} A_1 \\ C_1 \end{pmatrix},$$

has eigenvalues of $x = -i\epsilon_1\beta_2/\epsilon_2\beta_1$ and $x = -i\beta_1/\beta_2$, corresponding to eigenvectors $(A_1, C_1) = (1, -k_y/k_z)$ and $(A_1, C_1) = (k_y/k_z, 1)$, respectively. From this, the eigenvalues of Equation (5.14) are directly calculated as

$$\tan\beta_1 a = \frac{-2i\beta_1\beta_2}{\beta_1^2 + \beta_2^2} \tag{5.16}$$

and

$$\tan \beta_1 a = \frac{-2i\epsilon_1\epsilon_2\beta_1\beta_2}{\epsilon_2^2\beta_1^2 + \epsilon_1^2\beta_2^2}. \tag{5.17}$$

The corresponding eigenvectors are $(A_1^1, C_1^1) = (1, -k_y/k_z)$ and $(A_1^2, C_1^2) = (k_y/k_z, 1)$, respectively.

We have designated these two modes as mode 1 and mode 2. Equations (5.16) and (5.17) are both transcendental equations, whose solutions must be numerically calculated on the complex plane. To avoid this difficulty, we start from solutions for a *perfect-conducting* metal wall (keep in mind that with a large value of ϵ_2 in mid-infrared regime, the eigenmodes should not be far from those for a perfect conducting structure), and use iteration techniques to find the accurate solutions of β_1 in Equations (5.16) and (5.17). For higher modes $m \geq 1$, we set the initial value of β_1 to be $\beta_1^0 = m\pi/a$, then the following iteration procedure is followed.

$$\tan \beta_1^{n+1} a = \frac{-2i\beta_1^n\beta_2^n}{\beta_1^{2n} + \beta_2^{2n}} \tag{5.18}$$

and

$$\tan \beta_1^{n+1} a = \frac{-2i\epsilon_1\epsilon_2\beta_1^n\beta_2^n}{\epsilon_2^2(\beta_1^n)^2 + \epsilon_1^2(\beta_2^n)^2}, \tag{5.19}$$

where $n = 0, 1, 2, \cdots$, and $(\beta_2^n)^2 = (\epsilon_2 - \epsilon_1)k_0^2 + (\beta_1^n)^2$. In practice, several iteration loops are enough to guarantee an accurate solution of β_1.

The iteration technique cannot be applied to the lowest mode by starting from $\beta_1^0 = 0$. It is easy to find that $\beta_1 = 0$ is a solution of both (5.16) and (5.17). However, it can be shown that this solution is un-physical, unless ϵ_2 is infinite.

Now we can write down the EM fields inside the grating region using eigenmode expansion.

The tangential field components are

$$\begin{aligned} E_x(\mathbf{r}) &= \sum_m [A_m e^{ik^+_{z,m1}z} X^+_{m1}(x) + B_m e^{ik^-_{z,m1}z} X^-_{m1}(x) + \\ &\quad C_m e^{ik^+_{z,m2}z} X^+_{m2}(x) + D_m e^{ik^-_{z,m2}z} X^-_{m2}(x)] e^{ik_y y} \qquad (5.20a) \\ E_y(\mathbf{r}) &= \sum_m [A_m e^{ik^+_{z,m1}z} Y^+_{m1}(x) + B_m e^{ik^-_{z,m1}z} Y^-_{m1}(x) + \\ &\quad C_m e^{ik^+_{z,m2}z} Y^+_{m2}(x) + D_m e^{ik^-_{z,m2}z} Y^-_{m2}(x)] e^{ik_y y} \qquad (5.20b) \end{aligned}$$

and

$$\begin{aligned} H_x(\mathbf{r}) &= \sum_m [A_m e^{ik^+_{z,m1}z} U^+_{m1}(x) + B_m e^{ik^-_{z,m1}z} U^-_{m1}(x) + \\ &\quad C_m e^{ik^+_{z,m2}z} U^+_{m2}(x) + D_m e^{ik^-_{z,m2}z} U^-_{m2}(x)] e^{ik_y y} \qquad (5.21a) \\ H_y(\mathbf{r}) &= \sum_m [A_m e^{ik^+_{z,m1}z} V^+_{m1}(x) + B_m e^{ik^-_{z,m1}z} V^-_{m1}(x) + \\ &\quad C_m e^{ik^+_{z,m2}z} V^+_{m2}(x) + D_m e^{ik^-_{z,m2}z} V^-_{m2}(x)] e^{ik_y y}. \qquad (5.21b) \end{aligned}$$

Here $X^+_{m1}(x)$ is the modal function of the E-field x-component connected with mode 1 under the upwards k_z wave vector $k^+_{z,m1}$, others are similarly defined. A_m, B_m, C_m, and D_m are modal coefficients. For the lowest mode $m = 0$, since only mode 2 is present, A_m and B_m vanish.

To determine the amplitude of modal functions, we use the boundary conditions at the two interfaces of $z = h$ and $z = 0$. We also use the method of moments and project the E-field

onto the plane waves and obtain

$$\begin{aligned} dE_{xi}(h) &= C_0 e^{ik^+_{z,02}h} I^3_{i,0} + D_0 e^{ik^-_{z,02}h} I^4_{i,0} + \\ &\sum_{m\geq 1} [A_m e^{ik^+_{z,m1}h} I^1_{i,m} + B_m e^{ik^-_{z,m1}h} I^2_{i,m} + C_m e^{ik^+_{z,m2}h} I^3_{i,m} \\ &+ D_m e^{ik^-_{z,m2}h} I^4_{i,m}] \end{aligned} \tag{5.22a}$$

$$\begin{aligned} dE_{yi}(h) &= C_0 e^{ik^+_{z,02}h} J^3_{i,0} + D_0 e^{ik^-_{z,02}h} J^4_{i,0} + \\ &\sum_{m\geq 1} [A_m e^{ik^+_{z,m1}h} J^1_{i,m} + B_m e^{ik^-_{z,m1}h} J^2_{i,m} + C_m e^{ik^+_{z,m2}h} J^3_{i,m} \\ &+ D_m e^{ik^-_{z,m2}h} J^4_{i,m}] \end{aligned} \tag{5.22b}$$

and

$$dE_{xi}(0) = C_0 I^3_{i,0} + D_0 I^4_{i,0} + \sum_{m\geq 1} [A_m I^1_{i,m} + B_m I^2_{i,m} + C_m I^3_{i,m} + D_m I^4_{i,m}] \tag{5.23a}$$

$$dE_{xi}(0) = C_0 J^3_{i,0} + D_0 J^4_{i,0} + \sum_{m\geq 1} [A_m J^1_{i,m} + B_m J^2_{i,m} + C_m J^3_{i,m} + D_m J^4_{i,m}]. \tag{5.23b}$$

Here the moment between a plane wave function and a modal function is defined as

$$I^1_{i,m} = \int_0^d e^{-ik_{xi}x} X^+_{m1}(x)dx, \quad I^2_{i,m} = \int_0^d e^{-ik_{xi}x} X^-_{m1}(x)dx,$$

$$I^3_{i,m} = \int_0^d e^{-ik_{xi}x} X^+_{m2}(x)dx, \quad I^4_{i,m} = \int_0^d e^{-ik_{xi}x} X^-_{m2}(x)dx.$$

$J^k_{i,m}$, $M^k_{i,m}$, and $N^k_{i,m}$ $(k = 1, 2, 3, 4)$ are obtained by replacing $X(x)$ by $Y(x)$, $U(x)$, and $V(x)$ in the integration. The boundary condition of the H-field is done by projecting the H_x field onto the modal functions of mode 1, while projecting the H_y field onto the modal functions of mode 2. This results in

$$\sum_i H_{xi}(h)M_{-i,m} = C_0 e^{ik^+_{z,02}h} S^3_{m,0} + D_0 e^{ik^-_{z,02}h} S^4_{mi,0} + \\ + \sum_{m'\geq 1} [A_m e^{ik^+_{z,m'_1}h} S^1_{m,m'} + B_m e^{ik^-_{z,m'_1}h} S^2_{m,m'} + C_m e^{ik^+_{z,m2}h} S^3_{m,m'} \\ + D_m e^{ik^-_{z,m2}h} S^4_{m,m'}] \tag{5.24a}$$

$$\sum_i H_{yi}(h)N_{-i,m} = C_0 e^{ik^+_{z,02}h} T^3_{m,0} + D_0 e^{ik^-_{z,02}h} T^4_{m,0} + \\ \sum_{m'\geq 1} [A_m e^{ik^+_{z,m'_1}h} T^1_{m,m'} + B_m e^{ik^-_{z,m'_1}h} T^2_{m,m'} + C_m e^{ik^+_{z,m2}h} T^3_{m,m'} \\ + D_m e^{ik^-_{z,m2}h} T^4_{m,m'}] \tag{5.24b}$$

and

$$\sum_i H_{xi}(0)M_{-i,m} = C_0 S^3_{m,0} + D_0 S^4_{mi,0} + \\ \sum_{m'\geq 1} [A_m S^1_{m,m'} + B_m S^2_{m,m'} + C_m S^3_{m,m'} + D_m S^4_{m,m'}] \tag{5.25a}$$

$$\sum_i H_{yi}(0)N_{-i,m} = C_0 T^3_{m,0} + D_0 T^4_{m,0} + \\ \sum_{m'\geq 1} [A_m T^1_{m,m'} + B_m T^2_{m,m'} + C_m T^3_{m,m'} + D_m T^4_{m,m'}], \tag{5.25b}$$

where, $m = 1, 2, \cdots$ and the moment between two modal functions is defined as

$$S^1_{m,m'} = \int_0^d U^+_{m1}(x)U^+_{m'1}(x)dx, \qquad S^2_{m,m'} = \int_0^d U^+_{m1}(x)U^-_{m'1}(x)dx, \tag{5.26a}$$

$$S^3_{m,m'} = \int_0^d U^+_{m1}(x)U^+_{m'2}(x)dx, \qquad S^4_{m,m'} = \int_0^d U^+_{m1}(x)U^-_{m'2}(x)dx. \tag{5.26b}$$

and

$$T^1_{m,m'} = \int_0^d U^+_{m2}(x)U^+_{m'1}(x)dx, \qquad T^2_{m,m'} = \int_0^d U^+_{m2}(x)U^-_{m'1}(x)dx, \tag{5.27a}$$

$$T^3_{m,m'} = \int_0^d U^+_{m2}(x)U^+_{m'2}(x)dx, \qquad T^4_{m,m'} = \int_0^d U^+_{m2}(x)U^-_{m'2}(x)dx. \tag{5.27b}$$

From equations (5.24) and (5.25) we can delete the modal amplitude unknown variables and obtain the following matrix equation that connects the E-field and H-field on both sides of the grating as

$$\begin{pmatrix} E_{xi}(h) \\ E_{yi}(h) \\ E_{xi}(0) \\ E_{yi}(0) \end{pmatrix} = \begin{bmatrix} P_{11} & P_{12} & P_{13} & P_{14} \\ P_{21} & P_{22} & P_{23} & P_{24} \\ P_{31} & P_{32} & P_{33} & P_{34} \\ P_{41} & P_{42} & P_{43} & P_{44} \end{bmatrix} \begin{pmatrix} H_{xi}(h) \\ H_{yi}(h) \\ H_{xi}(0) \\ H_{yi}(0) \end{pmatrix}. \tag{5.28}$$

Once the transfer matrix of the structure is defined, our next task is to determine how to combine such matrices to obtain the overall matrix of a grating with an arbitrarily large thickness in a numerically stable manner. In the next sections we shall focus primarily on deriving the necessary recursion relations for combining the $R-$ and $S-$transfer matrices for an arbitrary number of structural layers, followed by a simple prescription for extracting the transmission and reflection spectra from them.

Recursion relations for the R-transfer Matrix

We start by considering the case of an R-type of transfer matrix. When we deal with gratings consisting of many layers, we can assume that each layer is surrounded by two imaginary infinitely-thin air films on both of its sides. The introduction of these extra air thin films has no physical contamination to the scattering problem, because the thickness of all films is set to zero. But these imaginary air films enable us to treat each grating layer separately in a systematical manner. All that is left is to combine these single layers into a whole. The bonus of great convenience is a natural result from such a technique. To appreciate the numerical

stability for arbitrarily thick gratings, we should use the R-matrix technique to calculate the overall R-matrix connecting the plane waves in the incidence and transmission regions. The key point of this technique is as follows. Suppose we have obtained the overall R-matrix for the first n layers $R^{(n)} = (R_{11}^{(n)}, R_{12}^{(n)}, R_{21}^{(n)}, R_{22}^{(n)})$, which satisfies

$$\begin{pmatrix} \Omega_0^+ \\ \Omega_n^+ \end{pmatrix} = \begin{bmatrix} R_{11}^{(n)} & R_{12}^{(n)} \\ R_{21}^{(n)} & R_{22}^{(n)} \end{bmatrix} \begin{pmatrix} \Omega_0^- \\ \Omega_n^- \end{pmatrix} \tag{5.29}$$

and the R-matrix $r^{(n+1)}$ for the $(n+1)^{th}$ layer which satisfies

$$\begin{pmatrix} \Omega_n^+ \\ \Omega_{n+1}^+ \end{pmatrix} = \begin{bmatrix} r_{11}^{(n+1)} & r_{12}^{(n+1)} \\ r_{21}^{(n+1)} & r_{22}^{(n+1)} \end{bmatrix} \begin{pmatrix} \Omega_n^- \\ \Omega_{n+1}^- \end{pmatrix}, \tag{5.30}$$

where $\Omega_0^+(\Omega_0^-)$ and $\Omega_n^+(\Omega_n^-)$ are column vectors for waves in the upper side of the 1^{st} and $(n+1)^{th}$ layer of the gratings, while $\Omega_1^+(\Omega_1^-)$ and $\Omega_{n+1}^+(\Omega_{n+1}^-)$ are column vectors for waves in the lower side. We can prove straightforward that the overall R-matrix $R^{(n+1)}$ for the total $n+1$ layers is given by

$$R_{11}^{(n+1)} = R_{11}^{(n)} + R_{12}^{(n)}[r_{11}^{(n+1)} - R_{22}^{(n)}]^{-1} R_{21}^{(n)}, \tag{5.31a}$$

$$R_{12}^{(n+1)} = -R_{12}^{(n)}[r_{11}^{(n+1)} - R_{22}^{(n)}]^{-1} r_{12}^{(n+1)}, \tag{5.31b}$$

$$R_{21}^{(n+1)} = r_{21}^{(n+1)}[r_{11}^{(n+1)} - R_{22}^{(n)}]^{-1} R_{21}^{(n)}, \tag{5.31c}$$

$$R_{22}^{(n+1)} = r_{22}^{(n+1)} - r_{21}^{(n+1)}[r_{11}^{(n+1)} - R_{22}^{(n)}]^{-1} r_{12}^{(n+1)}. \tag{5.31d}$$

Therefore, the procedure to calculate the overall R-matrix for a grating is as follows. First, calculate the R-matrix for the first layer $r^{(1)}$ and set $R^{(1)} = r^{(1)}$. Then, calculate the R-matrix for the second layer $r^{(2)}$, and use equation (5.31) to calculate the overall R-matrix $R^{(2)}$ for the first two layers, repeating until the final layer of the gratings.

Obtaining the transmission and reflection spectra form the R-matrix

With the final overall R-matrix in hand, we can solve the reflection and transmission coefficients by

$$\begin{pmatrix} E_0 + E_r \\ E_t \end{pmatrix} = \begin{bmatrix} R_{11}^{(n+1)} & R_{12}^{(n+1)} \\ R_{21}^{(n+1)} & R_{22}^{(n+1)} \end{bmatrix} \begin{pmatrix} E_0 - E_r \\ E_t \end{pmatrix} \tag{5.32}$$

or finally

$$\begin{bmatrix} I + R_{11}^{(n+1)} & -R_{12}^{(n+1)} \\ R_{21}^{(n+1)} & I - R_{22}^{(n+1)} \end{bmatrix} \begin{pmatrix} E_r \\ E_t \end{pmatrix} = \begin{pmatrix} R_{11}^{(n+1)} E_0 \\ R_{21}^{(n+1)} E_0 \end{pmatrix}. \tag{5.33}$$

Here I is an unit matrix, and

$$E_0 = (E_0^{-\frac{N}{2}}, \cdots, E_0^0, \cdots, E_0^j, \cdots E_0^{\frac{N}{2}})^T, \tag{5.34a}$$

$$E_r = (E_r^{-\frac{N}{2}}, \cdots, E_r^0, \cdots, E_r^j, \cdots E_r^{\frac{N}{2}})^T, \tag{5.34b}$$

$$E_t = (E_t^{-\frac{N}{2}}, \cdots, E_t^0, \cdots, E_t^j, \cdots E_t^{\frac{N}{2}})^T. \tag{5.34c}$$

Obviously, we have selected an index sequence of (j, i) to designate the plane wave components $(k_{ij,x}, k_{ij,y})$. All numerical manipulations take this sequence as the universal basis.

Until now we have only derived the R-matrix for the first layer of the ISU layer-by-layer PBG gratings, parallel to the y-axis. We can follow the same procedure as that for the first layer to calculate the R-matrix for the second layer, and the other layers. However, the symmetry of the PBG gratings reminds us to adopt an easier way to obtain the R-matrix for other layers. We see that the second layer, with rods directed along the x-axis, is just a 90° rotation from the first layer. The third layer is translated by $d/2$ from the first layer along the x-axis, and the fourth layer is translated from the second layer by $d/2$ along the y-axis. In another words, the third and fourth layers as a whole are translated from the first and second layers by $(d/2, d/2)$. Therefore, under a straightforward transformation of coordinates, we can derive the R-matrix for any layer in a simple way.

First consider the 90° rotation transformation. The coordinates are transformed as

$$y \longrightarrow x', \qquad x \longrightarrow -y', \tag{5.35}$$

where x, y and x', y' are coordinates in the lab (original) and crystal (rotated) frames. This also means that both the wavevectors and EM fieldvectors should be transformed in the same way,

$$(k_x, k_y) \longrightarrow (-k'_y, k'_x), \qquad (E_x, E_y) \longrightarrow (-E'_y, E'_x). \tag{5.36}$$

Suppose r' and r is the R-matrix in the rotated and original coordinates, respectively, which satisfy

$$\begin{pmatrix} \Omega'^{+}_{0x}(k'_{i,j}) \\ \Omega'^{+}_{0y}(k'_{i,j}) \\ \Omega'^{+}_{1x}(k'_{i,j}) \\ \Omega'^{+}_{1y}(k'_{i,j}) \end{pmatrix} = \begin{bmatrix} r'^{(11)}_{11} & r'^{(12)}_{11} & r'^{(11)}_{12} & r'^{(12)}_{12} \\ r'^{(21)}_{11} & r'^{(22)}_{11} & r'^{(21)}_{12} & r'^{(22)}_{12} \\ r'^{(11)}_{21} & r'^{(12)}_{21} & r'^{(11)}_{22} & r'^{(12)}_{22} \\ r'^{(21)}_{21} & r'^{(22)}_{21} & r'^{(21)}_{22} & r'^{(22)}_{22} \end{bmatrix} \begin{pmatrix} \Omega'^{-}_{0x}(k'_{m,n}) \\ \Omega'^{-}_{0y}(k'_{m,n}) \\ \Omega'^{-}_{1x}(k'_{m,n}) \\ \Omega'^{-}_{1y}(k'_{m,n}) \end{pmatrix} \tag{5.37}$$

and

$$\begin{pmatrix} \Omega^{+}_{0x}(k_{-j,i}) \\ \Omega^{+}_{0y}(k_{-j,i}) \\ \Omega^{+}_{1x}(k_{-j,i}) \\ \Omega^{+}_{1y}(k_{-j,i}) \end{pmatrix} = \begin{bmatrix} r^{(11)}_{11} & r^{(12)}_{11} & r^{(11)}_{12} & r^{(12)}_{12} \\ r^{(21)}_{11} & r^{(22)}_{11} & r^{(21)}_{12} & r^{(22)}_{12} \\ r^{(11)}_{21} & r^{(12)}_{21} & r^{(11)}_{22} & r^{(12)}_{22} \\ r^{(21)}_{21} & r^{(22)}_{21} & r^{(21)}_{22} & r^{(22)}_{22} \end{bmatrix} \begin{pmatrix} \Omega^{-}_{0x}(k_{m,n}) \\ \Omega^{-}_{0y}(k_{m,n}) \\ \Omega^{-}_{1x}(k_{m,n}) \\ \Omega^{-}_{1y}(k_{m,n}) \end{pmatrix}. \tag{5.38}$$

Transforming Equation (5.38) into rotated coordinates, we get

$$\begin{pmatrix} -\Omega'^{+}_{0x}(k'_{i,j}) \\ \Omega'^{+}_{0y}(k'_{i,j}) \\ -\Omega'^{+}_{1x}(k'_{i,j}) \\ \Omega'^{+}_{1y}(k'_{i,j}) \end{pmatrix} = \begin{bmatrix} r^{(11)}_{11} & r^{(12)}_{11} & r^{(11)}_{12} & r^{(12)}_{12} \\ r^{(21)}_{11} & r^{(22)}_{11} & r^{(21)}_{12} & r^{(22)}_{12} \\ r^{(11)}_{21} & r^{(12)}_{21} & r^{(11)}_{22} & r^{(12)}_{22} \\ r^{(21)}_{21} & r^{(22)}_{21} & r^{(21)}_{22} & r^{(22)}_{22} \end{bmatrix} \begin{pmatrix} -\Omega'^{-}_{0x}(k'_{-n,m}) \\ \Omega'^{-}_{0y}(k'_{-n,m}) \\ -\Omega'^{-}_{1x}(k'_{-n,m}) \\ \Omega'^{-}_{1y}(k'_{-n,m}) \end{pmatrix}. \tag{5.39}$$

Comparing (5.39) with (5.40), we obtain the transformation of the R-matrix under 90° rotation

$$r_{11}^{\prime(22)}(-j,i;-n,m) \longrightarrow r_{11}^{(11)}(i,j;m,n), \tag{5.40a}$$

$$-r_{11}^{\prime(21)}(-j,i;-n,m) \longrightarrow r_{11}^{(12)}(i,j;m,n), \tag{5.40b}$$

$$-r_{11}^{\prime(12)}(-j,i;-n,m) \longrightarrow r_{11}^{(21)}(i,j;m,n), \tag{5.40c}$$

$$r_{11}^{\prime(11)}(-j,i;-n,m) \longrightarrow r_{11}^{(22)}(i,j;m,n). \tag{5.40d}$$

The same transformation rule applies to r_{12}, r_{21}, and r_{22}.

The transformation of the R-matrix under the axis translations is simpler as a comparison with the axis rotation. Under axis translation

$$x \longrightarrow x' - x_0, \qquad y \longrightarrow y' - y_0, \tag{5.41}$$

the field directions and wave vectors remain unchanged

$$(k_x, k_y) \longrightarrow (k'_x, k'_y), \qquad (E_x, E_y) \longrightarrow (E'_x, E'_y). \tag{5.42}$$

Each plane-wave component of the EM field is transformed by

$$E(k_{i,j})e^{ik_i x + ik_j} \longrightarrow E'(k'_{i,j})e^{ik'_i x' + ik'_j y'} = E'(k'_{i,j})e^{ik_i x + ik_j y}e^{-ik_i x_0 - ik_j y_0}, \tag{5.43}$$

which yields to

$$E(k_{i,j}) \longrightarrow E'(k'_{i,j})e^{-ik_i x_0 - ik_j y_0}. \tag{5.44}$$

Recalling the definition of the R-matrix, we find the following transformation of the R-matrix under axis translation,

$$r'_{11}(i,j;m,n) \longrightarrow r_{11}(i,j;m,n)e^{i(k_i - k_m)x_0 + i(k_j - k_n)y_0} \tag{5.45}$$

and r_{12}, r_{21}, and r_{22} have the same transformation.

According to the above analysis, if the EM wave is normally incident on the 2D gratings, then the R-matrix of the second layer is just a 90°-rotation transformation from that for the first layer, which is block-diagonal. In this case, only the R-matrix for the first layer is needed, this greatly reduced the numerical calculations. The overall R-matrix for the 2D PBG gratings with arbitrary layers can be calculated on the basis of the first layer using the R-matrix addition technique shown in Equation (5.31). For arbitrary incidence angles, the R-matrix of the second layer is no longer a simple rotation-transformation from the first layer. Instead, we first make a transformation so that in the 90°-rotated coordinate the incident wave vector onto the second layer is $(k'_{0x}, k'_{0y}) = (-k_{0y}, k_{0x})$. Next, we calculate the R-matrix r' in this rotated coordinate using the same procedure for the first layer. Finally we back-transform this block-diagonal matrix to obtain the R-matrix r in the original coordinate according to Equation (5.39).

After we have obtained coefficients for the reflection and transmission waves, the transmission and reflection spectra are calculated by

$$T = \sum_{ij} T_{ij} = \sum_{ij} \frac{|\mathbf{E}^t_{ij}|^2 |k_{ij,z}|}{|\mathbf{E}_0|^2 |k_{0z}|} \tag{5.46}$$

and

$$R = \sum_{ij} R_{ij} = \sum_{ij} \frac{|\mathbf{E}^r_{ij}|^2 |k_{ij,z}|}{|\mathbf{E}_0|^2 |k_{0z}|}, \tag{5.47}$$

where the summation is over those homogeneous Bragg waves with a lateral wavevector $(k_{0x} + i\frac{2\pi}{d})^2 + (k_{0y} + j\frac{2\pi}{d})^2 \leq k_0^2$, and $\mathbf{E}^t_{ij}$ and $\mathbf{E}^r_{ij}$ are the amplitudes of the transmission and reflection Bragg wave in the $(ij)^{th}$ order.

Recursion relations and transmission and reflection spectra for the S-transfer matrix

In this section we shall only give the results, as the procedure for deriving the necessary formulas is nearly identical to those for the R-matrix case discussed previously. If $S^{(n)}$ is the overall S-matrix for n combined layers and $s^{(n+1)}$ is the S-matrix of the $(n+1)^{th}$ layer,

respectively, one straightforwardly proof, that the overall S-matrix for the combined $n+1$ layers is given by [?]:

$$S_{11}^{(n+1)} = s_{11}^{(n+1)} + [I - S_{12}^{(n)} s_{21}^{(n+1)}]^{-1} S_{11}^{(n)} \tag{5.48a}$$

$$S_{12}^{(n+1)} = s_{12}^{(n+1)} + s_{11}^{(n+1)} S_{12}^{(n)} [I - s_{21}^{(n+1)} S_{12}^{(n)}]^{-1} s_{22}^{(n+1)}, \tag{5.48b}$$

$$S_{21}^{(n+1)} = S_{21}^{(n)} + S_{22}^{(n)} s_{21}^{(n+1)} [I - S_{12}^{(n)} s_{21}^{(n+1)}]^{-1} S_{11}^{(n)}, \tag{5.48c}$$

$$S_{22}^{(n+1)} = S_{22}^{(n)} - [I - s_{21}^{(n+1)} S_{12}^{(n)}]^{-1} s_{22}^{(n+1)}. \tag{5.48d}$$

The procedure for finding the reflection and transmission spectra, is identical to that for the R-matrix case.

Advantages versus Drawbacks of the Modal Expansion Method

The MEM approach has several key advantages over all of the preceding methods. It is an order N^2 algorithm, since we apply the PW expansion only in a 2D scheme. It also awards a higher degree of accuracy compared to the TM method, since there is no attempt to represent the dielectric function of a spatial grid. (Remember the dielectric function is in reality a non-local function. In fact, it is a tensor.) This accuracy is displayed in Fig.5.3, where we compare a calculation performed using the TMM and one performed using the MEM to the experimental data for a metallic ISU layer-by-layer structure. Careful examination of the figures, shows that while the TMM at the most is able to provide a general qualitative agreement with the experimental data, the MEM method is actually able to pick up all of the features displayed in the experimental plot. Furthermore it allows for the extraction of the modal intensity distribution and, hence, offers a good estimate on the desired source profile for enhanced coupling (e.g., in wave guide designs). In addition, this method is very well adapted to the micro processing and machining techniques, and is directly extendable to all periodic structures. However, more importantly it is a very stable and versatile method.

In spite of all of these advantages, however, the MEM method suffers from a grave disadvantage. Because it was developed more or less within a PW framework, this immediately

implies that the results will be and are in fact slowly converging. This imposes severe demands on the computation time and memory. This problem can generally be reduced by further implementation of the crystal symmetry, and high-performance parallelization of the computer codes.

Bibliography

[1] L. Lifeng, 1996, *J. Opt. Soc. Am.* Vol. **13** 1024.

[2] Z.-Y. Li, 2002, *To be published.*

6 Dielectric Waveguides in Two-Dimensional Photonic Band Gap Materials

I. El-Kady, M. M. Sigalas, R. Biswas, and K. M. Ho.

A paper published in the Journal of Lightwave Technology, Vol. 17., No. 11, November 1999.

Introduction

Telecommunications and optical computing applications need efficient guiding of light on a single chip. Traditionally this has been accomplished by dielectric wave guides, such as optical fibers, which propagate light efficiently in straight lines. However, such dielectric wave guides are limited to a large bending radius, otherwise large radiation losses can occur, and new wave guides are needed to bend light around sharp corners.

A new direction is to use three-dimensional photonic band gap (*PBG*) crystals. By fabricating a wave guide or a channel in a three-dimensional (*3D*) photonic band gap crystal and operating at frequencies within the band gap, such wave guides overcome the problem of bending light around sharp corners[3].

However three-dimensional *PBG* crystals are still very difficult to fabricate at optical length scales. An alternative is to use simpler two-dimensional (*2D*) *PBG* crystals. Previous studies [4, 5] show that highly efficient transmission of light can be achieved around sharp corners in *2D PBG* wave guides. One major limitation to these studies is that the *2D* structure used was assumed to be infinite in the dimension perpendicular to the plane of periodicity. One would therefore expect leakage of waves in the practical situation of a finite structure.

Here we present simulations of the energy transport in such waveguides using a finite-difference-time-domain method. The geometry investigated consists of a three-layered dielectric structure in the dimension perpendicular to the plane of periodicity of the *2D PBG* structure, (Fig.6.1). The middle layer of which is to have a dielectric constant that is much larger than the other two enclosing layers. The dielectric contrast between the layers would then act to confine propagation to the central layer in exactly the same way as a conventional wave guide would.

Our proposed structure was first suggested by *Labilloy et al*[1], in conjunction with their studies of transmission and reflection off a *2D PBG* structure. The idea of including the three-layered dielectric structure was then used to guide the light out of the structure and into the measuring apparatus. In this article, however, we focus on the feasibility of such a structure as a wave guide.

As a first step in our studies, we will restrict ourselves currently to studying the guidance ability of this structure in straight lines. Comparison with the performance of a conventional guide is made, as well as discussions related to means and suggestions for enhancing its performance. Our studies also provide an upper theoretical limit on the performance of such guides, as we assumed no crystal imperfections and non-absorbing media. In the first part of our studies, the three-layer structure is studied in vacuum, in the second part, the three-layer structure is put on a high- dielectric-constant substrate to investigate the effects of substrate loss in the system.

Structural Parameters and Calculations

When investigating a wave guide design, our prime interest is to monitor the temporal and spatial development of the electromagnetic (EM) waves launched inside the guide. For this reason we employed the finite-difference-time-domain method ($FDTD$)[6], for the wave guide simulations.

A three layered dielectric structure is created along the z axis. The upper and lower dielectric layers are identical and are chosen to have a relative dielectric constant, ε, of either

1.00, 1.65, or 9.55 corresponding to *air, Aluminum Oxide* (Al_2O_3), or *Aluminum Gallium Arsenide* ($Ga_{0.2}Al_{0.8}As$) respectively. The central layer on the other hand, is chosen to have a considerably higher dielectric constant of 12.50 corresponding to *Gallium Arsenide (GaAs).* The height of the middle layer is chosen to have the values $0.43cm.$ or $0.86cm.$ and the overall structure height is $2.72cm.$

Two identical *PBG* structures consisting of a *2D* triangular lattice of air cylinders are drilled parallel to the z dimension of the dielectric structure, Fig.6.1. Each *PBG* structure consists of four bilayers of cylinders whose periodicity extend in the x and y dimensions of the structure. The two *PBG* structures will thus act to confine the propagation of the *EM* waves to the xy plane of the thin vertical channel that lies between them. The dielectric constant between the three dielectric layers will act concurrently to confine the *EM* wave propagation along the z dimension to the central high dielectric layer. Our wave guide is thus defined as the thin dielectric rectangular slab whose propagation axis lies parallel to the x dimension, and whose xz walls are tangent to the *PBG* cylinders while its xy walls lie along the interfaces between the central dielectric layer and the other two.

The number of air cylinders per yz bilayer in the *PBG* lattice, their radius, r, and their center-to-center separation (*lattice constant*), a, are determined by the particular choice of air-to-dielectric filling fraction, f, given by:

$$f = \frac{2\pi}{\sqrt{3}} \left(\frac{r}{a}\right)^2 \tag{6.1}$$

The structure extends an overall $14cm$ in the y dimension and $25cm$ in the x dimension. The width of the guide along the y dimension is chosen to be $0.94cm$.

In order to achieve good accuracy, the structure is divided into 640 by 360 by 108 grid points along the x, y, and z dimensions respectively, and a time step of $\Delta t = 0.682 \times 10^{-12}$ is chosen. The numerical space is terminated by second order *Liao* boundary conditions. To reduce the size of the computational problem and hence both the memory and time requirements, the symmetry displayed by our structure is utilized. The *EM* waves are launched into our guide by means of a dipole antenna situated at the center of the central dielectric layer with its axis

parallel to the y direction and extending $0.8cm$. Using the dipole source at various deriving frequencies, *Maxwell's* equations are integrated in time using the *FDTD* method to obtain the fields at each location within the structure. The symmetry plane that bisects the dipole antenna along its long axis is then recognized as a *magnetic image plane* (*magnetic wall*). The symmetry plane orthogonal to it and bisecting the guide feed, is on the other hand, is an *electric image plane* (*electric wall*). We thus need only model one fourth of the whole structure.

Before moving to the details of our calculations, however, we would like to mention that in order to compare our results with those experimentally observed by *Labilloy et al[1]*, at least from a qualitative point of view, a second structure in addition to the previous one is modeled. In this latter case a considerably large substrate of $GaAs$ is attached to the lower end of the structure, and the dimensions of the whole structure are re-adjusted so that they possess the same relative sizes as those studied experimentally.

To select the frequency of operation, the plane wave expansion technique [7, 8, 9], is first used to map out the photonic band structure for our *2D PBG* lattice for various choices of air-to-dielectric filling fraction, (Fig.6.2 a and b). As is well known from earlier work [7] there is a gap for the transverse electric (TE) modes, ($\mathbf{E}$ in the plane of the structure i.e. perpendicular to the cylinder axis), that opens up for filling fractions $f > 20\%$. The transverse magnetic (TM) modes have a much smaller gap that opens up for filling ratios $f > 60\%$, Fig.6.2b. Only a small region of filling fractions exists, between 60% and $\sim 85\%$, where the TE and the TM gaps overlap[7].

Throughout our calculations we shall therefore restrict ourselves to TE modes at a frequency of $10GHz$ because of the corresponding noticeable PBG width. We shall further restrict the majority of our studies to filling fractions of $20\%, 50\%$, and 80%. The choice of these particular filling fractions was done so as to sample regions on both sides of the gap as well as the region inside it. Other values of f are also studied to support our conclusions and predictions. Although our results are quoted at a frequency of $10GHz$ set by the dimensions in our simulation, our results can be scaled up to optical frequencies simply by scaling the

dimensions of the structure.

To effectively study the guidance ability of our structure, we need to examine both the spatial and temporal distribution of the *EM* waves as they progress through the structure. One way of doing so is by visualizing the *electric field* (**E**) *intensity* within planes that cut through the whole structure, see for example Figs.6.3 and 6.4. Two such sets of planes are selected. The first being the xy plane at the same level as our dipole, where the **E** field intensity is examined to study leakage losses out of the photonic structure. The second is the xz symmetry plane cutting through the center of the dipole, and is used to inspect the z localization of the *EM* waves inside the guide as well as losses into the surrounding air and/or substrate layers.

The disadvantage of the previous technique is that it provides no quantitative estimates of the *guidance efficiency,* η_g, or the *spacial decay rate,* α_x , of the waves in the guide. To complete the picture we therefore employ a second study technique. Here we monitor the *power,* P_g, carried by the *EM* waves as they progress through the guide by integrating the *Poynting vector,* **S,** within yz planes that slice through our guide perpendicular to the direction of propagation. P_g is then plotted versus time at each of these layers, Fig.6.6. The *time average* value of P_g is also calculated at each of these slicing planes and plotted versus displacement along the guide, Fig.6.7. These plots provide us with adequate information regarding η_g and α_x. The advantage of using **S** over the **E** *field intensity* is that not only does it provide information about the guided *power,* but also takes into account the *directionality* of wave propagation. In this way errors that are generated by including the reflected wave intensities are avoided.

Results and Discussion

The preliminary results indicate that the guidance features of our guide structure are highly sensitive to three major factors. The first is the height of the air cylinders relative to that of the guide itself, and is predominantly responsible for losses in the y direction. The second factor is the dielectric contrast between the central dielectric layer and the other two bounding layers, and is responsible for the losses in the z direction. Finally, the filling factor, f, of

air-to-dielectric which concurrently influences both y and z losses.

It is observed that decreasing the height of the air cylinders promotes part of the *EM* waves to seek the easy escape route and leak over the top of the air cylinders. The wave bypasses the photonic crystal and leaks out of the structure in the y direction. This agrees with the experimental observations cited by *Krauss et al*[2], and can easily be shown by comparing Fig.6.3a where the effective rod height is equal to that of the guide, and Fig.6.4a where the rods actually extend throughout the whole structure.

The influence of the dielectric contrast between the three dielectric layers is similar to that on the behavior of a conventional dielectric guide and is illustrated in Fig.6.3b and Fig.6.4b which shows greater confinement in the z direction for higher dielectric contrast between the outer and the inner layers. However, the problem arrises when trying to concurrently minimize both z and y losses as they require somewhat opposing conditions.

We study the performance of the waveguide by calculating the power traversing at different points along the guide (Fig.6.5) as a function of the air filling ratio f. The power in the waveguide is found by integrating the Poynting vector over different planes along the waveguide. We normalize the power in the waveguide by the power radiated by the dipole. For the high dielectric layer enclosed by two air layers, (Fig.6.6a), we find the lowest loss occurs for the conventional guide ($f = 100$ %), corresponding to a simple rectangular dielectric waveguide. However, with the *PBG* structure, the lowest loss is observed for filling ratios of 10 or 20% (Fig.6.6a), and substantially higher attenuation occurs for filling ratios of 50 or 80%. This result is surprising since the *PBG's* with filling ratios of 50-80% have the largest band gap and would be expected to be the best. The qualitative reason for this is that at filling ratios where *PBG* is best ($\sim$ 50%), there is little loss into the *PBG*, but there is instead loss in the z direction perpendicular to the waveguide. We find that this loss in the z direction can be reduced by going to a non-ideal *PBG* with filling fraction around 20%. This choice increases slightly the leakage in the plane but reduces the leakage in the z-direction, providing optimum performance. The best performance at 20%, has also been experimentally found by *Labilloy et al [1]*and *Krauss et al[2].* Evidently the leakage of the EM wave in the two directions can

not be reduced simultaneously.

Before concluding our current discussion, we would like to point out the effect of not etching-off the substrate on which such a structure would actually be grown on. Figures 6.7a and (6.7b) show a comparison between the predictions of our simulation on the geometry adopted by *Labilloy et al*[1] modeled with and without a substrate. It is obvious that including a substrate causes more losses. Such losses are seen to increase during the initial part of the guide (Fig.6.7a). They then level-off to a constant value when the guide mode is excited. Although this happens quite early, the power lost to the substrate is large enough to generally degrade the performance of the guide (Fig.6.8).

Conclusions

Upon comparing our current guide feature with those of a conventional dielectric guide of the same size, it is inevitable to conclude that the latter is in much better standing. However one possible suggested modification that is expected to enhance the performance of the guide is to replace each of the upper and lower dielectric slabs by a *1D* photonic crystal. Tuned so that it has an overlapping gap with our current *2D* one, it is expected to completely suppress the z losses. Unlike our current situation where the z scattering-off the *2D* lattice of the air cylinders seems unavoidable because of the large value of the *refractive index*, n, of the central dielectric slab[10], and no matter how large the dielectric contrast is, it cannot completely eliminate the z losses. However, the only drawback that faces such a design is that the cost relative to the gain is not expected to be very high, especially since a conventional dielectric guide is seen to function very well.

However one should make use of the ability of the *PBG* structures to reflect waves very efficiently and limit their function in a guide to bends. A feasible proposal is to use conventional dielectric guides to guide waves in the straight line segments of the required path and then to implement a *2D PBG* structure at any required bend along the path.

Acknowledgments

The author would like to thank D.D. Crouch for providing us with the *FDTD* code. The author would like also to acknowledge M.M. Sigalas, R. Biswas, and G. Tuttle for helpful discussions, and K.-M. Ho for suggesting this point of research and supervising this work. Finally, the author would like to thank both Ba. Shehadeh and J.S. AranthanII for technical support. This research was supported by the Office of Basic Energy Sciences U.S. Department of Energy. Ames Laboratory is operated for the U.S. DOE by Iowa State University under contract W-7405-Eng-82.

Bibliography

[1] D. Labilloy, H. Benisty, C. Weisbuch, T.F. Krauss, R.M. De La Rue, V. Bardinal, R.Houdre, U. Oesterle, D. Cassagne, and C. Jouanin, Phys. Rev. Lett. **21**, 4147(1997).

[2] T.F. Krauss, R.M. De La Rue, and S. Brand, Nature (London) **383**, 699(1996).

[3] M.M. Sigalas, R. Biswas, K.M. Ho, C.M. Soukoulis, and D.D. Crouch, *14th Annual Review of Progress in Applied Computaional Electrodynamics*, **Vol 1**, 144(1998).

[4] A. Mekis, J.C. Chen, I. Kurland, S. Fan, P.R.Villeneuve, and J.D. Joannopoulos, Pys. Rev. Lett. **77**, 3787(1996).

[5] S.Y. Lin, E. Chow, V. Hietala, P.R.Villeneuve, and J.D. Joannopoulos, Science **282**, 274(1998).

[6] A.Taflove, *Computational Electrodynamics, The Finite-Difference-Time-Domain Method* (Artech House Publishers, Boston, London, **Vol 1**, 1995).

[7] J.D. Joannoupoulos, R.D. Meade, J.N. Winn, *Photonic Crystals, Molding the Flow of Light* (Princeton University Press, Princeton, NJ, 1995).

[8] R.Biswas, M.M. Sigalas, C.M. Soukoulis, and K.M. Ho, *Photonic Band Structure in Topics in Computaional Materials Science*, e.d. C.Y. Fong (World Scientific, NJ, 1998).

[9] K.M. Ho, C.T. Chan, and C.M. Soukoulis, Phys. Rev. Lett. **65**, 3152(1990).

[10] D. Labilloy, H. Benisty, C. Weisbuch, T.F. Krauss,D. Cassagne, and C. Jouanin,R.Houdre, U. Oesterle,V. Bardinal, (To be published).

[11] Crouch, D.D., Advanced Electromagnetic Technologies Center, Raytheon Corporation.

[12] Sigalas, M., Private Communication, Ames Lab., Iowa State University of Sicence and Tech.

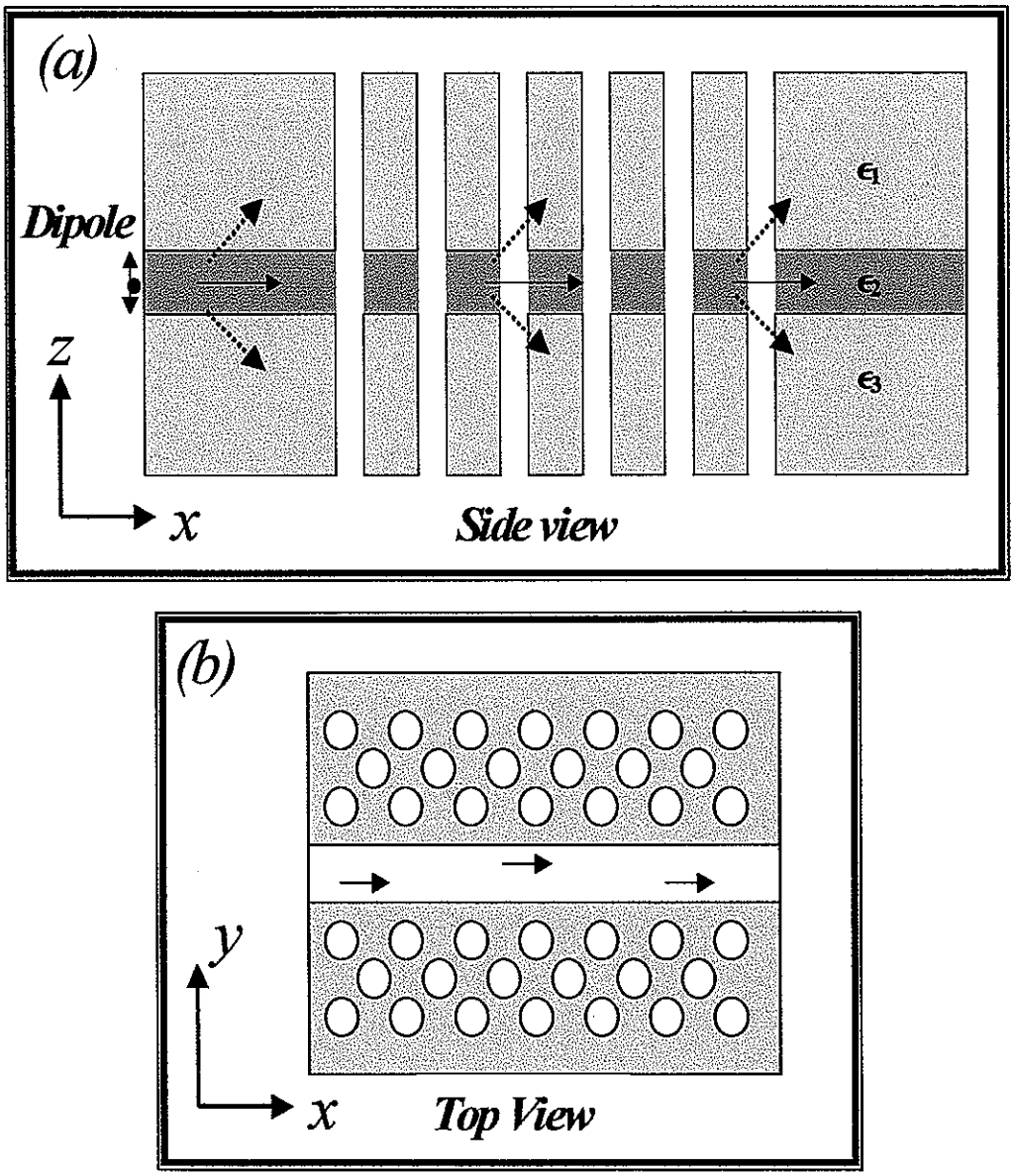

Figure 6.1 Waveguide Geometry. (a) Side view. (b) Top view.

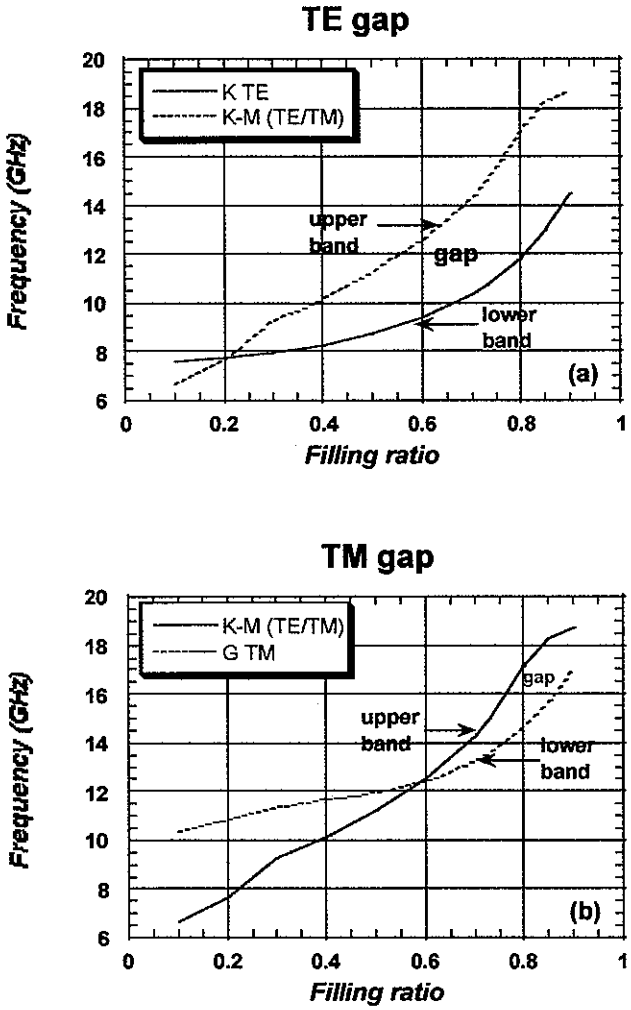

Figure 6.2 Photonic bandgap diagram for a hexagonal 2D lattice of air cylinders in a dielectric background. Lattice constant is 0.86cm. (a) TE polarization. (b) TM polarization.

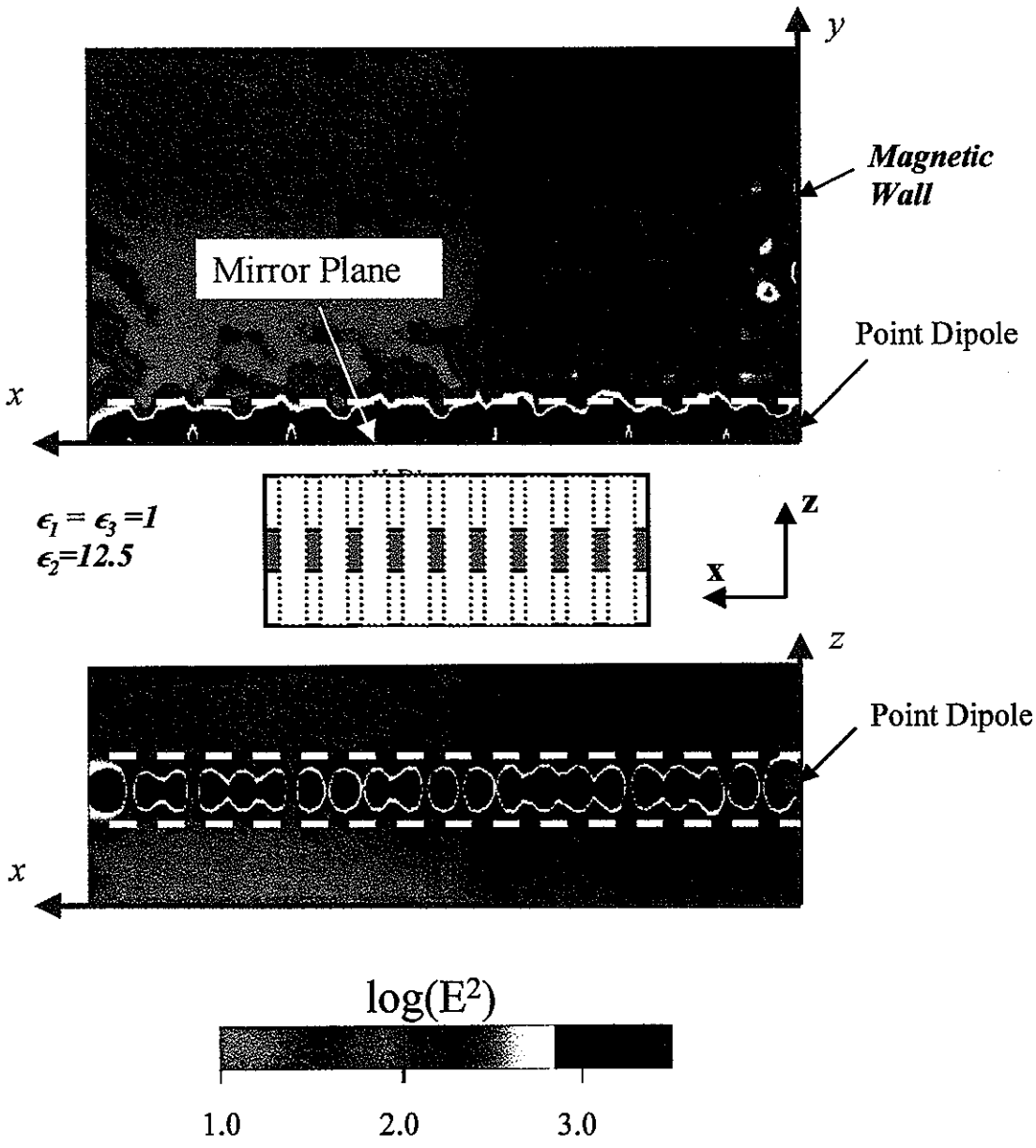

Figure 6.3 Electric field intensity at an air-todelectric fillig fraction f of 50%. The dielectric contrast between the central dielectric layer and the sandwitching ones is 12.5 : 1.0. (a) xy-plane slicing the structure at the same level as the dipole. We show here only one half of the structure as the xz-pane centered on the x-axiz acts as a symmetry mirror plane. (b) xz-symmetry plane slicing through the center of the structure.

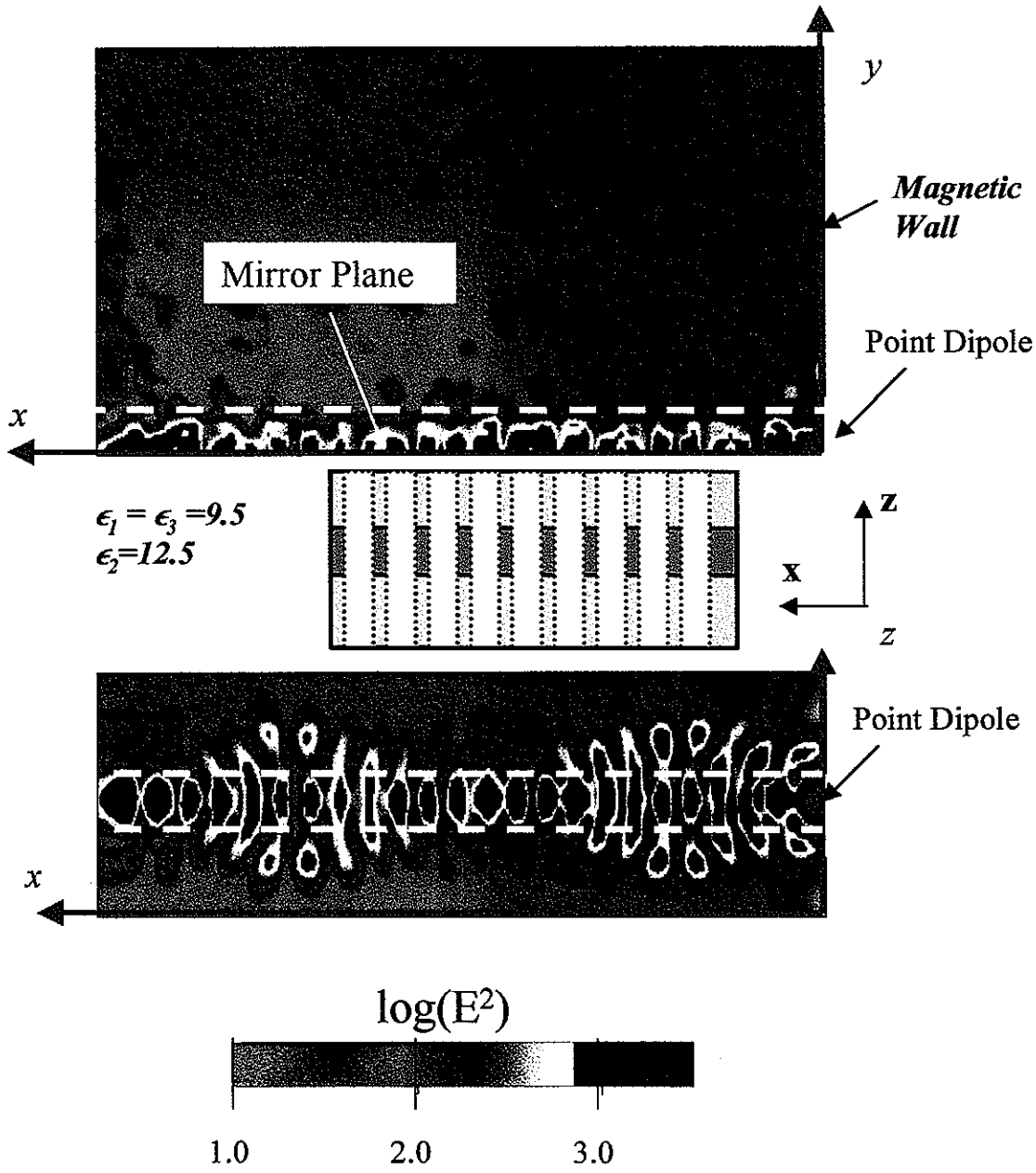

Figure 6.4 Electric field intensity at an air-todelectric fillig fraction f of 50%. The dielectric contrast between the central dielectric layer and the sandwitching ones is 12.5 : 9.5. (a) xy-plane slicing the structure at the same level as the dipole. We show here only one half of the structure as the xz-pane centered on the x-axiz acts as a symmetry mirror plane. (b) xz-symmetry plane slicing through the center of the structure.

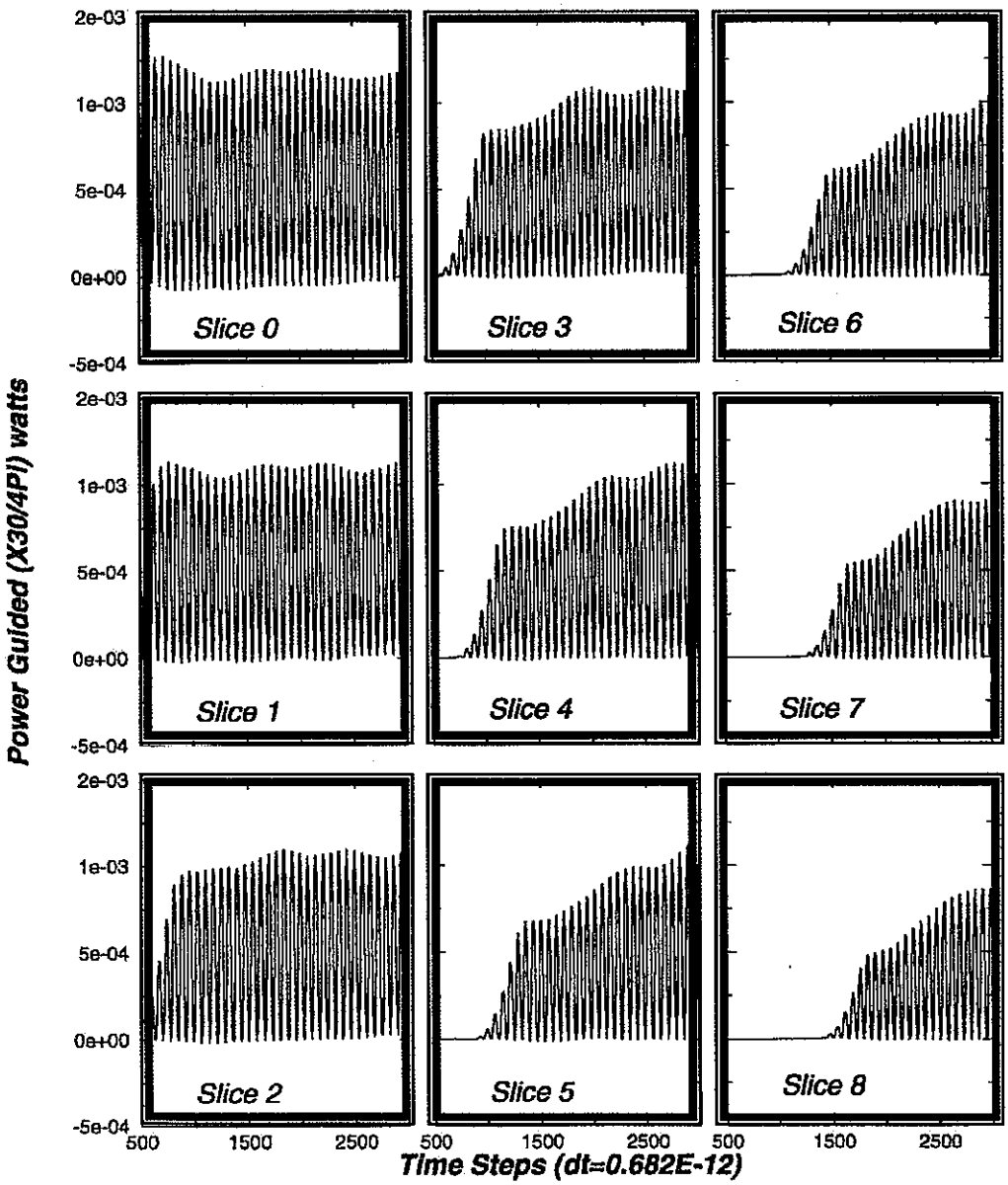

Figure 6.5 Power Guided P_g by the structure as it threads yz-planes slicing the guides perpindicular to the direction of propagation.

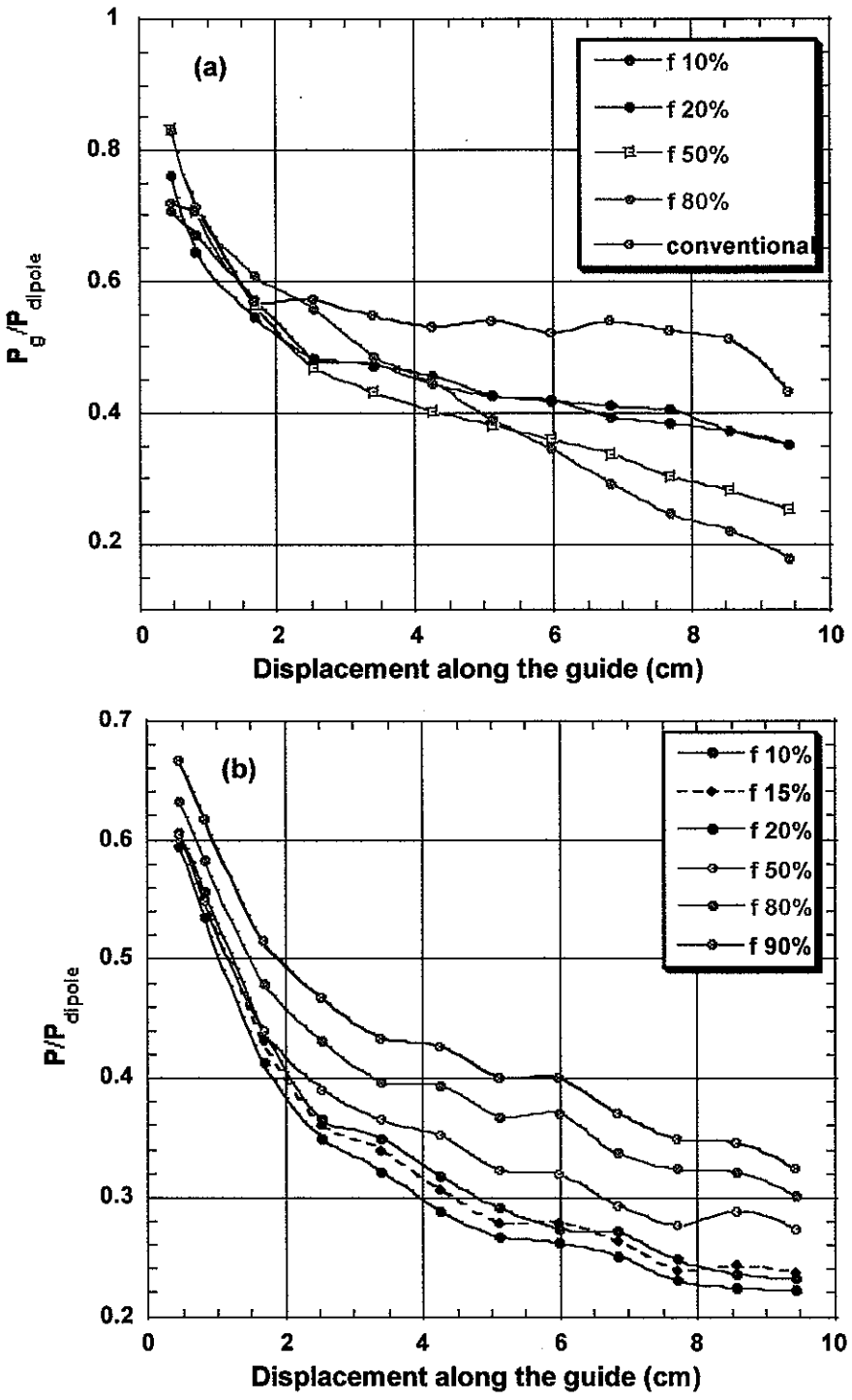

Figure 6.6 Time average value of the guided power over the first 1000 time steps, normalized relative to the power produced by the dipole. (a) Dielectric contrast of 12.5 : 1.0. (b) Dielectric contrast of 12.5 : 9.5.

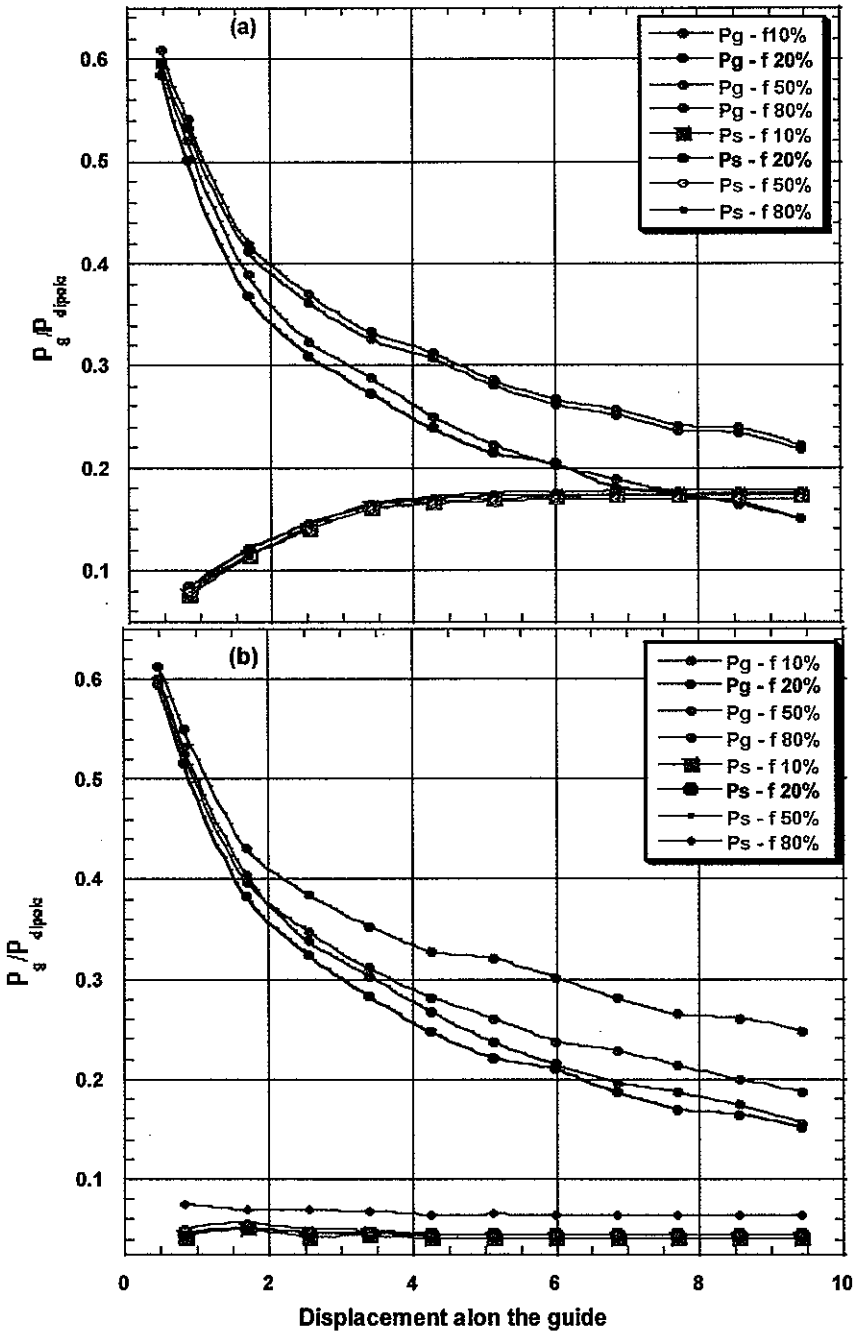

Figure 6.7 Time average value of the guided power over the first 1000 time steps, normalized relative to the power produced by the diole for the structure studied experimentally by Labilloy *et.al.* (a) With a substrate. (b) Without a substrate. P_s referes to the power lost to the substrate.

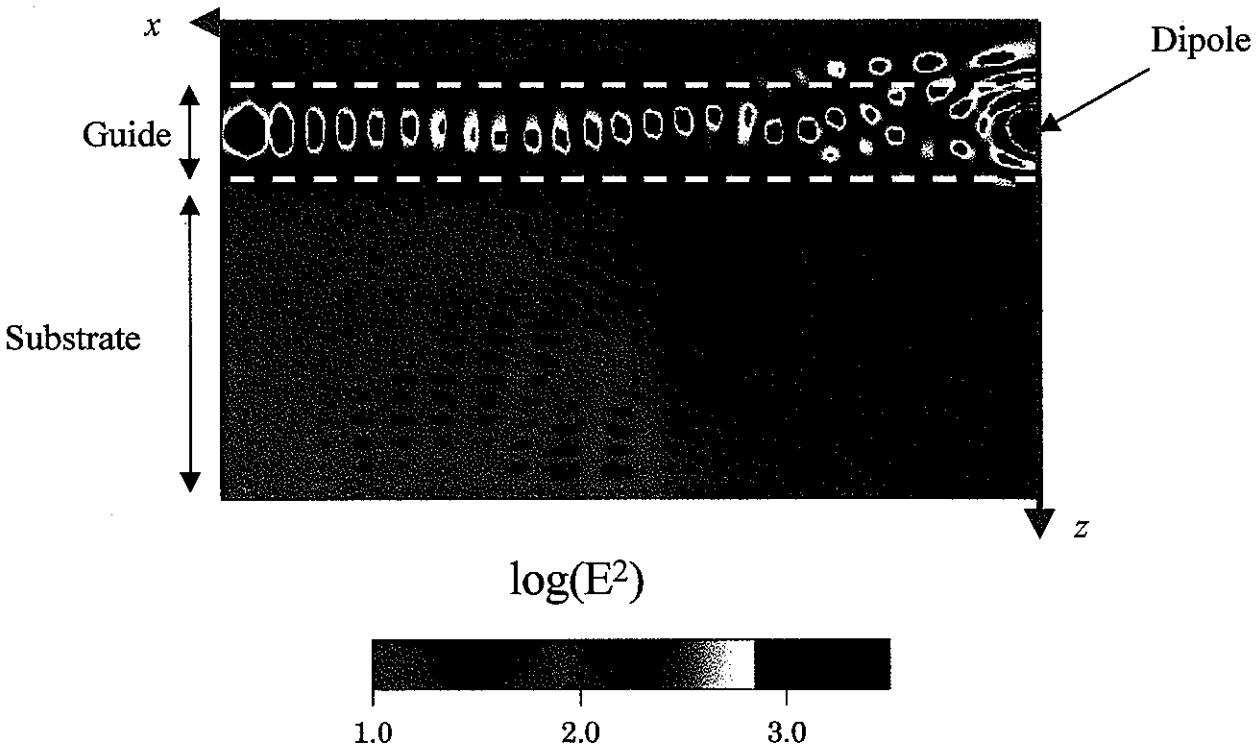

Figure 6.8 Electric field intensity at an air-todelectric fillig fraction f of 50%. in the xz-symmetry plane slicing through the center of the dipole for the structure studied by Labillo *et.al* [1].

7 Metallic Photonic Crystals at Optical Wavelengths

I. El-Kady, M. M. Sigalas, R. Biswas, K. M. Ho, C. M. Soukoulis,

Ames Laboratory and Department of Physics and Astronomy, Iowa State University, Ames IA 50011

A paper published in Physical Review B Journal, Vol. 62, No.23, December 2001.

Abstract

We theoretically study three dimensional metallic photonic band gap (PBG) materials at near infrared and optical wavelengths. Our main objective is to find the importantance of absorption in the metal and the possibility of observing photonic band gaps in such structures. For this reason, we study simple cubic structures where the metallic scatterers are either cubes or interconnected metallic rods. Several different metals have been studied (aluminum, gold, copper, and silver). Copper gives the smallest absorption and aluminum is more absorptive. The isolated metallic cubes are less lossy than the connected rod structures. The calculations suggest that isolated copper scatterers are very attractive candidates for the fabrication of photonic crystals at the optical wavelengths.

Introduction

There has been growing interest in the development of easily fabricated Photonic Band Gap (PBG) materials operating at the optical frequencies;[1] these are periodic dielectric materials exhibiting frequency regions where electromagnetic (EM) waves can not propagate. The reason for the interest in PBG materials arises from the possible applications of such materials in

several scientific and technical areas such as filters, waveguides, optical switches, cavities, design of more efficient lasers, etc.[1] Most of the research effort has been concentrated in the development of two-dimensional (2D) and three-dimensional (3D) PBG materials consisting of positive and frequency independent dielectrics[1], in which case one can neglect the possible problems related to the absorption. Here we offer an alternative approach to the fabrication of PBG materials using metals. There are several studies of metallic photonic crystals which are mostly concentrated at microwave, millimeter-wave, and far infrared frequencies.[2–9] In such frequencies, metals act almost like perfect reflectors with no significant absorption problems. Here, on the other hand, we focus on the infrared and near-optical ferequency regime. There are certain advantages of introducing metals to photonic crystals. These include reduced size and weight, easier fabrication methods and lower costs. A recent theoretical study suggested that a face centered cubic lattice of metallic scatterers can possess a complete photonic band gap.[10] However, the absorption of the metal was completely ignored. Here, we use the transfer matrix method to study the effect of absorption of the metal at frequency regime of interest (infrared and near optical frequencies). In particular, we study simple cubic structures consisting of isolated metallic cubes or interconnected metallic rods. Aluminum, copper, gold and silver have been used in order to investigate the effect of different metals on the absorption. In all the cases the lattice constant was chosen to be 0.25 microns and the metallic scatterers are assumed to be imbedded in air.

Approach

We utilize the frequency dependent dielectric functions $\epsilon_1(\omega), \epsilon_2(\omega)$ for these metals that have been directly measured by Ordal et al [11] from near infrared to optical frequencies (1 cm^{-1} to 20000 cm^{-1}). This provides a very realistic base for the photonic response of metallic structures composed of such elements. To aid the numerical calculation, the measured real and imaginary dielectric functions have been interpolated with a Drude model to yield the desired value of (ϵ_1, ϵ_2) at any frequency. The Drude dispersion model offers an excellent fit to the

measured data over a wide frequency range.[11]

$$\epsilon_1(\omega) = \epsilon_\infty - \frac{\omega_p^2}{\omega^2 + \omega_\tau^2} \tag{7.1}$$

$$\epsilon_2(\omega) = \frac{\omega_p^2 \omega_\tau}{\omega^3 + \omega \omega_\tau^2} \tag{7.2}$$

The the plasma frequency ω_p, and the damping frequency ω_τ, have been tabulated in Ref. 11, by fitting the Drude dispersion model to experimental measurements. The values for ω_p and ω_τ are [11], 3570/19.4 THz (Al); 1914/8.34 THz (Cu); 2175/6.5 THz (Au); and 2175/4.35 THz (Ag). These values fit the experimental data for (ϵ_1, ϵ_2) over frequencies from 30-900 THz, which covers the entire range of interest. The resulting dispersion relations for the real and imaginary parts of the dielectric constants of the above four metals are shwon in Figs. 7.1a and 7.1b.

Calculations and Results

The metallic photonic crystals studied here are the three dimensional counterparts of frequency selective surfaces (FSS).[12] These are two dimensional arrays of metallic patches or aperture elements that have frequency filtering properties. FSSs have been studied in great detail because of their application as filters, bandpass radomes, polarizers, and mirrors in microwave region. [12] Most FSS work has focused on a single-layer metal patterns.

We use the transfer-matrix method (TMM), introduced by Pendry and MacKinnon,[13] to calculate the EM transmission through the PBG materials. In the TMM, the total volume of the system is divided in small cells and the fields in each cell are coupled to those in the neighboring cells. Then, the transfer matrix is defined by relating the incident fields on one side of the PBG structure to the outgoing fields on the other side. Using the TMM, the band structure of an infinite periodic system can be calculated, but the main advantage of this method is the calculation of the transmission and reflection coefficients for EM waves of various frequencies incident on a finite thickness slab of the PBG material. In that case, the

material is assumed to be periodic in the directions parallel to the interfaces.

The TMM has been used to simulate the reflection and transmission from a simple cubic structure with metallic cubes at the lattice sites, occupying a filling fraction of 29.5 %. Three unit cells constitute the thickness of the slab. The unit cell is discretized into 12 divisions, so that the 3-unit cell structure is described by a 12x12x36 mesh. This mesh accurately describes the present cubes. We have checked the convergence of the calculations and found the high frequency results to be well converged for this choice of discretization.

Figure 7.2 shows the transmission and absorption of a three unit cell thick structure consisting of metallic cubes of 29.5 % filling ratio. There is a broad drop in transmission around 400 THz for all metals. The gap is wider for aluminium where the real part of the dielectric function $\mid \epsilon_1(\omega) \mid$ has the largest absolute value at these frequencies[11]. In contrast, copper exhibits a narrower gap because it has a smaller value of $\mid \epsilon_1(\omega) \mid$. The absorption $\epsilon_2(\omega)$ is higher for aluminum generating the largest absorption feature in Fig.7.1b. The absorption for gold and copper is less than 5% for all the frequencies below the upper edge of the gap. For higher frequencies, there are peaks in the absorption which indicate that the wave penetrates more in the metal. Usually, a peak appears in the absorption close to the frequency where a peak appears in the transmission. Aluminum however displays a greater amount of absorption over the frequency range of the gap.

We also studied defects in a simple cubic structure consisting of metallic cubes. Defects are introduced by reducing the size of the cubes in the middle layer by 50 %. This defect introduces a peak in the transmission within the gap region (Fig. 7.3). This may have been generated due to the displacement of the transmission peak at the low frequency side of the gap (250 THz in Fig.7.1a) to higher frequencies. The transmission at the top of the peak is 0.97, 0.95, 0.95 and 0.52 for copper, gold, silver and aluminum, respectively. The lower transmission for aluminum is due to the higher absorption at the defect peak (Fig. 7.3) which is as high as 0.42 for aluminum while being less than 0.05 for copper, gold and silver.

Figure 7.4 shows the transmission and absorption for the case where the metal forms an network of square rods connecting nearest neighbors in a simple cubic lattice. The filling ratio

of the metallic rods is 0.26. In that case there is a gap from zero up to a cutoff frequency in accordance with previous studies.[5] The cutoff frequency is at 410, 510, 520 THz for copper, gold/silver and aluminum, respectively. This trend is again related to the real part of the dielectric constant; the higher its absolute value, the higher is the corresponding cutoff frequency. On the other hand the absorption is higher for aluminum and smaller for copper due to the higher (lower) value of the imaginary part of the dielectric constant for aluminum (copper). For aluminum rods, there is a broad absorption feature around 375 THz similar to the case for isolated cubes, which arises from the greater losses in aluminum compared to the other metals.

Defects in the interconnected structure are introduced by removing the metal inside a cube centered on the lattice points of the second layer. Defect peaks appear in the transmission (Fig.7.5) around 230 THz. The transmission on top of the peaks is 0.62, 0.43, 0.37, and 0.05 for copper, silver, gold and aluminum, respectively. In contrast, there is an opposite trend for the absorption which is 0.1, 0.28, 0.2, and 0.35 for copper, gold and aluminum, respectively. Both of these trends are related to the higher (lower) value of the imaginary part of the dielectric constant of aluminum (copper). We found higher absorption for the connected rods case than in the isolated metallic cubes. This is an expected result since the interconnected structures long range conduction currents are induced which lead to higher losses[14]. Losses may be further reduced by using dielectric structures coated with a thin layer of metal[15],this may lead to promising structures with gaps[15].

Conclusions

In conclusion, we studied metallic photonic crystals at near infrared and optical wavelengths with the transfer matrix method. Our results show that robust mettalic PBGs may be obtained by using metals. By corectly choosing the metalic parameters, in paricular the damping frequency, an impinging electromagnetic radiation is foud to interact with the PBG crystal sufficiently enough to be scattered by it, but not too much as to be absorbed by it. Our studies focused on the absorption of such metallic structures for that reason we studied

only the simple cubic geometry. Although this type of geometry does not result in the widest possible gaps, it constitutes the simplest possible case study. We expect that our conclusions regarding the absorption will hold to any other metallic structures. By comparing the results for different metals, we found that copper gives the less possible absorption in all the cases. Gold gives slightly higher absorption. Aluminum is very lossy and is not recommended for optical photonic crystals. Isolated metallic scatterers have lower losses than the interconnected metallic networks. The most promising configuration for an optical photonic crystal is the isolated metallic scatterers composed of copper. Both silver and gold are acceptable although slightly lower in performance. Defects in this structure introduce a narrow defect band that acts as a frequency selective filter.

Ames Laboratory is operated for the U.S. Department of Energy by Iowa State University under contract No. W-7405-Eng-82.

Bibliography

[1] For a recent review, see the articles in J. of Lightwave Technology **17**, 1728-2405 (1999); M. M. Sigalas et. al. Photonic Crystals, Encyclopedia of Electrical Engineering, **16**, pp. 345 (1999).

[2] D. R. Smith, S. Schultz, N. Kroll, M. Sigalas, K. M. Ho, and C. M. Soukoulis, *Appl. Phys. Lett.*, **65**, 645 (1994).

[3] E. R. Brown and O. B. McMahon, Appl. Phys. Lett. **67**, 2138 (1995); K. A. McIntosh et. al., Appl. Phys. Lett. **70**, 2937 (1997).

[4] A. A. Maradudin and A. R. McGurn, Phys. Rev. B **48**, 17576 (1993).

[5] M. M. Sigalas, C. T. Chan, K. M. Ho, and C. M. Soukoulis, Phys. Rev. B **52**, 11744 (1995).

[6] J. S. McCalmont, M. M. Sigalas, G. Tuttle, K. M. Ho, and C. M. Soukoulis, Appl. Phys. Lett. **68**, 2759 (1996).

[7] D. F. Sievenpiper, M. E. Sickmiller, and E. Yablonovitch, Phys. Rev. Lett. **76**, 2480 (1996).

[8] E. Ozbay, et. al., Appl. Phys. Lett. **69**, 3797 (1996); B. Temelkuran, et. al., Appl. Phys. A **66**, 363 (1998).

[9] S. Gupta, G. Tuttle, M. Sigalas, and K. M. Ho, Appl. Phys. Lett. **71**, 2412 (1997); S. Gupta, Ph.d. thesis, Iowa State University (1998).

[10] A. Moroz, Phys. Rev. Lett. **83**, 5274 (1999).

[11] M. A. Ordal, L. L. Long, R. J. Bell, S. E. Bell, R. R. Bell, R. W. Alexander, Jr., and C. A. Ward, Applied Optics **22**, 1099 (1983); M. A. Ordal, R. J. Bell, R. W. Alexander, Jr., L. L. Long, and M. R. Querry, Applied Optics **24**, 4493 (1983).

[12] "Frequency selective surface and grid array," edited by T. K. Wu (Wiley, New York, 1995).

[13] J. B. Pendry and A. MacKinnon, Phys. Rev. Lett. **69**, 2772 (1992); J. B. Pendry, J. Mod. Opt. **41**, 209 (1994).

[14] J. D. Joannopoulos, P. R. Villeneuve, and S. Fan, Nature **386**, 143 (1997).

[15] W. Y. Zhang, X. Y. Lei, Z. L. Wang, D. G. Zheng, W. Y. Tam, C. T. Chan, and P. Sheng, Phys. Rev. Lett. **84**, 2853 (2000).

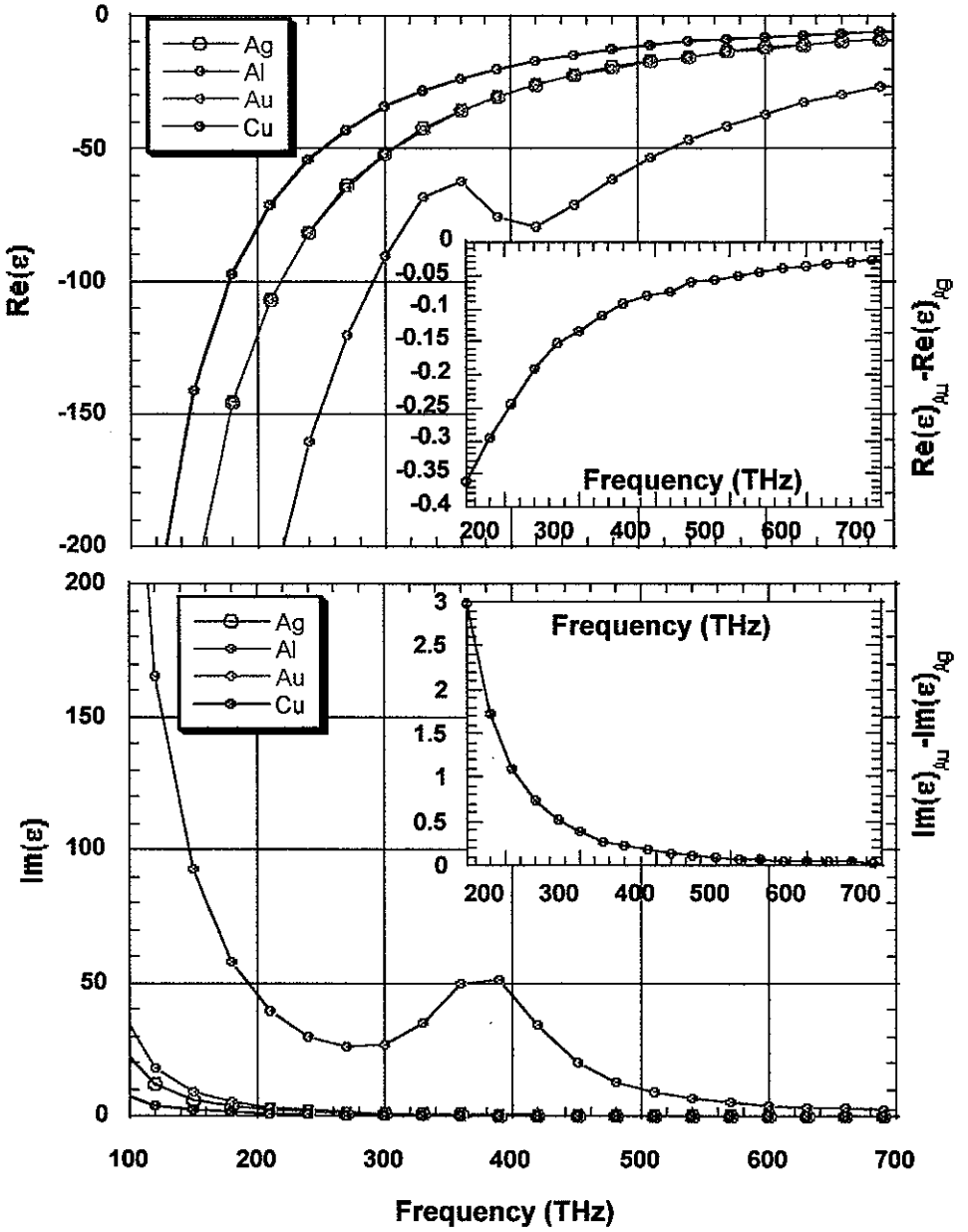

Figure 7.1 Dispersion relations for Al, Ag, Au, and Cu. (a) Real part of the dielectric constant. (b) Imaginary part of the dielectric constant. The inset in both plots shows the small difference between Au, and Ag.

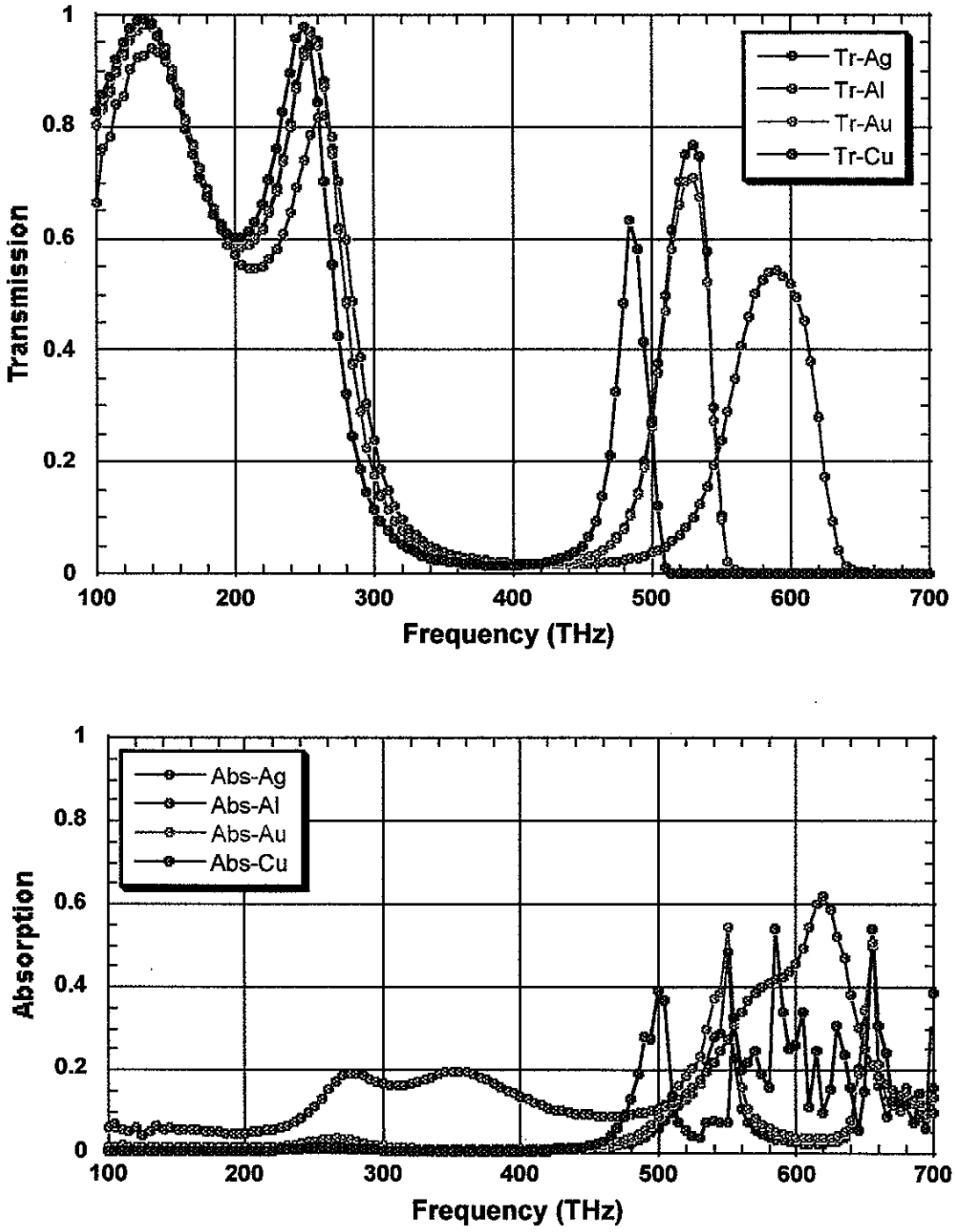

Figure 7.2 Transmission and absorption for a simple cubic structure consisting of isolated metallic cubes. The filling ratio of the cubes is 29.5%. The propagation is along the 100 direction and the structure is three unit cells thick.

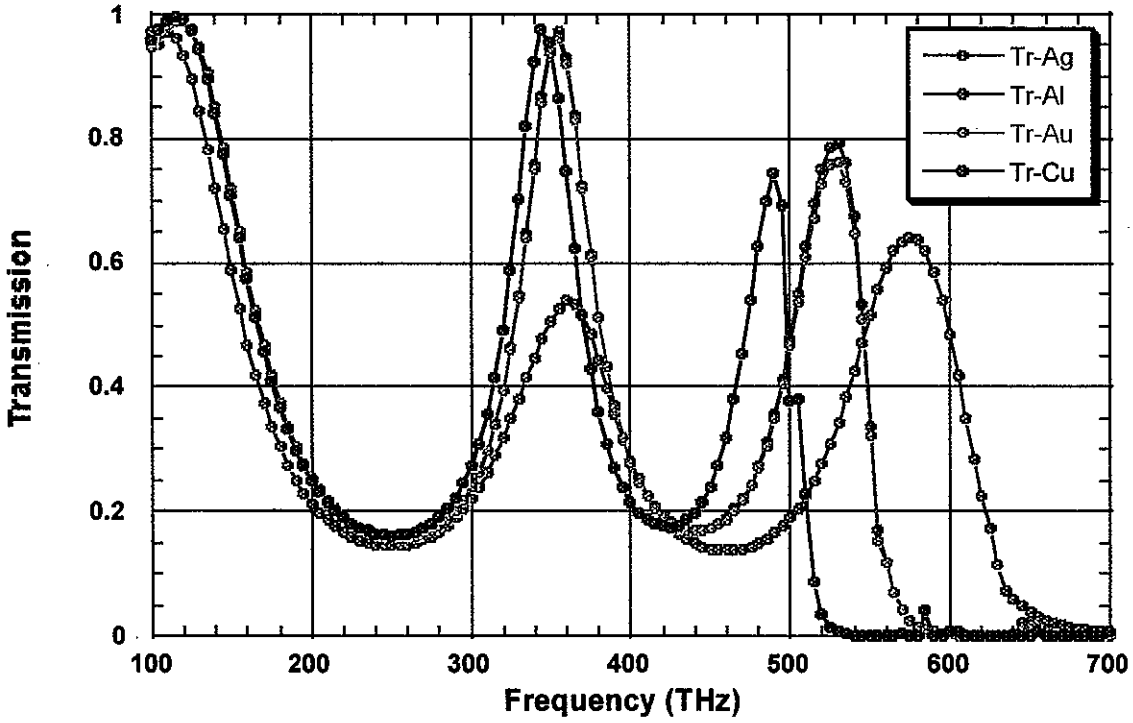

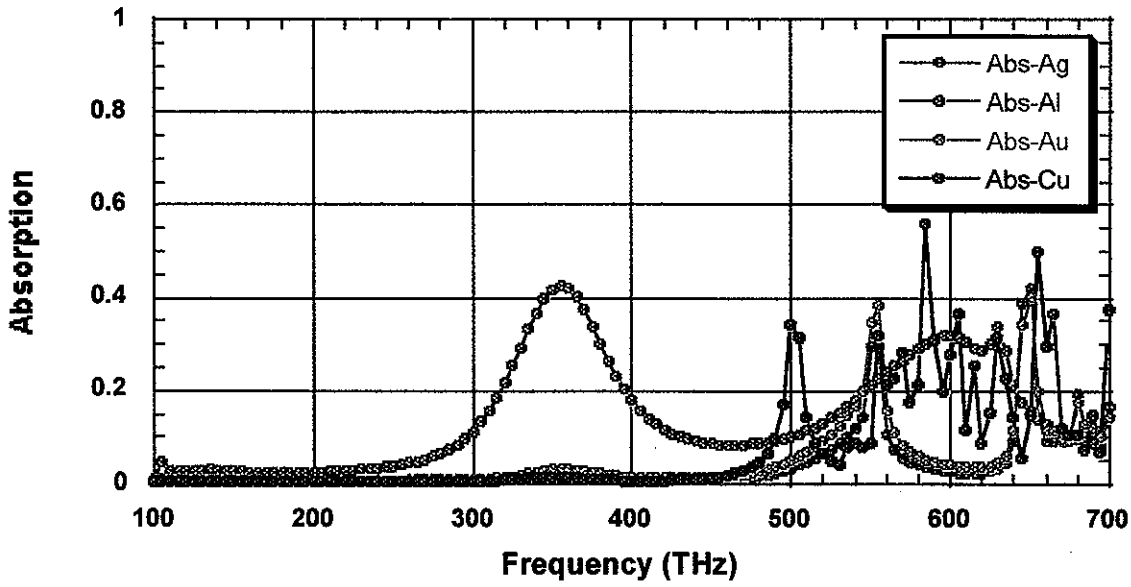

Figure 7.3 Transmission and absorption for a simple cubic structure consisting of isolated metallic cubes. Defects have introduced in the structure by reducing the size of the cubes in the second layer. The filling ratio of the cubes is 21%. The propagation is along the 100 direction and the structure is three unit cells thick.

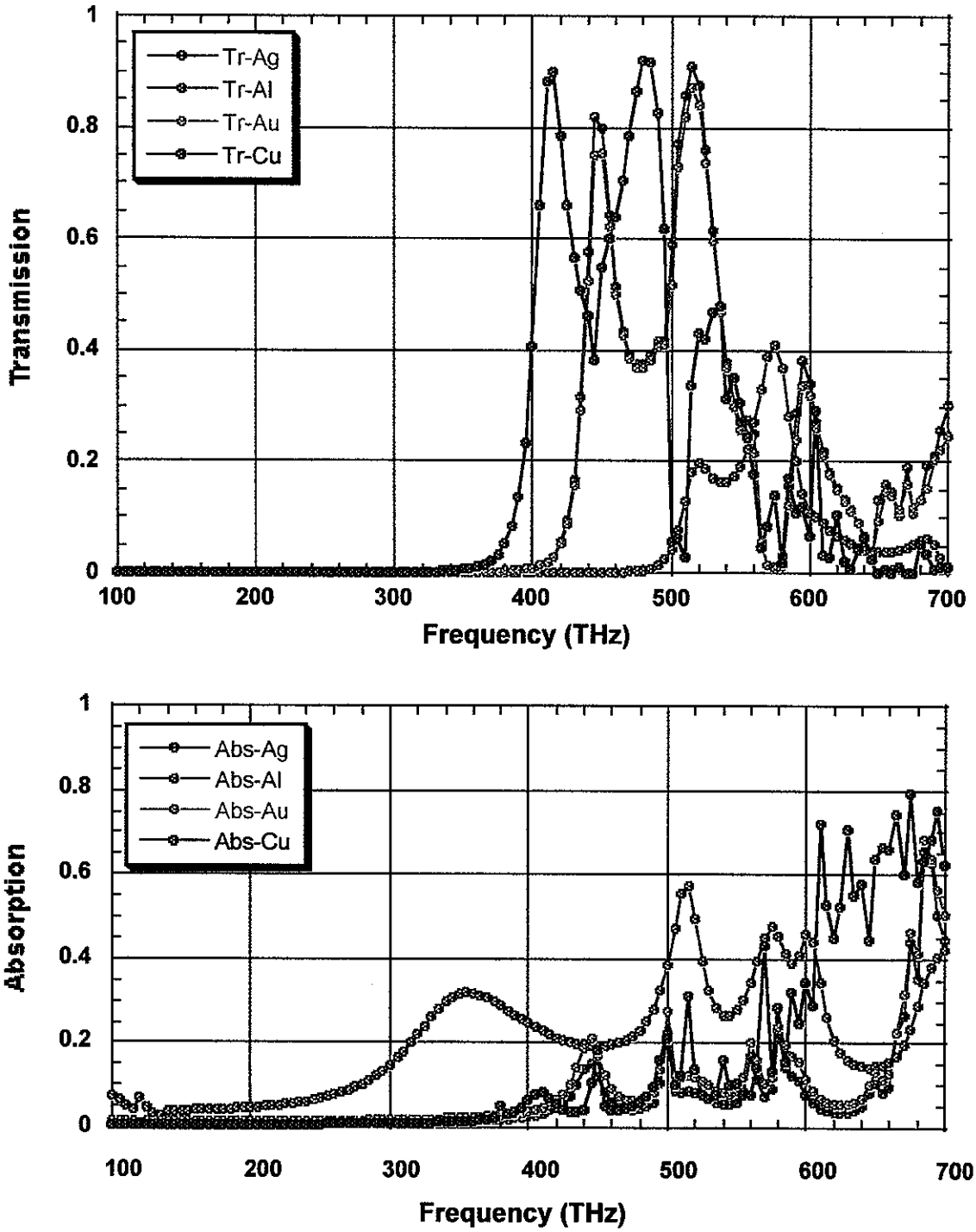

Figure 7.4 Transmission and absorption for a simple cubic structure consisting of interconnected metallic square rods. The filling ratio of the metal is 26%. The propagation is along the 100 direction and the structure is three unit cells thick.

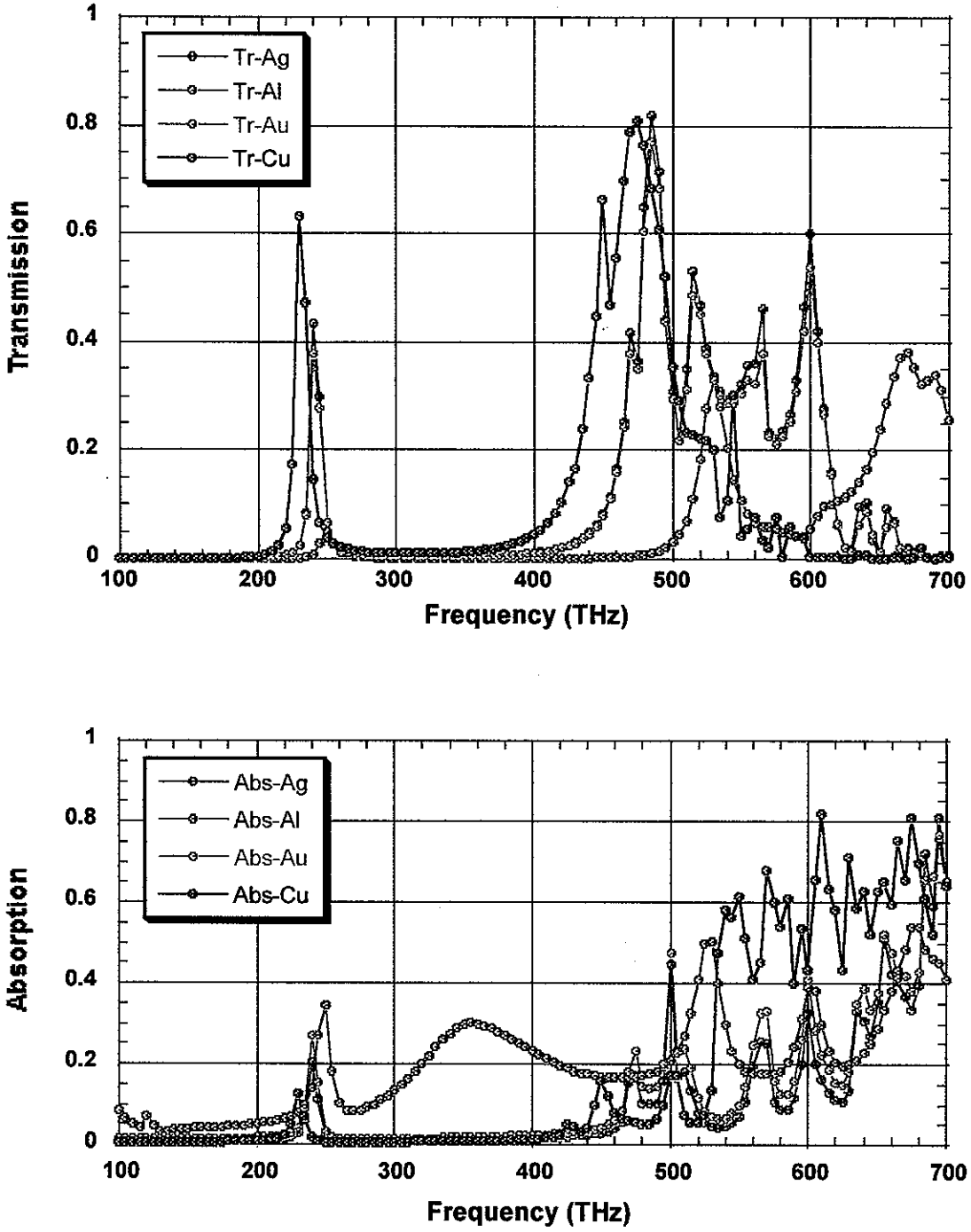

Figure 7.5 Transmission and absorption for a simple cubic structure consisting of interconnected metallic square rods with defects. The defects are created by removing the metal which is inside a cube centered in the lattice points of the second layer. The filling ratio of the metal is 21%. The propagation is along the 100 direction and the structure is three unit cells thick.

8 All Metallic, Absolute Photonic Band Gap Three-dimensional Photonic-Crystals for Energy Applications

J.G. Fleming, S.Y. Lin,

MS 0603, Sandia National Laboratories, P.O. Box 5800, Albuquerque, NM 87185

and

I. El-Kady, R. Biswas and K.M. Ho

Ames Laboratory, Department of Physics and Astronomy, Iowa State University, Ames, Iowa 50011

A paper published in the Journal Nature, Vol.417, May 2002.

Abstract

We point out a new direction in photonic crystal research that involves the interplay of photonic band gap (PBG) rejection [1-3] and photonic band edge absorption. It is proposed that an absolute PBG may be used to frustrate infrared part of Black-body emission and, at the same time, its energy is preferentially emitted through a sharp absorption band. Potential application of this new PBG mechanism includes highly efficient incandescent lamps and enhanced thermophotovoltaic energy conversion [4]. Here, a new method is proposed and implemented to create an all-metallic 3D crystal at infrared wavelengths, λ, for this purpose. Superior optical properties are demonstrated. The use of metal leads to the opening of a large and absolute photonic band gap (from $\lambda \sim 8\mu m$ to $> 208\mu m$). The measured attenuation strength of ~ 30 dB/ per unit cell at $\lambda = 12\mu m$ is the strongest ever reported for any 3D

crystals at infrared λ. At the photonic band edge, the speed-of-light is shown to slow down considerably and an order-of-magnitude absorption enhancement observed. In the photonic allowed band, $\lambda \sim 5\mu m$, the periodic metallic-air boundaries mold the flow of light, leading to an extraordinarily large transmission enhancement. The realization of 3D absolute band-gap metallic photonic crystal will pave the way for highly efficiency energy applications and for combining and integrating different photonic transport phenomena in a photonic crystal.

Introduction

It is known that a 3D metallic photonic crystal is promising for obtaining a larger photonic band gap [5-7], for achieving new EM phenomenon [8-10] and for high temperature ($> 1,000^oC$) applications. However, metals offer theoretical challenges in the investigation of photonic band gap behavior especially in the infrared (IR) and optical wavelength, as they are often dispersive and absorptive [11]. The difficulties in fabricating 3D metallic crystal in the IR and optical wavelengths present another challenge. So far, studies of metallic photonic crystals are mostly concentrated at microwave and millimeter wavelengths [9, 12-13]. One exception is work done by Mclntosh et al on infrared metallodielectric photonic crystals [7]. Also, fabrication of optical metallic 3D crystal using self-assembly method is just emerging [14,15].

In this work, fabrication of a Tungsten 3D photonic crystal was realized using a newly proposed method. It is done by selectively removing Si from already fabricated polysilicon/SiO2 structures, and back filling the resulting mold with chemical vapor deposited (CVD) Tungsten. This method can be extended to create almost any 3D single-crystal metallic photonic crystals at infrared λ, which are previously not achievable by any other means. A SEM image of the fabricated four-layer 3D Tungsten photonic crystal is shown in Fig.8.1a and (8.1b).

Experimental Measurements, Theoretical Calculations and Discussion

The optical properties of the 3D Tungsten photonic crystal are characterized using a Fourier-transform infrared measurement system for wavelengths ranging from $\lambda = 1.5$ to $25\mu m$ [16]. To obtain reflectance (R), a sample spectrum was taken from a 3D Tungsten crystal first

and then normalized to a reference spectrum of a uniform silver mirror. To find the absolute transmittance (T), a transmission spectrum taken from a 3D Tungsten crystal sample was normalized to that of a bare silicon wafer. This normalization procedure is intended to calibrate away extrinsic effects, such as light reflection at the air-silicon interface and silicon absorption. For tilt-angle transmission measurements, the sample is mounted onto a rotational stage with a rotational angles spanned from $\theta = 0^o$ to 60^o, measured from the surface normal, i.e. <001> direction.

The absolute reflectance (black diamonds) and transmittance (blue circles) of a four-layer 3D Tungsten photonic-crystal is shown in Fig.8.2a. Light propagates along the <001> direction of the crystal and is un-polarized. The reflectance exhibits oscillations at $\lambda < 5.5\mu m$, raises sharply at $\lambda \sim 6\mu m$ (the band edge) and finally reaches a high reflectance of 90% for $\lambda > 8\mu m$. Correspondingly, the transmittance shows distinct peaks at $\lambda < 5.5\mu m$, decreases sharply at $\lambda \sim 6\mu m$ (the photonic band edge) and then vanishes to below 1% for $\lambda > 8\mu m$. The dashed line is for reference purpose and is a transmittance taken from a $6000\mathring{A}$ uniform Tungsten film. The simultaneous high R and low T at $\lambda > 8\mu m$ is indicative of the existence of a photonic band gap in the Tungsten 3D photonic crystal. The attenuation is as large as $\sim 30dB$ at $\lambda = 10\mu m$ for our 4-layer sample, or equivalently a unit cell. The multiple oscillations at $\lambda < 5.5\mu m$ are attributed to photonic density-of-states (DOS) oscillations in the photonic allowed band.

To confirm our experimental observation, a transfer-matrix calculation [5] of transmittance and reflectance is carried out and the results shown in Fig.8.3. The structure parameters used are the same as the fabricated structure other than it has a slightly higher filling fraction, 33.3%. A frequency dependent dielectric functions $\epsilon_1(\omega)$, $\epsilon_2(\omega)$ for Tungsten were also used to take into account the dispersion and absorption effects [17, 18].

Fig.8.3a shows the computed result for a 4-layer (N=4) 3D crystal, which correctly predicts photonic band edge position and the gap size. More importantly, the transmittance (blue color curve) also shows a high transmission at $\lambda \sim 5\mu m$. Although, the computed peak value (80%) is about three-times higher and the full-width-half-maximum ($\sim 0.5\mu m$) three times narrower than the measured one. By increasing N from 6 to 8 and 10, the peak transmission drops

monotonically from $\sim 95\%$ to $\sim 75\%$, due to absorption loss. Surprisingly, there exists a sharp absorption peak (red color spectrum) at $\lambda \sim 6-7\mu m$. The peak λ is near the band edge and its absorptance is $\sim 50\%$. Using a photoaccoustic spectroscopy technique [19], a direct absorption measurement is performed and a clear absorption peak of 22% is observed at $\lambda \sim 6\mu m$. For comparison, the absorptance for an uniform Tungsten-film at this λ is measured to be $\sim 1\%$. For $\lambda < 4.5\mu m$, computed reflectance ($> 75\%$) is much higher than the observed one ($20 - 30\%$). Since metallic absorption loss is not important in this λ-range [17], the observed low R is attributed to scattering losses. One source of scattering is structure imperfections such as the keyholes shown in Fig.8.1.

The photonic band gap attenuation in a 3D metallic photonic crystal must not be confused with typical metallic attenuation. To illustrate this point, transmission spectra for 3D crystals of different number-of-layers, N=2, 4 and 6, were computed and the results shown in Fig.8.3b. The dashed line is a reference spectrum taken from a uniform 6000Å Tungsten-film. Consistent with its small metallic skin-depth ($300 - 500\mathring{A}$ for $1\mu m < \lambda < 25\mu m$), the Tungsten-film transmittance is very low (T$< 10^{-8}$) and is nearly λ-independent. The sample spectrum, on the other hand, exhibits a much higher transmission (T$\sim 10-1$) for $\lambda < 6\mu m$, suggesting that photonic transport in this spectral range is not dominated by metallic attenuation. Moreover, a strong λ-independent and N-dependent is observed in the band gap regime ($\lambda > 8\mu m$). This N-dependence indicates that transmittance attenuation at $\lambda > 8\mu m$ scales with layer-thickness of our 3D structure, but not the metallic skin depth. Thus, the attenuation at $\lambda > 8\mu m$ is due primarily to photonic band gap effect. The attenuation constant in the photonic band gap is very large. It is ~ 32, 56 and $64dB$ per unit cell at $\lambda = 10$, 20 and $40\mu m$, respectively. This means that as few as one unit cell of a 3D Tungsten crystal is sufficient for achieving strong electromagnetic waves attenuation.

To prove the existence of absolute metallic photonic band-gap, i.e. a common band gap for light propagating in all directions, a tilt-angle reflection experiment was conducted. Five tilt-angle spectra were shown in Fig.8.2b for $\theta = 10$, 30, 40, 50 and 60^o, respectively. As θ is increased, the band edge position moves from $\lambda \sim 6\mu m$ for $\theta = 10^o$ to $\lambda \sim 8\mu m$ for

$\theta = 60^o$. Nonetheless, both the oscillating features at $\lambda < 6\mu m$ and the high reflectance at longer wavelength remain for all θs. Despite the shift in band edge, a large complete photonic band-gap exists, from $\lambda \sim 8\mu m$ to $\lambda > 20\mu m$, for our 3D Tungsten photonic crystal. Such an extraordinarily large band gap is ideally suited for suppressing broadband Blackbody radiation in the infrared [20] and re-cycling its energy into the visible spectrum. In the photon recycling process, an absolute 3D photonic band gap completely frustrates IR thermal emission and forces the radiation into a selective emission band. Consequently, energy is not wasted in heat generation, but rather been re-channeled into a useful emission band. According to Kirchoff's law, the integrated absorptance equals integrated emissivity [21]. The absorption peak near band edge (see Fig.8.3) is then an ideal channel for light emission. As a Tungsten 3D crystal can be heated up to an elevated temperature of $> 1500C$, the emission band can be tailored to be in the visible, giving rise to a highly efficient incandescent lamp. This new phenomenon is based on a powerful interplay between photonic band gap rejection and photonic band edge enhanced absorption, which is made possible by the creation of a 3D metallic crystal. This photonic band gap mechanism for energy recycling has major energy consequences in thermal-photovoltaic (TPV) application as well [4]. Using our 3D structure as an emitter, a TPV model calculation [4] shows that the TPV conversion efficiency reaches 51%, which is to be compared to 12.6% efficiency for a Black-Body emitter.

A 3D metallic crystal not only exhibits a strong photonic band gap, but also posses unique transmission and absorption characteristics. It is noted that while transmittance through a uniform $6000\mathring{A}$ Tungsten-film is extremely small $T < 10^{-8}$, peak transmission through 3D W-crystal sample at $\lambda \sim 5\mu m$ is high, T$\sim 25-30\%$. We may also approximate our 3D structure as arrays of sub-wavelength holes and the estimated transmission efficiency is also small, 3×10^{-5} [22]. Here, the hole-radius is estimated from the straight opening shown in the inset of Fig.8.1a. None of the above two approximations can explain the observed transmission enhancement. A further transfer-matrix calculation reveals that the transmission peak λ scales linearly with lattice constant a and depends on material filling-fraction. A similar enhancement effect and scaling behavior have also been observed in 2D metallic thin film hole-arrays and was attributed

to surface plasma excitation [23]. However, its peak λ is independent of the hole-diameter, or equivalently hole filling-fraction. The surface plasmon picture is useful in describing EM modes in thin films with small holes, where the film thickness is small compare with λ [23]. It is likely that plasmon effect will play a role. However, a formal theoretical classification of the nature of the EM modes in complex structures as ours would give better insights into this extraordinary phenomenon. Such EM modes must also manifest the 3D crystal symmetry and facilitate waveguiding through metallic openings [24]. To explore the manner by which light-wave manages to mold itself according to the intricate 3D metallic structure (and to the Bloch Theorem), a FDTD calculation is carried out.

FDTD Calculations are done for a six-layer 3D crystal sample at three different λs ($\lambda = 5.2$, 6.5 and $12\mu m$) and at two separate time steps T ($= 1\Delta t = 0.133 \times 10^{-12} second$ and $2\Delta t$). This calculation assumes a perfect metallic boundary condition, as Tungsten material absorption is minimal at these λs [17]. Here the Δts are chosen to display the transient and steady state electromagnetic wave distribution, respectively. The color plot is expressed in a logarithmic scale and shows electric intensity profile in the y-z plane. The light source is a continuous wave point source, indicated by arrows, and is placed at mid-point of the first layer (L=1). The Tungsten rods show up as red regions. At $\lambda = 5.2\mu m$ and $T = 1\Delta t$, see Fig.8.4a, light-wave intensity (the dark blue color) diverges in y-direction and meanwhile its wave-front propagates along z-axis up to L=6. At $T = 2\Delta t$, Fig.8.4b, light has transported uniformly through all six layers and its intensity reached a steady state. It is noted that, at the metallic boundaries, there exists a strong field gradient, from red, green to blue, encompassing the metallic rods. These periodic metallic-air boundaries mold the flow of light and dictate its Bloch-wave transport characteristics. At $\lambda = 6.5\mu m$, Fig.8.4c and (8.4d), light also diverges in y-axis, propagates less intensively toward L=4 at $T = 1\Delta t$ and eventually through L=6 at $T = 2\Delta t$. Additionally, the speed-of-light is slowed down considerably at this λ. The weaker transmission and the retarded speed-of-light are clear manifestation of light propagation at a photonic band edge. This retardation, along with percolation of light through the 3D structure, may be responsible for the large absorption at $\lambda = 6 - 7\mu m$. Here, the very unique photonic band edge behavior

leads to order-of-magnitudes absorption-enhancement. At $\lambda = 12\mu m$ (see Fig.8.4e and 8.4f), light does not transport through the six-layer structure and is totally reflected back, as it is in the photonic band gap region.

Potential Application

Finally, we address feasibility and challenges for realizing practical incandescent lamps. The first challenge involves the creation of metallic photonic crystals in the visible wavelengths. The minimum feature size needs to be made 10 times smaller, i.e.$100 - 200nm$. Current commercially available optical lithographic steppers can produce feature size of $150 - 180nm$ over a $12 - inch$ silicon wafer and down to $120nm$ by year 2002. These steppers are designed for large-scale production with high yields, which should help driving the production cost down. Another alternative is to use direct electron-beam write lithographic technique, although it is more costly. It is also noted that a photonic band gap is effective only when infrared light is emitted within the 3D photonic crystal. Emission from the sample surfaces would experience less photonic band gap effect. One solution is to passivate the surface layers. By applying a thin insulating surface coating, electrical current can only pass through bulk portion of the 3D crystal, and high emission efficiency is again achievable.

Experimental Methods: Creation of a 3D single-crystal metallic photonic crystal

Details on the fabrication of the polysilicon/SiO2 3D photonic crystal, which formed the basis of the Tungsten-molds, are given in reference-16. Briefly, the 3D silicon photonic crystal consists of layers of one-dimensional rods with a stacking sequence that repeats itself every four layers (a unit cell), and has a face-center-tetragonal lattice symmetry [25]. Further details on the rest of the processing steps are as follows. Firstly, the polysilicon in a 3D silicon photonic crystal was removed using a $6M$, $85C$ KOH etch which has a selectivity of $\sim 100:1$. Over-etch during the KOH process, which is required to ensure the removal of all the poly-silicon, results in the formation of a "V" structure on the bottom of the layer contacting the substrate. This

is due to etching of the underlying substrate. The KOH etch effectively stops when the etch-front encounters the slow etching {111} planes of the substrate, thus forming a "V" groove (see Fig.8.1). However this artifact does not appear to significantly impact photonic band gap performance. Secondly, the blanket CVD Tungsten film does not adhere to silicon dioxide and was therefore grown on a 50nm thick TiN adhesion layer deposited by reactive ion sputtering. The bulk of the Tungsten film was deposited at high pressure ($90 Torr$) from WF6 and H2. The chemical vapor deposition of Tungsten results in films of very high purity; the film resistivity was $10 microOhm - cm$. The step coverage of the deposition process is not 100% and this gives rise to the formation of a keyhole in the center of the more deeply imbedded lines (see Fig.8.1b). However, the resulting thickness is far greater than the skin depth of Tungsten and the parts typically retain sufficient structural integrity to be handled readily. And lastly, excess Tungsten on the surface was removed by chemical mechanical polishing and the oxide mold was removed with a 1 : 1 HF solution, which etches SiO2 but not Tungsten or TiN. All of the techniques employed throughout are modifications of standard CMOS processes and all work was performed on commercially available, monitor grade, six-inch silicon wafers.

Acknowledgement

The authors thank Dr. J. Gees and J. Moreno for valuable discussion and M. Tuck and J. Bur for technical support. The work at Sandia National Laboratories is supported through DOE. Sandia is a multi-program laboratory operated by Sandia Corporation, a Lockheed Martin Company, for the United States Department of Energy. This research was supported by the Office of Basic Energy Sciences U.S. Department of Energy. Ames Laboratory is operated for the U.S. DOE by Iowa State University under contract W-7405-Eng-82.

Bibliography

[1] Yablonovitch, E. Inhibited spontaneous emission in solid-state physics and electronics, Phys. Rev. Lett. 58, 2059-2062 (1987).

[2] John, S. Electromagnetic absorption in a disordered medium near a photon mobility edge, Phys. Rev. Lett. 53, 2169-2172 (1984).

[3] Genack, A. & Garcia, N. Observation of photon localization in a three-dimensional periodic array, Phys. Rev. Lett. 66, 2063-2067 (1991).

[4] Zenker, M. , Heinzel, M., Stollwerck, G., Ferber, J., and Luther, J., Efficiency and power density potential of combustion-driven thermophotovoltaic systems using GaSb photovoltaic cells, IEEE Trans. Elec. Dev. 48, p. 367-376 (2001).

[5] Sigalas, M.M., Chan, C.T., Ho, K.M. and Soulokous, C.M., Metallic photonic band-gap materials, Phys. Rev. B52, 11744-11751 (1995).

[6] Fan, S., Villeneuve, P.R., and Joannopoulos, J.D., Large omnidirectional band gaps in metallodielectric photonic crystals, Phys. Rev. B54, 11245-11251 (1996).

[7] Mcintosh, K.A., et. al., Three-dimensional metallodielectric photonic crystals exhibiting resonant infrared stop bands, Appl. Phys. Lett. 70, 2937-2939 (1997).

[8] Sievenpiper, D.F., Sickmiller, M.E., and Yablonovitch, E., 3D wire mesh photonic crystals, Phys. Rev. Letts. 76, 2480-2483 (1996).

[9] Moroz, A., Three-dimensional complete photonic-band-gap structures in the visible, Phys. Rev. Letts. 83, 5274-5277 (1999).

[10] Pendry, J.B., Negative refraction makes a pefect lens, Phys. Rev. Letts, 85, 3966-3969 (2000).

[11] For a general reference, please see Handbook of Optical Constants of Solids, p. 275-409, edited by E.D. Palik, (Academic Press, San Diego, USA, 1998).

[12] Ozbay, E., et. al., Defect structures in metallic photonic crystals, Appl. Phys. Lett. 69, 3797-3799 (1996).

[13] Sievenpiper, D.F., Yablonovitch, E., Winn, J.N., Fan, S., Villeneuve, P.R., and Joannopoulos, J.D., 3D metallo-dielectric photonic crystals with strong capacitive coupling between metallic islands, Phys. Rev. Letts. 80, 2829-2832 (1998).

[14] Velev, O.D., Kaler, E. W., Structured porous materials via colloidal crystal templating: from inorganic oxides to metals, Adv. Mater. 12, 531-534 (2000).

[15] Zakhidov, A.A., et. al., Three-dimensionally periodic conductive nanostructures: network versus cerment topologies for metallic PBG, Synthetic Metals 116, 419-426 (2001).

[16] Lin, S.Y., et. al., A three-dimensional photonic crystal in the infrared wavelengths, Nature 394, 252-253 (1998).

[17] M.A. Ordal, et al., Optical properties of the metals Al, Co, Cu, Au, Fe, Pb, Ni, Pd, Pt, Ag, Ti, and W in the infrared and far infrared, Applied Optics 22, 1099-1119 (1983).

[18] El-Kady, I., Sigalas, M.M., Biswas, R., Ho, K.M., and Soukoulis, C.M., Metallic photonic crystals at optical wavelengthsm Phys. Rev. B 62,15299-15301 (2000).

[19] McClelland, J.F., Jones, R.W., Lou, S., and Seaverson, L.M., A Practical guide to FTIR photoaccoustic spectroscopy, in Practical sampling teciniques for infrared analysis, P.B. Coleman, Ed. (CRC Press, Boca Raton, Florida, 1993), Chapter 5.

[20] Lin, S.Y., Fleming, J.G., Chow, E., and Bur, J., Enhancement and suppression of thermal emission by a three-dimensional photonic crystal, Phys. Rev. B 62, R2243, (2000).

[21] "Infrared Detectors and Systems", by E. L. Dereniak and G.D. Boreman, John Wiley & Sons, New York, 1996, p.74, Ch.2.

[22] Bethe, H.A. Theory of diffraction by small holes. Phys. Rev. 66, 163-182 (1944).

[23] Ebbesen, T.W., Lezec, H.J., Ghaemi, H.F., Thio, T., Wolff, P.A., Extraordinary optical transmission through sub-wavelength hole arrays, Nature 391, 667-669 (1998).

[24] Porto, J.A., Garcia-Vidal, F.J., Pendry, J.B., Transmission resonance on metallic gratings with very narrow slits, Phys. Rev. Lett. 83, 2845-2848 (1999).

[25] Ho K. M. et al, Photonic band gap in three-dimensions: new layer-by-layer periodic structure, Solid State Communi. 89, 413-416 (1994).

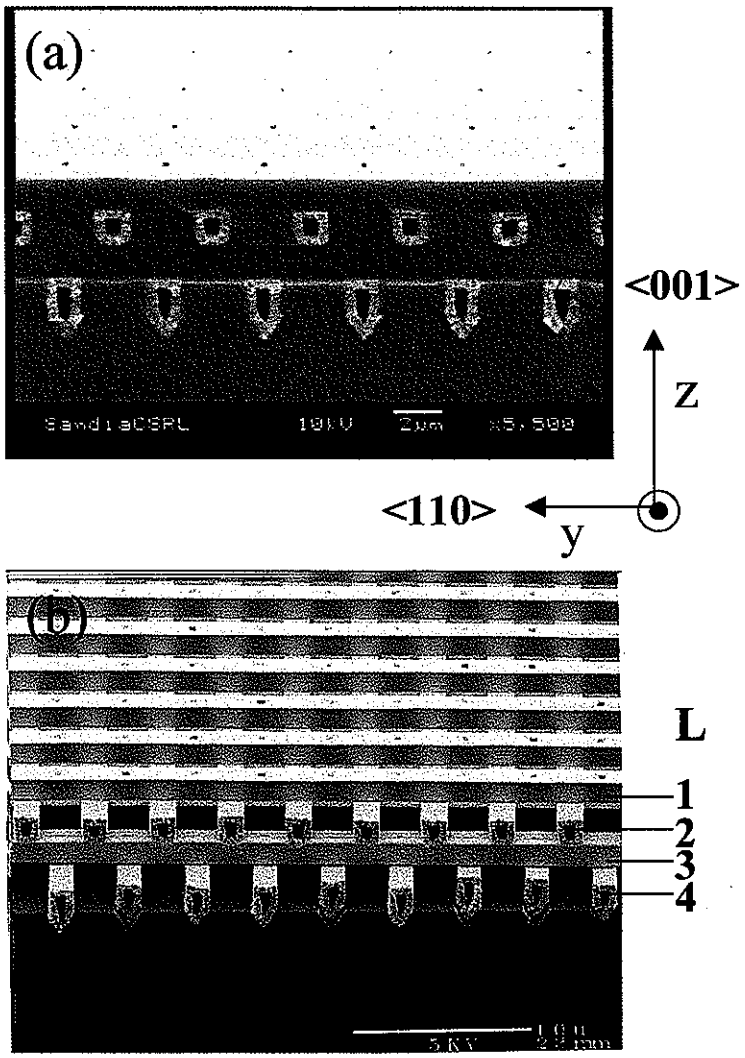

Figure 8.1 Images of a 3D Tungsten photonic crystal, taken by a Scanning Electron Microscope (SEM). The images taken with and without oxide are shown in 1(a) and 1(b), respectively. The 1D Tungsten rod-width is $1.2\mu m$, the rod-to-rod spacing is $4.2\mu m$ and the filling fraction of Tungsten material is 28%. The bottom "V" groove is formed due to a slow KOH etching {111} planes of the (001) oriented silicon substrate. The step coverage of the deposition process is not 100% and this gives rise to the formation of a keyhole in the center of the more deeply imbedded lines.

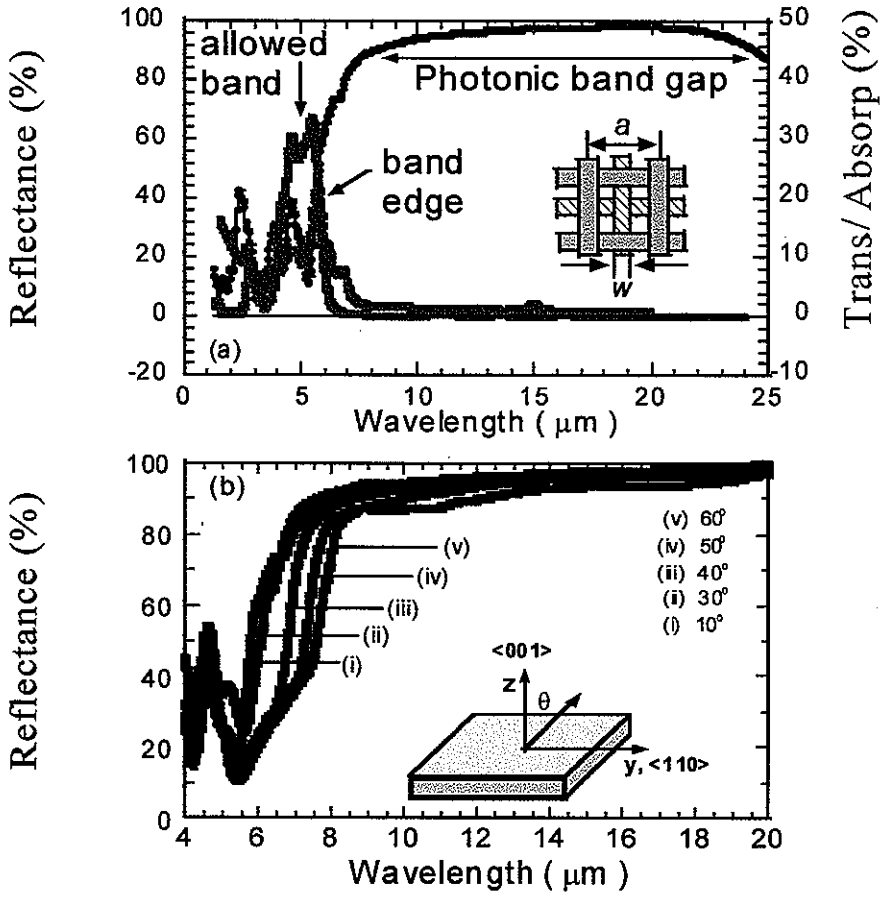

Figure 8.2 (a) The measured reflectance (black diamond), transmission (black circles) and absorptance (red circles) spectra for light propagating along <001> axis. The inset shows a schematic top view of the 3D crystal. (b) Tilt-angle reflectance spectra taken from the 4-layer Tungsten photonic crystal. The crystal orientation is tilted from the <001> to <110> axes and the light incident angle (θ) is therefore systematically tilted away from $\Gamma - X$\ toward $\Gamma - L$ of the first Brillouin zone. The tilt angle is varied from $\theta = 10$, 30, 40, 50 and 60°.

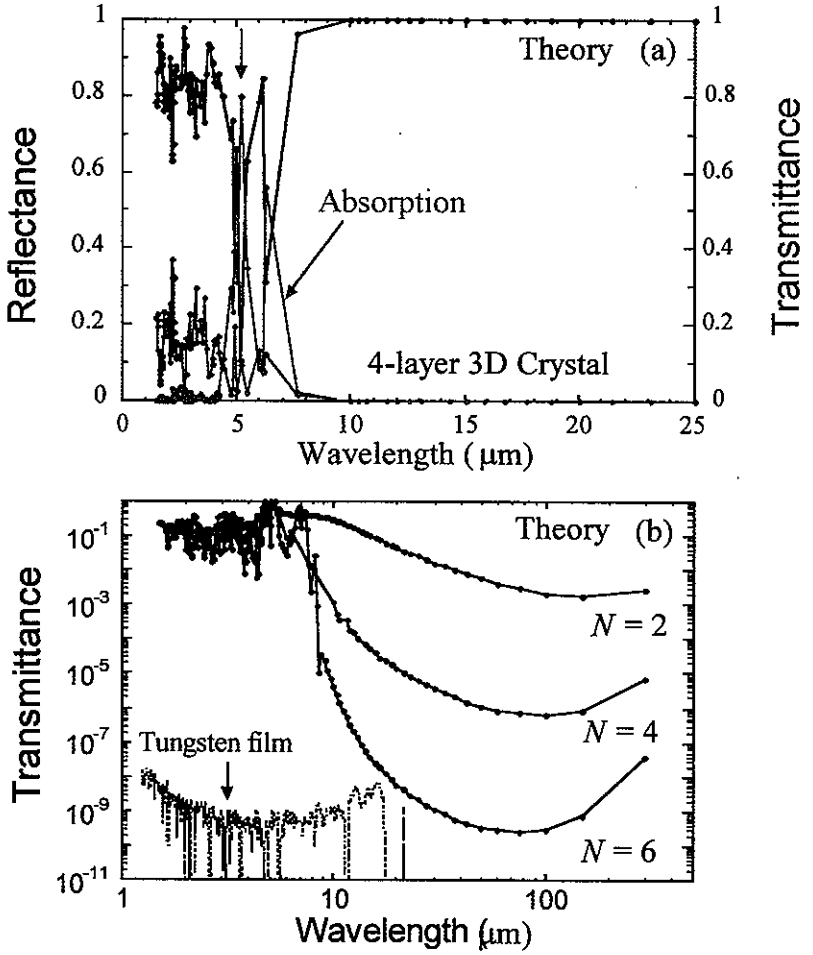

Figure 8.3 (a) A theoretically computed reflectance (black dots), transmittance (blue dots) and absorptance (red dots) spectra for the 4-layer 3D Tungsten photonic crystal. (b) Computed transmission spectra for 3D Tungsten photonic crystal samples of different number-of-layer, N=2, 4 and 6. The plot is in a log-to-log scale. The dashed line is a reference measured for a uniform 6000Å Tungsten-film.

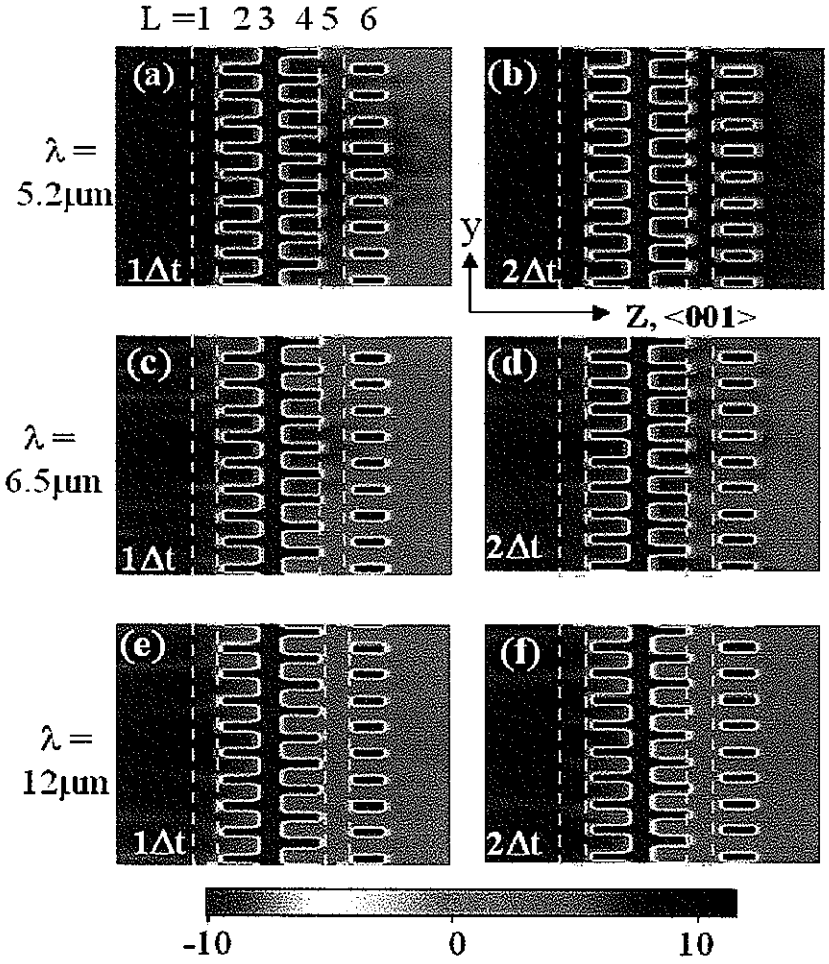

Figure 8.4 Results of a finite-difference-time-domain (FDTD) calculation for a six-layer Tungsten 3D photonic crystal. Calculations are done for three different λs ($\lambda = 5.2$, 6.5 and $12\mu m$) and at two separate time steps ($T = 1\Delta t$ and $2\Delta t$). The simulation light source is a point source, indicated by arrows, and intensity profile plotted across the y-z plane in a logarithmic scale. The purple and red colors represent the strongest and weakest intensity, respectively. The y-z plane intersects with even-layer metallic rods (L=2, 4 and 6) and the L=3 odd-layer rod. The two yellow dashed lines indicate locations of the other two odd-layer rods, L=1 and 5. Light wave transports strongly through the 3D crystal at $\lambda = 5.2\mu m$, less intensively and more slowly at $\lambda = 6.5\mu m$ and is totally reflected at $\lambda = 12\mu m$, consistent with the behavior of light propagation in the photonic allowed-band, band-edge and forbidden band-gap.

9 Summary and Conclusions

Throughout this work, we have undertaken a theoretical approach to the complex problem of modeling the flow of electromagnetic waves in photonic crystals. The methods discussed are by no means limited to handling such structures, but can be directly generalized to address any type of transport phenomena. Our focus extended beyond a pure theoretical approach to the problem to actually addressing the feasibility and use of the exciting phenomena of photonic gaps in actual applications.

To achieve our goals, we started in chapter 1 by providing a solid basis on which the current work was built. An exhaustive review of the relevant developments in the filed were summarized, both from a practical and an academic point of view. Next, we shifted our attention to providing the detailed physics underlying our theoretical approaches. Full analytical derivations of the computational electromagnetic methods used in our work were addressed in detail in chapters 2 through 5. We then shifted our attention to actual applications of the previous theoretical techniques.

We began with a discussion of 2D photonic crystal wave guides in chapter 6. The structure addressed consisted of a 2D hexagonal structure of air cylinders in a layered dielectric background. Comparison with the performance of a conventional guide was made, as well as discussions related to means and suggestions for enhancing its performance. Our studies also provided an upper theoretical limit on the performance of such guides, as we assumed no crystal imperfections and non-absorbing media. In the first part of our studies, the three-layer structure was studied in vacuum. In the second part, the three-layer structure was mounted on a high- dielectric-constant substrate to investigate the effects of substrate loss in the system.

Upon comparing our current guide feature with those of a conventional dielectric guide of

the same size, it is inevitable to conclude that the latter is in much better standing. However, one possible suggested modification expected to enhance the performance of the guide is to replace each of the upper and lower dielectric slabs by a *1D* photonic crystal. Tuned so that it has an overlapping gap with our current *2D* crystal, it is expected to completely suppress the z losses. Unlike our current situation where the z scattering-off the *2D* lattice of the air cylinders seems unavoidable because of the large value of the *refractive index,* n, of the central dielectric slab, and no matter how large the dielectric contrast is, it cannot completely eliminate the z losses. However, the only drawback that faces such a design is that the cost relative to the gain is not expected to be very high, especially since a conventional dielectric guide is seen to function very well. Nevertheless, one should make use of the ability of the *PBG* structures to reflect waves very efficiently and limit their function in a guide to bends. A feasible proposal is to use conventional dielectric guides to guide waves in the straight line segments of the required path and then to implement a *2D PBG* structure at any required bend along the path.

Having pointed out the severe limitations of 2D photonic crystals, we shift our attention to 3D photonic crystals. However, to avoid the experimental difficulties of manufacturing several unit cells primarily arising for the small index contrast of semiconducting materials, we focus our attention on the use of metals as our building blocks. This eliminates the need for multiple unit cells to realize the PBG effect. We begin in chapter 7 by theoretically studying three dimensional metallic photonic band gap (PBG) materials at near infrared and optical wavelengths. Our main objective is to find the importance of absorption in the metal and the suitability of observing photonic band gaps in this structure. For this reason, we study simple cubic structures where the metallic scatterers are either cubes or interconnected metallic rods. Several different metals are studied (aluminum, gold, copper, and silver). The effect of topology is also addressed and isolated metallic cubes are found to be less lossy than the connected rod structures. Our results reveal that the best performance is obtained by choosing metals with a large negative real part of the dielectric function, together with a relatively small imaginary part. To achieve this, simply note that by examining the Drude formula for the real and imaginary parts of the dielectric constant, Equations (7.1) and (7.2), the ratios of

the imaginary-to-real parts of the dielectric function in the high frequency limit (IR-optical) approaches the dimensionless ratio of the damping frequency to the incident electromagnetic wave frequency. The key to significantly reducing the absorption of metal in a PBG design is thus to choose metals that possess relatively small values of the damping frequency (e.g., Ag, Au, Cu, W, ..., etc.).

Our studies in chapter 7 focused on the effect of absorption. For this reason, we only studied simple cubic structures. This structure does not give the widest possible gaps but it is the simplest possible structure. We expect that our conclusions regarding the absorption will hold to any other metallic structures. By comparing the results for different metals, we found that copper gives the least possible absorption in all the cases. Gold gives slightly higher absorption. Aluminum is very lossy and is not recommended for optical photonic crystals. Isolated metallic scatterers have lower losses than the interconnected metallic networks. The most promising configuration for an optical photonic crystal is the isolated metallic scatterers composed of copper. Both silver and gold are acceptable, although slightly lower in performance. Defects in this structure introduce a narrow defect band that acts as a frequency selective filter.

The next step is to use our findings so far and utilize them in fabricating an actual metallic photonic crystal. In chapter 8, we point out a new direction in photonic crystal research that involves the interplay of photonic band gap (PBG) rejection and photonic band edge absorption. It is proposed that an absolute PBG may be used to frustrate the infrared part of the blackbody emission and, at the same time, its energy is preferentially emitted through a sharp absorption band. Potential application of this new PBG mechanism includes highly efficient incandescent lamps and enhanced thermophotovoltaic energy conversion. Here, a new method is proposed and implemented to create an all-metallic 3D crystal at infrared wavelengths, λ, for this purpose. Superior optical properties are demonstrated. The use of metal leads to the opening of a large and absolute photonic band gap (from $\lambda \sim 8\mu m$ to $> 208\mu m$). The measured attenuation strength of ~ 30 dB/ per unit cell at $\lambda = 12\mu m$ is the strongest ever reported for any 3D crystals at infrared λ. At the photonic band edge, the speed of light is shown to slow down considerably and an order of magnitude absorption enhancement

observed. In the photonic allowed band, $\lambda \sim 5\mu m$, the periodic metallic-air boundaries mold the flow of light, leading to an extraordinarily large transmission enhancement. The realization of 3D absolute band-gap metallic photonic crystal will pave the way for highly efficient energy applications and for combining and integrating different photonic transport phenomena in photonic crystals. One such potential application is the use of such a crystal to manufacture a new type of incandescent lamp. The suggested lamp would be able to recycle the energy that would otherwise go into the unwanted heat associated with usual lamps, into light emitted in the visible spectrum. It is estimated this would increase the efficiency over the conventional lamps by about 40%.

Finally, we address feasibility and challenges for realizing practical incandescent lamps. The first challenge involves the creation of metallic photonic crystals in the visible wavelengths. The minimum feature size needs to be made 10 times smaller, i.e., $100 - 200nm$. Current commercially available optical lithographic steppers can produce a feature size of $150 - 180nm$ over a 12-inch silicon wafer and down to $120nm$ by year 2004. These steppers are designed for large-scale production with high yields, which should help drive the production costs down. Another alternative is to use the direct electron-beam write lithographic technique, although it is more costly. It is also noted that a photonic band gap is effective only when infrared light is emitted within the 3D photonic crystal. Emission from the sample surfaces would experience less photonic band gap effect. One solution is to passivate the surface layers. By applying a thin insulating surface coating, electrical current can only pass through bulk portion of the 3D crystal and high emission efficiency is again achievable.

As far as future work, there are many possibilities that can extend and build upon the ideas put forward here. Specifically there are several key directions we would like to followup on:

- First there is the issue of enhancing the real space discretization process for better representation of the dielectric function. A possible improvement is to use a 9-point space stencil rather than the usual 4-point stencil. Not only would this lead to a fourth accurate representation of the discretized Maxwell's equations, but would provide a finer

mesh for the real space mesh. Such efforts are well on their way at our end. However, the process has thus far proven quite challenging, both analytically and numerically.

- Another improvement is to implement a triangular 3-point spatial mesh, rather than the usual rectangular one, or even an adaptive mesh. This approach has already been undertaken by electrical engineers for quite sometime, and is yet to be adapted by physicists in the field.

- A further improvement is to allow for the temporal as well as spatial modeling of electromagnetic waves in the presence of absorptive and gain media using the FDTD method. This would open the door to the possibility of theoretically studying photonic crystal lasers and LEDs, and would pave the way for better understanding of the physics of gain media. As we have mentioned before, current efforts in that direction have been undertaken at our end, but several tests are in order before any credit can be claimed.

- An additional improvement on the speed of convergence of the MEM method is in order. This method provides an unprecedented rich domain of information about the photonic crystals and how they mold the propagation of electromagnetic waves in them. However, it is severely limited by the memory requirements demanded by a k-space method. Two possibilities of improvements are at hand. First, there is the possibility of implementing the same technique in real space, this would reduce the computational demands. Once again, we have already started progressing towards this direction. The other is to increase further the implementation of symmetry group considerations, and make more use of the in-layer symmetry of the structure.

- Finally, an interesting direction is to study further the problem of 3D PBG waveguides. The problem can be viewed as being two-fold. First, there is the coupling problem, and this entails the design of the ultimate source for effectively coupling into such guides. Second, there is the issue of efficiency and guide performance. This is largely hindered by the fact that it is extremely hard in any temporal simulation to distinguish between forward and backward propagating waves. An ingenious idea suggested by my research

advisor, Dr. K.M. Ho, is to solve for the actual eigenmode of the guide and then actually launch this mode as our source. By taking the dot product of the subsequent wavelets with this mode, one would then be able to identify the direction of energy flow along the guide and judge its efficiency. Furthermore, by studying the behavior of this eigenmode at the termination of the guide, one may be able to identify the coupling efficiency, the related problems, as well as ways of improvements.

We hope these and similar ideas of improvements will be attempted in the near future.